Université de Liège
Faculté des Sciences Appliquées
Département Aérospatiale & Mécanique/LTAS-MN2L
Université de Liège

Faculté des Sciences Appliquées
Année Académique 2010-2011

ON THE INFLUENCE OF INDENTER TIP GEOMETRY ON THE IDENTIFICATION OF MATERIAL PARAMETERS IN INDENTATION TESTING

Pour l'obtention du grade de
Docteur en Sciences de l'Ingénieur

PhD Thesis presented by: Weichao Guo
Supervisor: Prof. Jean-Philippe Ponthot
Cosupervisor: Dr. Gast Rauchs

aides à la formation recherche
Fonds National de la Recherche Luxembourg
CENTRE DE RECHERCHE PUBLIC HENRI TUDOR www.tudor.lu

JURY MEMBERS

Prof. Pierre Duysinx, Université de Liège, Belgium. President of the jury

Prof. Jean-Philippe Ponthot, Université de Liège, Belgium. Supervisor of the thesis

Dr. Gast Rauchs, Centre de Recherche Public Henri Tudor, Luxembourg. Cosupervisor of the thesis

Dr. Anne-Marie Habraken, Université de Liège, Belgium

Prof. Ludovic Noels, Université de Liège, Belgium

Prof. Eric Béchet, Université de Liège, Belgium

Prof. Pierre Beckers, Université de Liège, Belgium

Prof. Weihong Zhang, Northwestern Polytechnical University, China

ACKNOWLEDGEMENTS

First and foremost, I wish to express my deep and sincere gratitude to Prof. Jean-Philippe Ponthot and Dr. Gast Rauchs for acting as my advisors during the work of my PhD degree, as well as for their invaluable guidance of this research. Prof. Jean-Philippe Ponthot is a generous and kind professor and has a rigorous scholarship. Although he is very busy in daily work, he regularly spared some time to discuss the problem in my work with me. I also especially thank Dr. Gast Rauchs for his continuous guidance, patience and enthusiasm about my work and for his pertinent advices in technical questions throughout my work. Without his help, I suppose that I had not achieved this research work.

Secondly, I would like to specially thank Prof. Weihong Zhang who is my advisor in China. He is one of the top experts in the field of structural optimization. Although the current work is a little far from his research field, he often gave me a lot of encouragements and practical suggestions on seeking a deeper understanding of knowledge, let me go forward continuously with great passion.

The present research work has been carried out under the financial support funded by the FNR (Fonds National de la Recherche) of the Grand Duchy of Luxembourg, under the grant number TR-PHD BFR 06/027. Without the financial support, I would not have had the chance of doing the thesis.

I would also like to express my appreciation to Prof. François Gitzhofer and Dr. Lu Jia in Plasma Technology Research Centre (CRTP) in the University of Sherbrooke, Canada, for providing some experimental data on thin film coating.

I am grateful to all the members in Prof. Jean-Philippe Ponthot's research group for their technical supports on my work.

Many thanks are reserved for a number of colleagues and friends for their critical and constructive remarks throughout this research work. Although the list of these people is too long to be given in totality, I would especially like to thank these Chinese friends. Some interesting activities were held regularly and I always felt the familial atmosphere nearby. Special thanks are devoted to Dr. Aimin Yan and Dr. Lihong Zhang.

I have become the person I am today thanks to the continuous care and love of my family. No matter when and where, my parents and my elder brother always provide their unconditional support, care and love to me. Finally, this dissertation with love and gratitude is dedicated to my

wife, Qi Wang, for her kind encouragements and for accompanying along with me in Belgium during the work of PhD degree.

Finally, I would like to thank the members of the jury who have read and commented the present thesis. I also thank them for their presence at my public defence.

TABLE OF CONTENTS

ABSTRACT

The rapid development of structural materials and their successful applications in various sectors of industry have led to increasing demands for assessing their mechanical properties in small volumes. If the size dimensions are below micron, it is difficult to perform traditional tensile and compression tests at such small scales. Indentation testing as one of the advanced technologies to characterize the mechanical properties of material has already been widely employed since indentation technology has emerged as a cost-effective, convenient and non-destructive method to solve this problem at micro- and nanoscales.

In spite of the advances in indentation testing, the theory and development on indentation testing are still not completely mature. Many factors affect the accuracy and reliability of identified material parameters. For instance, when the material properties are determined utilizing the inverse analysis relying on numerical modelling, the procedures often suffer from a strong material parameter correlation, which leads to a non-uniqueness of the solution or high errors in parameter identification. In order to overcome that problem, an approach is proposed to reduce the material parameter correlation by designing appropriate indenter tip shapes able to sense indentation piling-up or sinking-in occurring in non-linear materials.

In the present thesis, the effect of indenter tip geometry on parameter correlation in material parameter identification is investigated. It may be helpful to design indenter tip shapes producing a minimal material parameter correlation, which may help to improve the reliability of material parameter identification procedures based on indentation testing combined with inverse methods.

First, a method to assess the effect of indenter tip geometry on the identification of material parameters is proposed, which contains a gradient-based numerical optimization method with sensitivity analysis. The sensitivities of objective function computed by finite difference method and by direct differentiation method are compared. Subsequently, the direct differentiation method is selected to use because it is more reliable, accurate and versatile for computing the sensitivities of the objective function.

Second, the residual imprint mappings produced by different indenters are investigated. In common indentation experiments, the imprint data are not available because the indenter tip itself shields that region from access by measurement devices during loading and unloading. However, they include information about sinking-in and piling-up, which may be valuable to reduce the correlation of material parameter. Therefore, the effect of the imprint data on identification of material parameters is investigated.

Finally, some strategies for improvement of the identifiability of material parameter are proposed. Indenters with special tip shapes and different loading histories are investigated. The sensitivities of material parameters toward indenter tip geometries are evaluated on the materials with elasto-plastic and elasto-visoplastic constitutive laws.

The results of this thesis have shown that first, the correlations of material parameters are related to the geometries of indenter tip shapes. The abilities of different indenters for determining material parameters are significantly different. Second, residual imprint mapping data are proved to be important for identification of material parameters, because they contain the additional information about plastic material behaviour. Third, different loading histories are helpful to evaluate the material parameters of time-dependent materials. Particularly, a holding cycle is necessary to determine the material properties of time-dependent materials. These results may be useful to enable a more reliable material parameter identification.

PUBLISHED PAPERS

Guo, W.C., Rauchs, G., Zhang, W.H. and Ponthot, J.P., (2010). Influence of friction in material characterization in microindentation measurement. Journal of Computational and Applied Mathematics, Vol. 234, pp. 2183-2192.

Ponthot, J.P., Guo, W.C., Rauchs, G. and Zhang, W.H., (2009). Influence of friction on imperfect conical indentation for elastoplastic material. Tribology - Materials, Surfaces & Interfaces, Vol. 3, pp. 151-157.

ATTENDED CONFERENCES

Guo, W.C., Rauchs, G., Ponthot, J.P. and Zhang, W.H., (2009). Study the influence of friction in imperfect conical indentation for elasto-plastic material. The 3rd Vienna International Conference on Nano-Technology, Vienna, Austria.

Guo, W.C., Ponthot, J.P., Zhang, W.H. and Rauchs, G., (2008). The influence of friction on elasto-plastic materials in nanoindentation. The 4th International Conference on Advanced Computational Methods in Engineering, Li ège, Belgium.

NOTATIONS

Greek characters

α	Back stress
α_m	Parameter for evaluating piling-up or sinking-in
α_{mc}	Material constant in calculating creep parameter
β	Parameter for magnifying the difference between indentation depth and contact depth
β_c	Correction factor for calculating reduced elastic modulus
δ	Kronecker delta
$\dot{\varepsilon}$	Strain rate
ε_e	Elastic strain
ε_g	Geometric parameter for calculating contact depth
ε_R	Representative strain
ε_p	Plastic strain
$\bar{\varepsilon}_p$	Effective plastic strain
ε_y^0	Initial yield strain
η	Coefficient of viscosity
θ	Half apex angle
$\boldsymbol{\lambda}$	Lagrange multipliers
λ_{jk}	Cosine matrix of Hessian matrix
μ	Friction coefficient
ξ	Material parameter in Voce-type hardening law
ρ	Radius of imperfect indenter tip
σ	1D stress
$\boldsymbol{\sigma}$	Cauchy stress tensor
$\overset{\nabla}{\boldsymbol{\sigma}}$	Objective rate of the Cauchy stress tensor
$\bar{\sigma}$	Effective stress
σ_R	Representative stress

σ_v	Current yield stress
σ_{visco}	Stress due to viscous effect
$\dot{\varepsilon}_{vp}$	Rate of effective viscoplastic strain
σ_y^o	Initial yield stress
$\tau_{\max}$	Maximum shear stress
υ	Poisson's ratio of indented material
υ_i	Poisson's ratio of indenter
ω	Excitation frequency

Latin Characters

a	Contact area radius
a_c	Contact area radius in cone
a_{ec}	Constant in calculating fracture toughness
A_{proj}	Projected contact area
B	Constant in calculating initial unloading stiffness
C	Loading curvature
C_F	Length of radial fracture
C_i	Constant in calibrating projected contact area with contact depth
D	Constant in Cowper-Symonds law
$\mathbf{D}$	Rate of deformation tensor
$\mathbf{D}^e$	Elastic part in rate of deformation
$\mathbf{D}^p$	Inelastic part in rate of deformation
D_s	Damping coefficient
E	Young's modulus of indented material
E_i	Young's modulus of indenter
E_r	Reduced modulus
E'	Storage modulus
E''	Loss modulus
f	Yield function
$\mathbf{F}$	Deformation gradient
F	Objective function
f_g	Geometrical factor

Notations

G	Shear modulus
h	Indentation depth
$\dot{h}$	Indentation depth rate
h_c	Contacted depth
h_d	Deviation of penetration depth for the imperfect indenter
h_f	Residual depth
$h_{\max}$	Maximum indentation depth
H	Indentation hardness
$\mathbf{H}$	Hooke stress-strain tensor
H_{ij}	Hessian matrix
$\widetilde{H}_{ij}$	Approximated Hessian matrix
H_{kh} , H_{kin}	A kinematic hardening parameter in Armstrong-Frederick law
H_{kb} , H_{nl}	A dimensionless parameter in Armstrong-Frederick law
H_P	Work-of-indentation hardness
$\mathbf{I}$	Identity tensor
k_c	Correction factor in calculating work-of-indentation hardness
$\mathbf{K}(\mathbf{x})$	A linear differential operator in space with design vector $\mathbf{x}$
K	Bulk modulus
K_c	Fracture toughness
L	Length
$\mathbf{L}$	Spatial gradient of velocity
Lx	Length
Ly	Length
m	Viscosity exponent
m_s	Constant in calculating initial unloading stiffness
M	A set of reference points on contact surface
n	Work-hardening exponent
N	Number of load steps or design variables
n_c	Creep stress index
nx	Number of elements in horizontal direction
ny	Number of elements in vertical direction
P	Indentation load

$P_{\max}$	Maximum indentation load
$\mathbf{P}(\mathbf{x})$	Load data $\mathbf{P}(\mathbf{x})$ with design vector $\mathbf{x}$
Q	Material parameter in Voce-type hardening law
Q_c	Activation energy
$\mathbf{r}^0$	Position located at imprint centre
$\mathbf{r}^l$	Radial location
R	Radius of spherical indenter
$\mathbf{R}$	Rotation tensor
R_c	Universal gas constant
s	Plastic arc length
$\mathbf{s}$	Deviator of the stress tensor
S	Initial unloading stiffness
t	time
T	Temperature
$\mathbf{U}$	Stretch tensor
$\mathbf{v}$	Velocity
V_P	Volume of plastic deformation
W_E	Elastic work
W_P	Plastic work
W_T	Total work
$\mathbf{x}$	Vector of design parameters
x_i	Design variable
$\mathbf{Y}$	Position vector

CHAPTER 1

INTRODUCTION

Overview

This chapter deals with the effect of the indenter tip geometry in indentation testing. First, the purpose of such an investigation is stated. Second, the main contents of the thesis are introduced.

Contents

1.1. Motivation of the study

As an advanced measuring technology, indentation testing has been widely used in various industrial fields to determine material properties. Such a technology can provide a unique mechanical response in small volumes, especially for the measurement of material properties at microscopic and smaller scale or when such properties are affected by material structures which cannot be removed (e.g. the hardness of bone is affected by its internal trabeculae and the hardness of weld joint is affected by workpieces). For instance, the Fig. 1. 1 shows a group of gears and a MEMS device which are designed at microscopic scale (Kim et al., 2003). Tensile and compression tests cannot be applied to these small structures. Moreover, for some kinds of materials like bone – see Fig. 1. 2 (Zysset et al., 1999) – the mechanical properties, namely, elasticity and hardness, are related to the structures of the bone. Accordingly, micro-indentation and especially nano-indentation are valuable technologies for the local investigation of the properties of such materials.

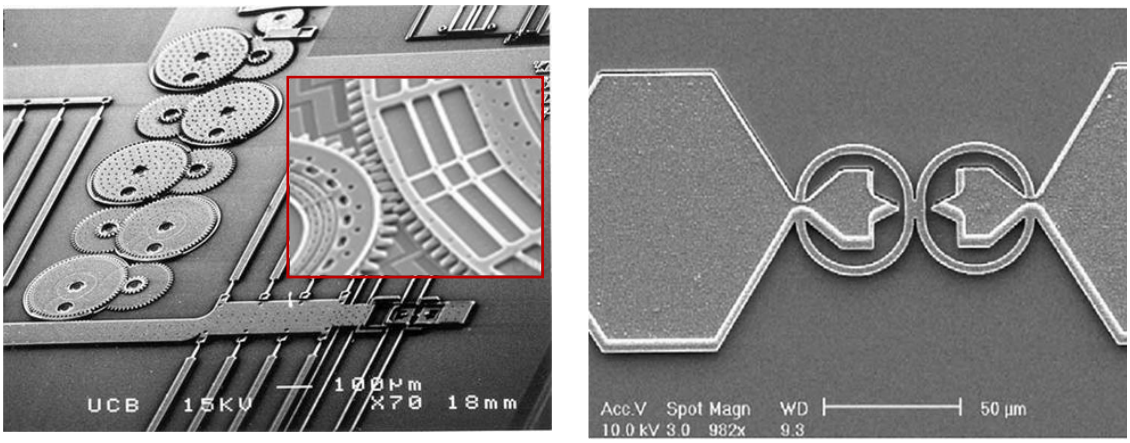

(a) (b)

Fig. 1. 1. (a) A group of gears (www.web.mit.edu/3.052/www/Lectures2003/Lecture2.ppt) and (b) a MEMS device (Kim et al., 2003) designed at microscales.

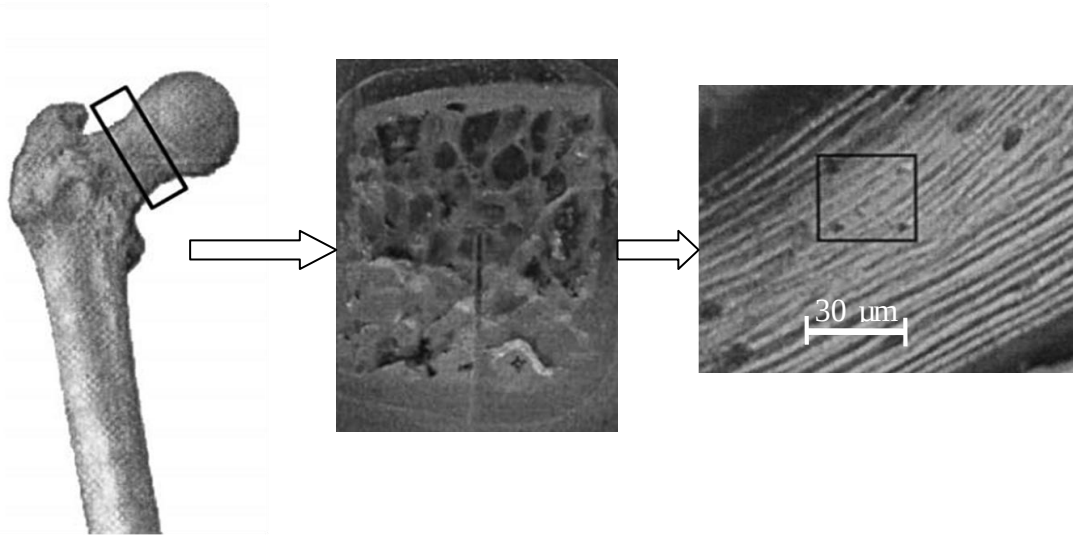

Fig. 1. 2. Determination of the material property of human femur (Zysset et al., 1999).

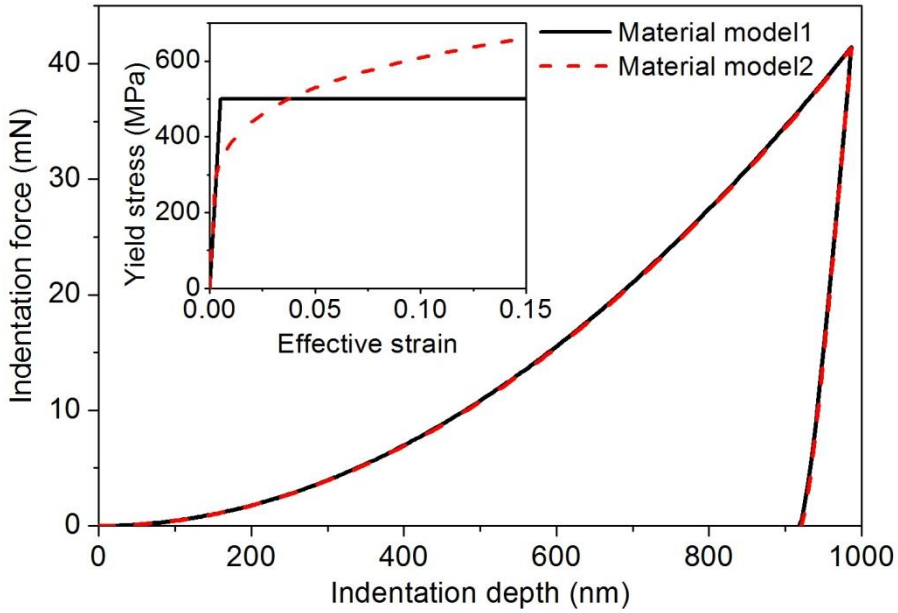

Fig. 1. 3. A pair of different materials with indistinguishable loading and unloading curves, which are produced by indentation testing with a conical indenter with the half apex angle of 70.3° (Chen et al., 2007).

In order to have a unique solution in the identification of any material parameter, the indentation response must ideally be unique for a given material. This means that a one-to-one correspondence between the measured indentation load-displacement curves and the elasto-plastic properties of the material is needed. However, in spite of the advances of indentation technology, the properties of some materials are still difficult to identify in a unique way. Indeed, as shown in Fig. 1. 3, two material models have obviously different elasto-plastic properties, yet

they yield almost identical indentation behaviours which are measured by indentation testing using the same conical indenter with a half apex angle of 70.3°. Other more "mystical materials[1]" can be seen in the investigation carried out by (Chen et al., 2007). The materials lead to indistinguishable indentation behaviours although they have different elasto-plastic properties and they are identified by several types of indenters.

Furthermore, some material parameters are not directly obtained via experimental procedures, but they are rather determined through inverse methods that rely on numerical modelling. These procedures are usually designed to determine material parameters using numerical optimisation techniques to minimise the difference between experimental and modelled load-displacement curves. Nevertheless, it is well known that these procedures are often characterised by a strong material parameter correlation (Mahnken and Stein, 1996b; Forestier et al., 2003). Consequently, it is difficult to obtain unique and accurate material parameters.

In indentation measurement, the determined results, namely, hardness and Young's modulus, are heavily dependent on the load-displacement curve. However, the load-displacement curve is a non-local quantity because it results from an integral over the whole contact surface, which leads to the loss of crucial information. For these reasons, it is necessary to find ways to reduce this correlation in order to obtain stable and unique material parameter results. Some improvements have been achieved by including additional experimental data in objective function, like residual imprint mappings of the residual imprint that remains after load removal in the indentation test (Bolzon et al., 2004; Bocciarelli et al., 2005; Bocciarelli and Bolzon, 2007). These residual imprint mappings contain information about the deformation of the specimen surface under and around the indenter – e.g. indentation sinking-in or piling-up – which is of the outmost importance for the quantification of the plastic material behaviour. However, this information is not available during indentation experiments because the indenter tip itself shields the contact region from access by measurement devices. This information can only be determined after the removal of the indenter.

Therefore, the main aim of this thesis is to sense the relationship between the indentation piling-up or sinking-in and the geometrical shape of the indenter tip. According to recent investigations (Cheng et al., 2006; Kozhevnikov et al., 2010), some indenters which have arbitrary geometrical tip shapes are used to investigate the loading-unloading curve and the distribution of contact pressure for viscoelastic material. Thus, the main idea is to design some indenters with a special geometrical tip shape because the geometry of the residual imprint mapping and the mechanical response are directly related to the tip shape of the indenter. It is desired that the imprint data produced by the designed arbitrary shape indenters may include additional information. Given that the indenter has a more complex geometrical shape the material flow and the stress

[1] Mystical materials: Chen et al., (2007) presume some materials which have distinct elasto-plastic properties, yet they always yield the identical load-displacement curves when they are measured using indentation testing.

distribution under this indenter should be more complex. The indentation imprint data and the load-displacement curve may be sensitive to this indenter shape. This may be valuable in reducing the parameter correlation and improving the identifiability of material parameters.

Consequently, it is necessary to investigate the effect of the indenter tip geometry on the parameter correlation in the identification of material parameters. It may help to design indenter tip shapes by producing a minimal material parameter correlation. This may contribute to the improvement of the reliability of material parameter identification procedures which are based on indentation testing combined with inverse methods.

The current research work presented in this thesis was supported by the "Centre de Recherche Public Henri Tudor", under the research project "FNR-Project FNR/05/02/01 VEIANEN" funded by FNR (Fonds National de la Recherche) of the Grand Duchy of Luxembourg. The grant number is TR-PHD BFR06-027. The work is a collaboration between Prof. Jean-Philippe Ponthot from the Aerospace and Mechanical Engineering Department of the University of Liège, and Dr. Gast Rauchs from the Department of Advanced Materials and Structures of the "Centre de Recherche Public Henri Tudor".

1.2. Outline of the thesis

Two main parts are dealt with in this thesis: Firstly, the effect of the indenter tip geometry on the identification of material parameters is assessed. Secondly, strategies for a more reliable identification of material parameters and for the improvement of the identifiability of material parameter are proposed.

After a presentation of the state of the art in indentation testing, chapter 2 reviews the basic theory and the related studies on the subject. Then, it presents the applications of indentation and the methods used for the identification of material properties. Subsequently, the method for assessing the correlation of material parameters is introduced. Finally, the similarities and differences between the geometrical shapes of classical indenters are analysed through illustrations.

Chapter 3 is dedicated to the discussion of some main factors which may affect the indentation results. The results obtained in numerical simulations and experiments are compared. The dispersions of the indentation results produced by the contact friction and the indenter tip rounding are specially demonstrated. At the same time, an illustration of the contribution of numerical models to the understanding and the interpretation of indentation results is highlighted. At last, an example for determining the mechanical properties of a thin film coating is performed.

In chapter 4, an illustration for assessing the importance of the residual imprint mapping data and the indenter tips on material parameters identification is performed. Then, two strategies for the improvement of the identification of material parameters are introduced. One relies on changing the tip shape of the indenter while the other relies on altering the loading history.

In chapter 5, the efficiency of several kinds of indenter tip shapes are assessed on the basis of various material constitutive laws, i.e. elasto-plastic and elasto-viscoplastic.

Finally, the overall conclusions of the research work discussed in this thesis are given in chapter 6, together with the outlook and the further developments it implies.

1.3. Main contributions of the thesis

Some main original contributions of this thesis are worth noting. First, the work has investigated the influence of the rounded indenter tip on indentation hardness. Then it has proposed an improved method to calculate the hardness of material for the indenter with a rounded tip. The results show this method can significantly improve the accuracy of the calculated hardness. Second, the work has assessed the effects of imprint data and indenter tip geometry on the parameter correlation in the identification of material parameters. Third, the work has proposed two strategies for improving the identifiability of material parameters.

The geometrical shapes of classical indenters which include spherical, conical, Vickers and Berkovich indenters are compared in chapter 2 and their effects on the correlation of material parameters are assessed in chapter 4. On the basis of the forgoing investigations, strategies for the improvement of the identifiability of material parameters are proposed, namely, the use of arbitrary indenter tip shapes and a different form of loading history to reduce the correlation of material parameters. The efficiencies of different indenters for decreasing the parameter correlation are compared according to several material constitutive laws. At the same time, and the effect of imprint data on the parameter correlation is assessed too.

Moreover, the indentation results and the sources of their dispersion have been analyzed. The influences of the contact friction and the influences of indenter tip rounding on indentation testing results are particularly investigated. The results show that neither the contact friction nor the rounded tip radius of the imperfect indenter should be neglected. Besides, residual imprint mapping data are introduced into the objective function to reduce the correlation of material parameters. The results show that for the elasto-plastic materials with small ratio of E/σ_y^0 and elasto-viscoplastic materials, the imprint data are helpful to decrease the correlation of material parameters.

CHAPTER 2

MATERIAL PROPERTY IDENTIFIED BY INDENTATION TESTING

Overview

This chapter starts with a review of the state of the art in indentation testing and the related studies on the subject. Secondly, it introduces the applications of indentation testing in practice and the frequently used methods for the identification of material parameters. Then, the frequently used methods for the identification of material parameters and the method for assessing the correlation of the material parameters are presented. Finally, the similarities and differences between the geometrical shapes of classical indenters are analysed.

Contents

2.1. State of the art review in indentation testing

An indentation measurement is conducted by pushing vertically a hard indenter, the mechanical properties of which are known, into the plane of a specimen characterised by unknown mechanical properties, while recording the load and the displacement of the indenter into the surface – see Fig. 2. 1. The two mechanical properties which are most frequently extracted from this load-displacement curve are Young's modulus, E (unit is MPa) and hardness, H (unit is GPa).

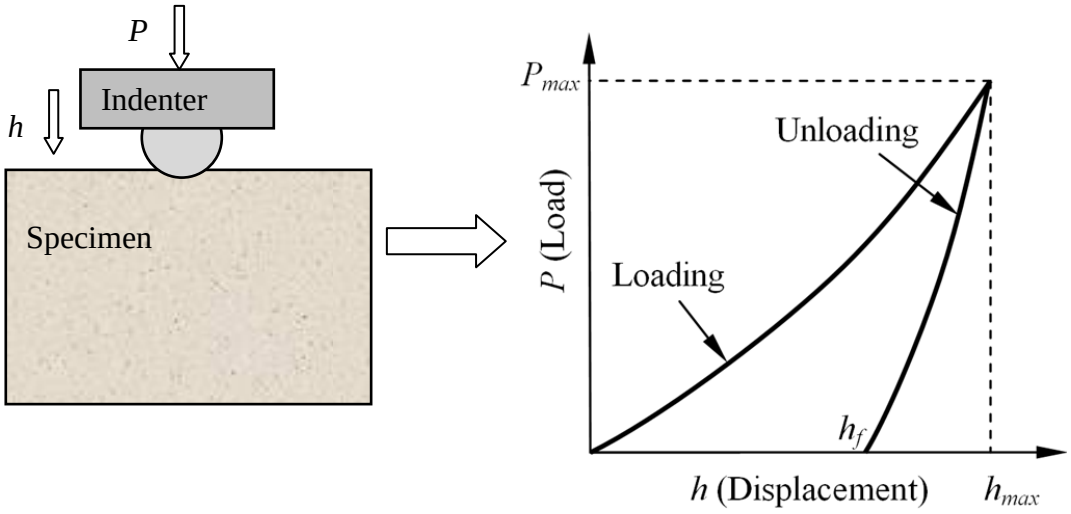

Fig. 2. 1. A schematic illustration of the identification of a bulk material.

Indentation testing has its origins in Moh's hardness test of 1822 (Fischer-Cripps, 2002) and the analytical approach to the contact problem in indentation testing traces back to Hertz contact theory of 1881. Since that time, many methods were developed for hardness measurements and various definitions for hardness were proposed. For instance, the Brinell hardness test method was proposed in 1900 (Borodich and Keer, 2004; Hutchings, 2009). It was the first widely used and standardised hardness test method for a wide variety of materials. This test consists of applying a 5 or 10 mm diameter steel ball with a load of 30000 N on a metal sample with a flat surface. For softer materials the load is reduced to 15000 N or 5000 N to avoid excessive indentation. The Brinell hardness is calculated by dividing the maximum applied load by the imprint area after unloading. The Vickers hardness test was developed in 1922 (Hutchings, 2009). It is similar to the Brinell test, but it employs only one pyramidal diamond indenter with a square base. The two diagonals of the imprint after unloading are measured using a microscope. Then the average length is calculated for evaluating the square area of the imprint.

The Vickers hardness equals the ratio of the maximum applied load to the imprint area. Moreover, Rockwell hardness test method was also developed in the early twentieth century (Hutchings, 2009). In the Rockwell hardness test, the used indenter is either a diamond cone or a hardened steel ball. To start this test, the indenter is forced into a sample at a prescribed minor load. Then, a major load is applied and held for a set time period. Subsequently, the force on the indenter is decreased back to the minor load. The Rockwell hardness is calculated from the depth of permanent deformation of the indenter into the sample, namely, the difference in indenter position before and after application of the major load.

Although hardness measurement has been well known for approximately two hundred years, the use of indentation technology to measure hardness has gained new popularity during the last decades. In the middle of the twentieth century, some major contributions to this testing method were introduced by the pioneering researchers (Lysaght, 1949; Tabor, 1951). In their work, the hardness tests – e.g. Brinell, Rockwell hardness – were reviewed. Subsequently, the same method was applied at microscale (Doerner and Nix, 1986; Tirupataiah and Sundararajan, 1987). So indentation testing has begun to represent an effective practical methodology for material characterisation. At the end of the twentieth century, (Oliver and Pharr, 1992) made another major contribution to indentation testing. In their works, an improved method has been proposed to determine hardness and Young's modulus using load-displacement curve. The hardness and the Young's modulus of the indented material computed by the improved technology were proved to have higher accuracies. This improved technology has been used widely in current indentation instruments.

Thanks to modern computers, and to advanced numerical methods, many indentation tests have been developed rapidly in recent years involving spherical indentation (Taljat and Pharr, 2004; Jeon et al., 2006; Harsono et al., 2009), conical indentation (Cheng and Cheng, 1999; Fischer-Cripps, 2003; Abu Al-Rub, 2007; Durban and Masri, 2008; Berke et al., 2009), Vickers indentation (Antunes et al., 2006; Antunes et al., 2007; Yin et al., 2007) and Berkovich indentation (Fischer-Cripps, 2001; Kese et al., 2005; Foerster et al., 2007; Sakharova et al., 2009), based on the foregoing pioneering works. Now, most of those indentation measurements are already standardised by the ISO (the International Organization for Standardization), e.g. ISO 14577, which covers the indentation testing for indentations in the macro-, micro- and nano-scale ranges (Fischer-Cripps, 2002).

At present, advanced indentation instruments can provide accurate measurements of the continuous variation of the indentation load P down to μN, as a function of the indentation depth h down to nm. When the displacement of the indenter is measured at nanometres (10^{-9} m) rather than microns or millimetres (10^{-3} m), the indentation is referenced to as nanoindentation.

Concurrently, comprehensive theoretical and computational studies have emerged to elucidate the contact mechanics and the deformation mechanisms in order to systematically extract material properties from the load-displacement curves obtained from instrumented indentation. For example, the hardness can be obtained from the maximum load and the initial unloading slope using the suggested methods (Oliver and Pharr, 1992). The elastic and plastic properties may be computed through the adequate procedures (Venkatesh et al., 2000; Swadener et al., 2002a), whereas the residual stresses may be extracted by the method presented in (Suresh and Giannakopoulos, 1998).

As the understanding of mechanics in indentation testing increases, and especially, thanks to the pioneering work of (Oliver and Pharr, 1992), not only is indentation testing used to measure hardness, but it is also used to evaluate material parameters like the Young's modulus and the yield strength. Indeed, since the end of the twentieth century, indentation has been employed to measure the mechanical behaviour of materials for various engineering applications (Gouldstone et al., 2007). The main reason for its wide use is that it can be carried out at microstructural scales, and even at micro- and nanoscales, which makes this technique one of the most powerful tools for the characterisation of bulk materials in small volumes. For instance, indentation testing can evaluate the properties of the materials used in electronic solders or engineering welds (Ma et al., 2003), while keeping the structural integrity.

The increasing advance of the theory and the methodology on indentation testing brought about the rapid development of indentation measurement instruments. Nowadays, various indentation instruments are used by many famous manufactures, namely, MTS Systems Corp. (www.mtsnano.com), Micro Materials Ltd. (www.micromaterials.co.uk), CSIRO Inc. (www.csiro.au/hannover/2000/catalog/projects/umis.html), Hysitron Inc. (www.hysitron.com) and CSM Instruments Corp. (www.csm-instruments.com). The representative products of those manufacturers are shown in Fig. 2. 2, whereas most of the indentation systems are represented in the schematic illustration in Fig. 2. 3 (Hengsberger et al., 2001). They include three main parts: indenter, load application, and capacitive sensor for measuring the displacements of the indenter. The load is applied by an electromagnetic coil which is connected to the indenter shaft by a series of leaf springs. The deflection of the springs is a measure of the load applied to the indenter. The displacement is usually measured by a capacitive sensor.

(a) Nano-Indenter XP (MTS)

(b) Ultra-Micro-Indentation System (CSIRO)

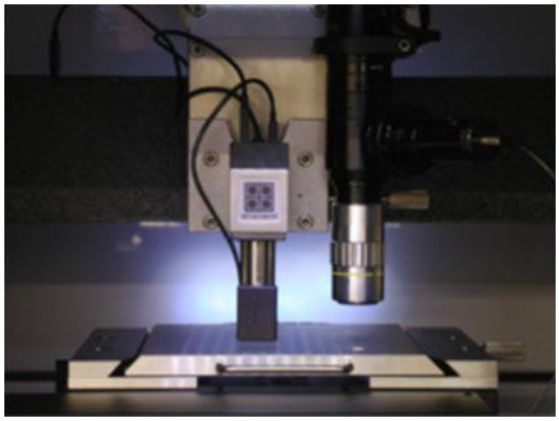

(c) Triboscope (Hysitron)

(d) Nano-Hardness Tester (CSM)

Fig. 2. 2. Representative indentation instruments.

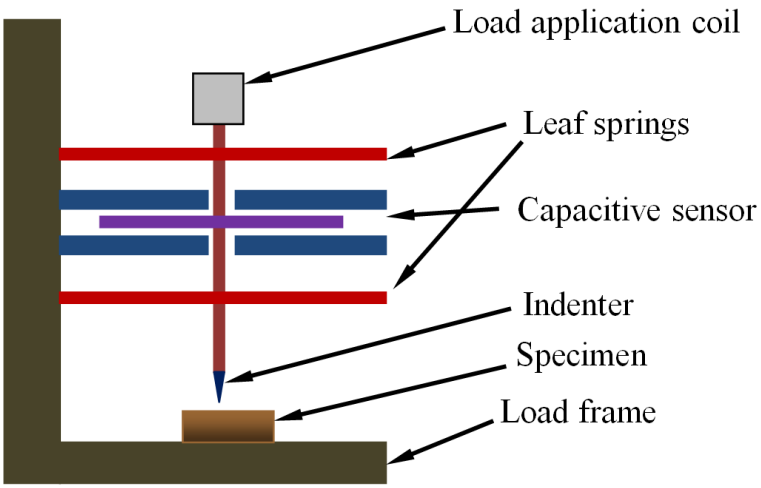

Fig. 2. 3. A schematic illustration of a typical indentation instrument structure (Hengsberger et al., 2001).

Despite the significant evolution of indentation test instruments, the tests require considerable experimental skills and resources. Such tests are extremely sensitive to thermal drifts and mechanical vibration. Therefore, in some cases, a more accurate experiment should be performed in a stable environment. For example, the specimen and the indenter are mounted in an enclosure to insulate against temperature variation, vibration and acoustic noise if the specimen is measured using the Hysitron Triboindenter instrument (Hysitron, 2005), see Fig. 2. 4.

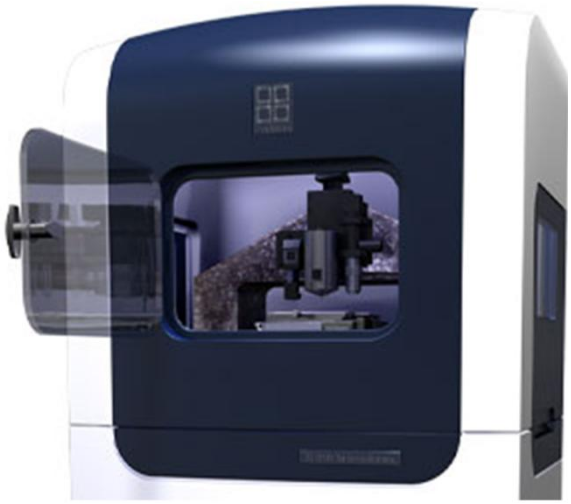

Fig. 2. 4. Indentation instrument with an enclosure (www.hysitron.com).

Experimental investigations of indentation have been conducted on many materials to extract hardness and other mechanical properties such as Young's modulus (Oliver and Pharr, 1992),

yield stress (Kucharski and Mroz, 2007), fracture toughness (Perrott, 1978; Kruzic et al., 2009) and work-hardening coefficient (Huber and Tsakmakis, 1998; Mata et al., 2002a; Durban and Masri, 2008). Besides, indentation testing is also widely performed for the evaluation of many complex material systems like thin film coatings. Coated products have found increasing applications in the industry because of their unique sets of surface characteristics, but also due to the fact that the base material/coating combination which can be tailored to provide resistance to heat, wear, erosion and/or corrosion (Fauchais, 2004).

In practical applications, the coatings need to be subjected to intense mechanical loads, and, hence, it is necessary to explore their mechanical response in order to predict their appropriate operating conditions and their life expectancy. However, the traditional methods, such as compression and tensile tests, are difficult to apply well at such small scales. Indentation testing, as a newly developed measurement method, has proved to be successful in the identification of the mechanical properties of coating (Landman and Luedtke, 1996; Balint et al., 2006; Rodriguez et al., 2007; Zhang et al., 2007a).Indeed, indentation testing has been widely used in micro- and nano-electro-mechanical systems – MEMS and NEMS (Opitz et al., 2003; Haseeb, 2006; Bocciarelli and Bolzon, 2007; Yan et al., 2007; Shi et al., 2010) and ceramic thermal barrier coating – TBC (Bouzakis et al., 2003; Lugscheider et al., 2003; Rodriguez et al., 2009). Furthermore, in the case of the relatively thin thickness coatings, e.g. the thickness < 10 μm, conventional indentation testing can provide simple, efficient and robust means for the evaluation of the coatings properties (Bouzakis et al., 2003; Mohammadi et al., 2007; Rodriguez et al., 2009). More significant still, indentation testing is also used in the medical area, namely, for the identification of the properties of bones and biomaterials (Cense et al., 2006; Kruzic et al., 2009; Sun et al., 2009).

However, such indentation testing is limited by its definition. For example, the conventional indentation methods for the calculation of the modulus of elasticity (based on the unloading curve) are built on the hypothesis of isotropic materials although this test is nearly already extended to measure almost all the anisotropic elastic materials. If a material exhibits a viscous behaviour, the initial stiffness of the unloading curve may be negative. Thus, the evaluated modulus of elasticity will be meaningless. Besides, the problem related to the "piling-up" or the "sinking-in" of the material on the edges of the specimen during the indentation process is still under investigation (Hengsberger et al., 2001).

In summary, although indentation testing is limited in some practical applications, it remains valuable because it allows the researchers to carry out local investigations of the material behaviour, which can give important insights about how materials are affected by production processes and service conditions.

2.2. Related studies

2.2.1. Constitutive formulations of materials

Numerical methods are frequently performed for depth understandings of indentation testing. In this thesis, many investigations are also carried out utilizing numerical simulations. In numerical simulation, the constitutive formulation of indented materials should be established in a mathematical expression. Here, the establishment of the formulation considers the previous work of (Ponthot, 2002), where a unified stress update algorithm for elastic–plastic constitutive equations is introduced and then extended to elasto-viscoplasticity in a finite deformation framework using a corotational formulation, within an updated Lagrangian scheme.

The position of a material particle in the reference configuration of a body, corresponding to a time t_o can be denoted by its position vector, $\mathbf{Y}$. Then, its position in the deformed configuration of the body, corresponding to a time t ($t > t_0$), is noted by $\mathbf{y} = \mathbf{y}(\mathbf{Y}, t)$. The velocity of the reference point is defined by

$$\mathbf{v} = \dot{\mathbf{y}} = \frac{\partial \mathbf{y}(\mathbf{Y}, t)}{\partial t}. \tag{2.1}$$

The deformation gradient relating the deformed configuration to the initial configuration is defined as

$$\mathbf{F} = \frac{\partial \mathbf{y}}{\partial \mathbf{Y}} \text{ with } J = \det \mathbf{F} > 0. \tag{2.2}$$

By polar decomposition, the stretch tensor $\mathbf{U}$ and the rotation tensor $\mathbf{R}$ can be uniquely defined by

$$\mathbf{F} = \mathbf{R}\mathbf{U} \text{ with } \mathbf{R}^T\mathbf{R} = \mathbf{I} \text{ and } \mathbf{U} = \mathbf{U}^T, \tag{2.3}$$

where $\mathbf{I}$ represents the identity tensor. The corresponding spatial gradient of velocity is given by

$$\mathbf{L} = \frac{\partial \mathbf{v}}{\partial \mathbf{y}} = \dot{\mathbf{F}}\mathbf{F}^{-1}. \tag{2.4}$$

It can be decomposed into a symmetric and an antisymmetric part,

$$\mathbf{L} = \mathbf{D} + \mathbf{W}, \tag{2.5}$$

with

$$\mathbf{D} = \frac{1}{2}(\mathbf{L} + \mathbf{L}^T) \text{ the rate of deformation tensor,} \tag{2.6}$$

$$\mathbf{W} = \frac{1}{2}(\mathbf{L} - \mathbf{L}^T) \text{ the spin tensor.} \tag{2.7}$$

The rate of deformation can be additively decomposed into an elastic, $\mathbf{D}^e$ (reversible) and an inelastic, $\mathbf{D}^p$ (irreversible) part, i.e.

$$\mathbf{D} = \mathbf{D}^e + \mathbf{D}^p . \tag{2.8}$$

The relationship between the rate of strain and the rate of stress is postulated as

$$\overset{\nabla}{\boldsymbol{\sigma}}_{ij} = H_{ijkl}(\mathbf{D}_{kl} - \mathbf{D}^p_{kl}) \text{ or } \overset{\nabla}{\boldsymbol{\sigma}} = \mathbf{H} : (\mathbf{D} - \mathbf{D}^p), \tag{2.9}$$

where $\overset{\nabla}{\boldsymbol{\sigma}}$ is an objective rate of the Cauchy stress tensor $\boldsymbol{\sigma}$. $\mathbf{H}$ is the Hooke stress-strain tensor (elastic stiffness tensor) which is given by

$$H_{ijkl} = K\delta_{ij}\delta_{kl} + 2G(\delta_{ik}\delta_{jl} - \frac{1}{3}\delta_{ij}\delta_{kl}), \tag{2.10}$$

where δ is the Kronecker delta symbol, K is the bulk modulus and G is the shear modulus of the material.

Plastic deformation is triggered when the stress in the material reaches a given limit. In the material model, the yield function is used to detect an increase of the plastic deformations. It defines a surface which envelops all physically possible stress states in rate–independent plasticity. Stress states inside this contour cause only elastic deformations, while stress states on this yield surface give rise to elastic–plastic deformations. By definition, in rate–independent plastic stress states outside the yield contour f are not admissible.

Moreover, the von Mises yield function with J_2 flow theory for isotropic materials will be chosen as the yield criterion in the following numerical calculations, more details can be seen in the works (Ponthot, 2002; Berke, 2008). This yield criterion is frequently assumed for metals and alloys (Mahnken and Stein, 1996a; Brünig, 1999). Furthermore, it offers the numerical advantage that the gradients of the von Mises yield surface, which are used for the numerical solution procedure, are always uniquely defined. Mathematically, in case of an isotropic hardening, the yield function is expressed as,

$$f(\boldsymbol{\sigma}, \sigma_v) = \bar{\sigma} - \sigma_v = 0, \tag{2.11}$$

where,

$\bar{\sigma}$ is the effective stress, i.e. $\bar{\sigma} = \sqrt{\frac{3}{2}\mathbf{s} : \mathbf{s}}$;

$\mathbf{s}$ is the deviator of the stress tensor;

σ_v is the current yield stress.

However, as many metals and alloys exhibit different hardening behaviour, it appears necessary to study indentation responses affected by hardening. This means that the phenomena exhibited by not only the classical isotropic hardening behaviour, but also by the kinematic hardening behaviour, such as Bauschinger effect and ratcheting effect, need to be investigated (Huber and Tsakmakis, 1998; Dettmer and Reese, 2004). If it is assumed that the materials have non-linear kinematic hardening, according to the Armstrong-Frederick law with the non-linear kinematic hardening parameters, H_{kh} and H_{kb}, the relationship between back stress α and effective plastic strain $\bar{\varepsilon}_p$, is described as

$$\overset{\nabla}{\alpha} = \frac{2}{3} H_{kh} D_{ij}^{p} - H_{kb} \dot{\bar{\varepsilon}}_p \alpha . \tag{2.12}$$

Therefore, in the yield function, the effective stress $\bar{\sigma}$ can be rewritten by

$$\bar{\sigma} = \sqrt{\frac{3}{2}(\mathbf{s}-\boldsymbol{\alpha}) : (\mathbf{s}-\boldsymbol{\alpha})} . \tag{2.13}$$

While $f < 0$, there is elastic material behaviour. For $f = 0$, rate-independent elasto-plastic material behaviour takes place. Herein, plastic hardening with an associative flow rule is considered, including non-linear isotropic and non-linear kinematic hardening. The evolution of the yield stress, σ_v can be closely approximated by the Voce-type hardening law,

$$\sigma_v = \sigma_y^0 + Q[1 - \exp(-\xi \bar{\varepsilon}_p)] , \tag{2.14}$$

where σ_y^0 is the initial yield stress. Q and ξ are non-linear isotropic hardening parameters. In addition, if the materials are considered with viscosity, e.g. if the viscosity is described as the Cowper-Symonds law (Lim, 2007),

$$\sigma_{visco} = \sigma_0 \left(\frac{\dot{\bar{\varepsilon}}_{vp}}{D} \right)^{\frac{1}{m}} , \tag{2.15}$$

where, σ_0 is the quasi-static flow stress. $\dot{\bar{\varepsilon}}_{vp}$ is the rate of effective viscoplastic strain. D is a constant and m is the viscosity exponent. A new constraint is defined in the viscoplastic range according to (Ponthot, 2002),

$$\bar{f} = \bar{\sigma} - \sigma_v - \sigma_{visco} = 0 . \tag{2.16}$$

In the elastic regime, both f and $\bar{f}$ are equivalent because in this case, $\dot{\bar{\varepsilon}}_{vp} = 0$ and $\bar{\sigma} \le \sigma_v$. So that one has $\bar{f} \le 0$.

2.2.2. Sensitivity analysis

Sensitivity analysis is a well established field of mechanics. The general formulations of the sensitivity analyses are already developed in both continuum and discretized format (Tsay and Arora, 1990; Kim and Huh, 2002; Stupkiewicz et al., 2002). Sensitivity analysis plays an important role in inverse and identification studies which normally involve numerical optimization algorithms. In inverse and identification studies, an objective function is defined first to quantify the difference between experimentally measured and analytically predicted response data. Then, sensitivity analyses are used to evaluate the gradients of the error function with respect to the model parameters which are used in the analysis. Subsequently, the parameters of the model will be modified according to the evaluation of the gradients of the error function in order to minimize the difference between the predicted and experimental response data.

In fact, a large number of problems can be quantified and evaluated thanks to sensitivity analysis. For instance, sensitivity analysis is presented for the metal forming processes (Antunez and Kleiber, 1996), for thermal mechanical system (Song et al., 2003; Song et al., 2004), as well as it was used by (Bocciarelli and Bolzon, 2007) to show that the proposed methodology is accurate and effective in identification of the constitutive parameters of coatings. Besides, some applications and recent developments of sensitivity analysis can be seen from (Smith et al., 1998c; Smith et al., 1998a; Smith et al., 1998b; Cao et al., 2003; Rauchs, 2006).

Generally speaking, three kinds of sensitivity analysis methods are widely used in mechanical problems, namely, the direct differentiation method (DDM) (Kermouche et al., 2004; Huang and Lu, 2007), the adjoint state method (ASM) (Tsay and Arora, 1990; Zhang et al., 2007d), and the finite difference method (FDM) (Kim and Huh, 2002).

As far as FDM is concerned, it is conceptually the simplest approach to the determination of sensitivities. However the accuracy of FDM strongly depends on the perturbation size according to the involved problem. For instance, the accuracy based on the magnitude of the perturbation-truncation errors will be significant if the perturbation is too large. On the other hand, the round-off errors are disastrous if the perturbation is too small (Chandra and Mukherjee, 1997). Thus, if the sensitivity is calculated by FDM, the oscillatory tendency may be extremely severe and the solution cannot be used for optimization analysis (Kim and Huh, 2002).

The DDM is carried out by computing variations of the equilibrium equation for the continuum with respect to the design variables and the solution of sensitivity equations. It is designed to yield exact expression for the sensitivity and avoid the use of finite differences. Compared to FDM, DDM is characterised by more reliability, accuracy and versatility (Kim and Huh, 2002).

The ASM is an exact approach to the determination of sensitivity and does not involve finite differencing. In this approach, an adjoint system must be prescribed in addition to the physical system. One auxiliary system is defined for each design function, rather than for each design parameter. The sensitivity of the function with respect to the entire design vector is directly calculated.

Although the original physical system is governed by nonlinear equations, the solution of linear equations as a part of the sensitivity calculations is necessary to both DDM and ASM. The choice of the accurate method depends on computational efficiency. According to the investigations (Tsay and Arora, 1990), the ratio between active constrains and design variables as well as the relative difficulty of obtaining the adjoint solutions versus the sensitivity solutions decide that which approaches had better be chosen. Detailed information and several analytical examples to verify and show the procedures of design sensitivity analysis are presented in the following works (Tsay and Arora, 1990; Tortorelli and Michaleris, 1994).

In the following parts, a concise explanation is given to review the sensitivity analysis design.

2.2.2.1. General theory

According to (Tsay and Arora, 1990; Tortorelli and Michaleris, 1994; Smith et al., 1998c), if a linear steady-state system is presumed, the response $\mathbf{u}(\mathbf{x})$ can be evaluated through the governing equation:

$$\mathbf{K}(\mathbf{x})\mathbf{u}(\mathbf{x}) = \mathbf{P}(\mathbf{x}). \tag{2.17}$$

Herein, $\mathbf{K}(\mathbf{x})$ is a linear differential operator in space and is an explicit function of n-dimensional design vector $\mathbf{x}$. The elements of $\mathbf{x}$ comprise the set of design parameters and are used to describe the material response, sectional properties, load data etc. the load data $\mathbf{P}(\mathbf{x})$ is also an explicit function of the design $\mathbf{x}$. To solve the above equation, the Newton-Raphson iteration is frequently used because it exhibits quadratic terminal convergence (Tsay and Arora, 1990; Smith et al., 1998c).

In a design problem, assuming that an objective function F is defined through the function G, the cost and constraint functions of a process with generalized response function are quantified as

$$F(\mathbf{x}) = G(\mathbf{u}(\mathbf{x}), \mathbf{x}). \tag{2.18}$$

Hence, G is both implicitly and explicitly dependent on $\mathbf{x}$. Assuming sufficient smoothness, the design sensitivity of F with respect to the design variable $\mathbf{x}$ is calculated as,

$$\frac{DF}{D\mathbf{x}} = \frac{\partial G}{\partial \mathbf{u}} \frac{D\mathbf{u}}{D\mathbf{x}} + \frac{\partial G}{\partial \mathbf{x}}. \tag{2.19}$$

Here, the difficulty of evaluating this expression arises from the presence of the implicit sensitivity $Du/D\mathbf{x}$, which is generally unknown.

2.2.2.2. Finite difference sensitivity analysis

The finite difference method is the simplest approach to compute the sensitivity of the objective function. In this method, the finite difference sensitivity is derived from the first-order Taylor polynomial, which is defined as

$$F(x_i + \Delta x_i) = F(x_i) + \frac{\partial F(x_i)}{\partial x_i}\Delta x_i + O(\Delta x_i^2). \tag{2.20}$$

Therefore, if the difference is defined as the forward difference, it is approximated as below,

$$\frac{\partial F}{\partial x_i} \approx \frac{F(x_i + \Delta x_i) - F(x_i)}{\Delta x_i}. \tag{2.21}$$

The truncation error of this approximation is derived from Taylor's theorem as

$$O(\Delta x_i^2) = \frac{\partial^2 F(x_i)}{\partial^2 x_i}\frac{(\Delta x_i)^2}{2!} + \ldots + \frac{\partial^n F(x_i)}{\partial^n x_i}\frac{(\Delta x_i)^n}{n!}. \tag{2.22}$$

It is clearly seen that if the perturbation of Δx_i is very small, the error $O(x_i)$ tends to zero and the sensitivity computed by FDM is reliable. However, if Δx_i is too small, the numerical round-off error will erode the accuracy of the computations.

Similarly, the backward difference can be approximated as below,

$$\frac{\partial F}{\partial x_i} \approx \frac{F(x_i) - F(x_i - \Delta x_i)}{\Delta x_i}. \tag{2.23}$$

Both the forward and the backward differences are first-order accurate. Therefore, in practical applications, sometimes the central difference is used because it is a second-order accurate approximation. The objective function is written into the form of the second-order Taylor polynomial as below,

$$F(x_i + \Delta x_i) = F(x_i) + \frac{\partial F(x_i)}{\partial x_i}\Delta x_i + \frac{1}{2}\frac{\partial^2 F(x_i)}{\partial^2 x_i}\Delta x_i^2 + O(\Delta x_i^3), \tag{2.24}$$

$$F(x_i - \Delta x_i) = F(x_i) - \frac{\partial F(x_i)}{\partial x_i}\Delta x_i + \frac{1}{2}\frac{\partial^2 F(x_i)}{\partial^2 x_i}\Delta x_i^2 - O(x_i^3). \tag{2.25}$$

Thus, the central difference approximation

$$\frac{\partial F}{\partial x_i} = \frac{F(x_i + \Delta x_i) - F(x_i - \Delta x_i)}{2\Delta x_i} + O(\Delta x_i^3), \tag{2.26}$$

is second-order accurate.

2.2.2.3. Direct differentiation sensitivity analysis

The sensitivity of F shown in Eq. (2.19) can be written in component form,

$$\frac{DF}{Dx_i} = \frac{\partial G}{\partial \mathbf{u}} \frac{D\mathbf{u}}{Dx_i} + \frac{\partial G}{\partial x_i} \ , \tag{2.27}$$

For the $i = 1,2,3,...,N$ components of $\mathbf{x}$. In order to calculate the derivative of $D\mathbf{u}/Dx_i$, the system equation Eq. (2.17) has to be differentiated with respect to the individual design parameters, i.e.

$$\frac{D\mathbf{K}(\mathbf{x})}{Dx_i}\mathbf{u}(\mathbf{x}) + \mathbf{K}(\mathbf{x})\frac{D\mathbf{u}(\mathbf{x})}{Dx_i} = \frac{D\mathbf{P}(\mathbf{x})}{Dx_i} \ , \tag{2.28}$$

which is rewritten as

$$\frac{D\mathbf{u}(\mathbf{x})}{Dx_i} = \left[\mathbf{K}(\mathbf{x})\right]^{-1}\left[\frac{D\mathbf{P}(\mathbf{x})}{Dx_i} - \frac{D\mathbf{K}(\mathbf{x})}{Dx_i}\mathbf{u}(\mathbf{x})\right] . \tag{2.29}$$

The above pseudo problem can be efficiently computed because the decomposed stiffness matrix, $\left[\mathbf{K}(\mathbf{x})\right]^{-1}$ is available from the governing equation Eq. (2.17). Afterwards, the derivatives $D\mathbf{u}/Dx_i$ are determined by forming the pseudo load vector,

$$\frac{D\mathbf{P}(\mathbf{x})}{Dx_i} - \frac{D\mathbf{K}(\mathbf{x})}{Dx_i}\mathbf{u}(\mathbf{x})$$

and then by performing a backward substitution. This process is repeated for N times, i.e. once for each of the N design variables. Thus, once $D\mathbf{u}/Dx_i$ are computed, the sensitivity $\partial F/\partial x_i$ is evaluated from Eq. (2.27).

2.2.2.4. Adjoint state sensitivity analysis

In the adjoint state sensitivity analysis, adjoint variables, i.e. Lagrange multipliers are introduced to eliminate the implicit sensitivities $D\mathbf{u}/Dx_i$ from Eq. (2.19). An augmented function is defined as below combining Eq. (2.17) and Eq. (2.18),

$$\widehat{F}(\mathbf{x}) = G(\mathbf{u}(\mathbf{x}), \mathbf{x}) - \boldsymbol{\lambda}(\mathbf{x}) \bullet \left[\mathbf{K}(\mathbf{x})\mathbf{u}(\mathbf{x}) - \mathbf{P}(\mathbf{x})\right], \tag{2.30}$$

where $\boldsymbol{\lambda}$ acts as the Lagrange multipliers. Here $\widehat{F}(\mathbf{x}) = F(\mathbf{x})$, since all admissible designs $\mathbf{x}$ must satisfy the system equation. Thus an admissible solution $\mathbf{x}$ leads to the fact that $\mathbf{K}(\mathbf{x})\mathbf{u}(\mathbf{x}) - \mathbf{P}(\mathbf{x})$ equals zero. The differentiation of $\widehat{F}$ with respect to the design variable x_i is written as,

$$\begin{aligned}\frac{D\widehat{F}}{Dx_i} &= \frac{\partial G(\mathbf{u}(\mathbf{x}),\mathbf{x})}{\partial \mathbf{u}}\frac{D\mathbf{u}}{Dx_i} + \frac{\partial(\mathbf{u}(\mathbf{x}),\mathbf{x})}{\partial x_i} \\ &\quad - \frac{D\boldsymbol{\lambda}(\mathbf{x})}{Dx_i}\bullet\left[\mathbf{K}(\mathbf{x})\mathbf{u}(\mathbf{x}) - \mathbf{P}(\mathbf{x})\right] \\ &\quad - \boldsymbol{\lambda}(\mathbf{x})\bullet\left[\frac{D\mathbf{K}(\mathbf{x})}{Dx_i}\mathbf{u}(\mathbf{x}) + \mathbf{K}(\mathbf{x})\frac{D\mathbf{u}(\mathbf{x})}{Dx_i} - \frac{D\mathbf{P}(\mathbf{x})}{Dx_i}\right],\end{aligned} \tag{2.31}$$

where, it is noted again that $D\widehat{F}/Dx_i = DF/Dx_i$, because the last two quantities in between parentheses,

$\mathbf{K}(\mathbf{x})\mathbf{u}(\mathbf{x}) - \mathbf{P}(\mathbf{x})$ and $\dfrac{D\left[\mathbf{K}(\mathbf{x})\mathbf{u}(\mathbf{x}) - \mathbf{P}(\mathbf{x})\right]}{Dx_i}$,

equal zero. Here, the second term is eliminated using Eq. (2.17). Thus Eq. (2.31) is rearranged as

$$\frac{D\widehat{F}}{Dx_i} = \left[\frac{\partial G(\mathbf{u}(\mathbf{x}),\mathbf{x})}{\partial x_i} - \boldsymbol{\lambda}(\mathbf{x})\bullet\left(\frac{D\mathbf{K}(\mathbf{x})}{Dx_i}\mathbf{u}(\mathbf{x}) - \frac{D\mathbf{P}(\mathbf{x})}{Dx_i}\right)\right] + \frac{D\mathbf{u}(\mathbf{x})}{Dx_i}\bullet\left[\frac{\partial G(\mathbf{u}(\mathbf{x}),\mathbf{x})}{\partial \mathbf{u}} - \mathbf{K}^T(\mathbf{x})\boldsymbol{\lambda}(\mathbf{x})\right], \tag{2.32}$$

where $()^T$ denotes the transpose operator. Given that $\boldsymbol{\lambda}$ is arbitrary, it can be selected to eliminate the coefficient of the $D\mathbf{u}/Dx_i$ term. The resulting adjoint response $\boldsymbol{\lambda}$ is

$$\boldsymbol{\lambda}(\mathbf{x}) = \mathbf{K}^{-T}(\mathbf{x})\frac{\partial G(\mathbf{u}(\mathbf{x}),\mathbf{x})}{\partial \mathbf{u}}. \tag{2.33}$$

Once the adjoint response is evaluated, the implicit response derivative $D\mathbf{u}/Dx_i$ is annihilated and Eq. (2.32) is reduced to

$$\frac{D\widehat{F}}{Dx_i} = \left[\frac{\partial G(\mathbf{u}(\mathbf{x}),\mathbf{x})}{\partial x_i} - \boldsymbol{\lambda}(\mathbf{x})\left(\frac{D\mathbf{K}(\mathbf{x})}{Dx_i}\mathbf{u}(\mathbf{x}) - \frac{D\mathbf{P}(\mathbf{x})}{Dx_i}\right)\right], \tag{2.34}$$

which is the desired sensitivity.

2.2.2.5. Concluding remarks

The sensitivity analysis is defined as the gradient of the objective function with respect to the variable parameters. It is usually performed to estimate the influences of variable parameters upon the objective function, Sensitivity analysis has been mainly developed for the identification of material properties in experiments characterised by inhomogeneous stress fields (Mahnken and Stein, 1996b; Mahnken and Stein, 1996a; Constantinescu and Tardieu, 2001; Kim et al., 2001; Nakamura and Gu, 2007). Moreover, it is widely used to evaluate the influence of contact problems with friction (Kim et al., 2002; Stupkiewicz et al., 2002; Pelletier, 2006; Schwarzer et al., 2006), tip geometry and surface integrity (Warren and Guo, 2006).

In this thesis, sensitivity analysis relying on DDM is used. According to the investigation of (Mahnken and Stein, 1996a), DDM is preferred over ASM, because of its simplicity and because the linear update scheme of the DDM does not require a backward calculation. This method uses the same finite element model as the resolution of the direct deformation problem, and therefore the sensitivity analysis can be performed in parallel with the solution of the direct deformation problem. In fact, after the iterative resolution of the non-linear direct deformation problem over a time increment, DDM requires only a linear update for calculating the derivatives at the end of the time step. This leads to considerable savings in computing time compared to FDM, where one additional non-linear solution of the direct deformation problem is required for calculating the gradient with respect to each additional material parameter.

2.2.3. Optimization analysis

In order to identify the material parameter based on inverse analysis involving numerical optimization, an optimization strategy using the sensitivity analysis scheme is designed. According to the published papers, optimization methodology is often encountered in the traditional model calibration tasks, such as the optimal shape design (Antunez and Kleiber, 1996; Stupkiewicz et al., 2002; Zhang et al., 2007c), the boundary condition specification (Sergeyev and Mroz, 2000; Liang et al., 2007), the discretization strategy investigation (Zhang et al., 2007b), as well as material property assignment (Antunez and Kleiber, 1996; Song et al., 2004; Zhang et al., 2007b).

Currently, many optimization methods – e.g. genetic algorithms (Reid, 1996; Gosselin et al., 2009), simplex method (Pan, 1998; Wang et al., 2008), gradient-based methods like Gauss-Newton (Gavrus et al., 1996; Mahnken and Stein, 1996b), Levenberg-Marquardt (Gelin and Ghouati, 1994), and cascade optimization methods (Ponthot and Kleinermann, 2006) are widely used in various fields of industry. It is noted that genetic algorithms are often used in practice

because of their versatility. However, as a major drawback, this method is very time-consuming since in general many function evaluations (up to several hundred thousands) are necessary. Thus, for the reason of efficiency, optimization strategy is often based on gradient evaluation.

For instance, some researchers propose a quasi-Newton with SQP method (Sun, 1998; Wei et al., 2006) or quasi-Newton with BFGS method (Constantinescu and Tardieu, 2001) to determine the material parameters and some researchers use a Gauss-Newton type algorithm to find the optimal solution in the identification of rheological parameters (Gavrus et al., 1996). Other researchers (Gelin and Ghouati, 1994; Gerday, 2009) prefer to use a Levenberg-Marquardt algorithm in the identification of the material parameters. Recently, (Ponthot and Kleinermann, 2006) proposed a cascade optimization strategy using a different gradient-based optimization algorithms, in parameter identification and in shape optimization. The cascade optimization strategy has proved to be more efficient and robust in a variety of numerical applications.

Sensitivity analysis and numerical optimization are used together for the identification of material properties. For determining the material parameters from a constitutive law used in a numerical method (such as the finite element method), the differences between model and experiment must be quantified through an objective function. Normally, the objective function is calculated as the sum of squared differences between modelled and experimental results (Mahnken and Stein, 1996b; Constantinescu and Tardieu, 2001; Rauchs, 2006; Luo and Lin, 2007). Subsequently, it is minimized in order to provide the best match between experimental data and simulated data in specific optimal approach strategies. For example, (Mahnken and Stein, 1996a; Forestier et al., 2002; Forestier et al., 2003; Rauchs, 2006) used a Gauss-Newton procedure; (Constantinescu and Tardieu, 2001) used quasi-Newton with BFGS algorithm and (Bocciarelli and Bolzon, 2007; Bocciarelli and Maier, 2007) used the Trust Region (TR) algorithm to identify material properties.

2.3. Applications of indentation testing

2.3.1. Calculations of hardness and Young's modulus

During an indentation measurement, the process of loading takes place when the indenter is pressed into a specimen – see Fig. 2. 5(a). First, an elastic deformation occurs in the specimen. Following the load increase, the specimen enters into the plastic regime. After the maximum load or the optional hold period, the applied load is reduced. Generally, the loading and unloading curves are both nonlinear. However, in the past, some researchers (Doerner and Nix, 1986) claimed that the unloading curve can be fitted into a linear curve. Several years later, other authors (Oliver and Pharr, 1992; Bolshakov et al., 1994; Pharr and Bolshakov, 2002;

Schwarzer, 2006) tested a large number of materials. They concluded that the unloading curves were rarely linear, even in the initial stages of unloading.

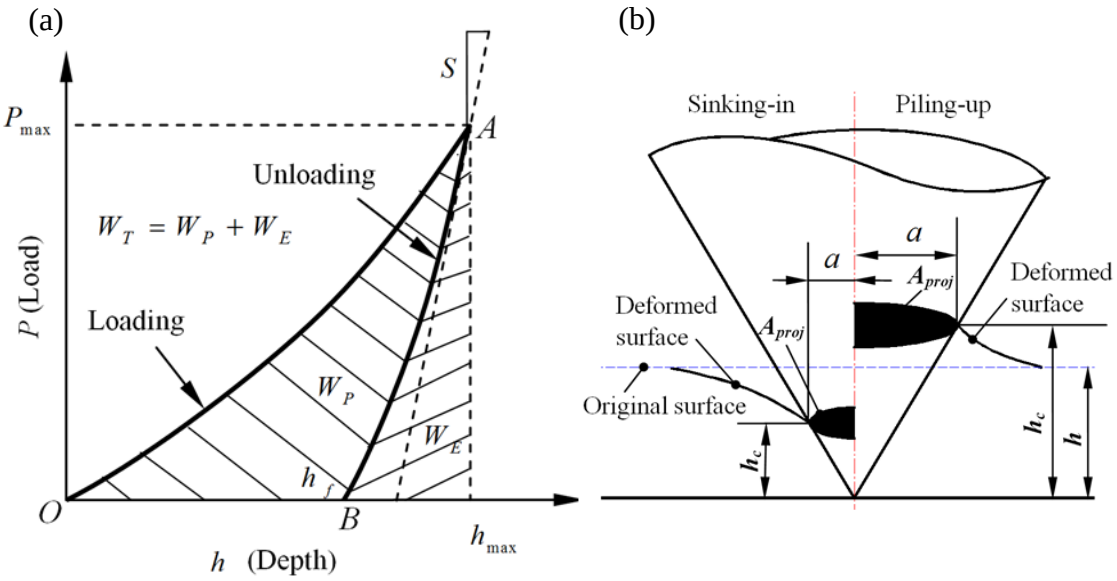

Fig. 2. 5. (a) Schematics of the load versus indentation depth curve (Tuck et al., 2001); (b) Indentation profiles with sinking-in (left) and piling-up (right) (Bucaille et al., 2002).

Fig. 2. 5(b) shows a cross-section of the profile of a specimen surface at full loading for a typical elastic-plastic indentation. The recorded residual impression and penetration depth are primarily used to determine the hardness of a material which is defined as the ratio of the maximum indentation load, P, and the contact surface area, A. This is why the unit of hardness is given in $N/m^2 = Pa$. In contrast to the classic indentation methods, which use nonstandard units such as HV, HB, or HR, nanoindentation makes specific use of SI units (Albrecht et al., 2005). By recording the data of the whole indentation procedure, the hardness and the reduced elastic modulus can be calculated according to the following methods (Oliver and Pharr, 1992):

$$H = \frac{P_{\max}}{A_{proj}}, \tag{2.35}$$

$$E_r = \sqrt{\frac{\pi}{A_{proj}}}\frac{S}{2\beta_c}, \tag{2.36}$$

where, A_{proj} is the projected area of the hardness impression. $P_{\max}$ is the maximum indentation load. E_r is the so-called reduced modulus which includes the material parameters of the indenter (E_i, υ_i) and of the investigated material (E, υ). They can be represented as below (Oliver and Pharr, 1992):

$$\frac{1}{E_r} = \frac{1-\upsilon^2}{E} + \frac{1-\upsilon_i^2}{E_i}. \tag{2.37}$$

The indenter is often presumed as rigid. If the indenter is made of diamond (Young's modulus $E_i = 1141\,GPa$, Poisson's ratio $\upsilon_i = 0.07$), its elastic modulus is normally ten times larger than the indented materials. If we want to calculate *E* according to Eq. (2.37), the value of υ must be known. In practice, if $\upsilon = 0.3 \pm 0.01$ is supposed for metals, the error on Young's modulus E is within 3.3%. This means that if the value of υ is unknown before the measurement, it must be assumed to be 0.3.

In Eq. (2.36), β_c is a constant which is specific to the indenter geometry. If the indenter is conical, Berkovich or Vickers, $\beta_c = 1.0$, 1.034 or 1.012 respectively (Pharr, 1998; Poon et al., 2008).

$$S = \left.\frac{dP}{dh}\right|_{h_{\max}}$$

is referred to as the initial unloading stiffness. It can be obtained by fitting a straight line to a fraction of the upper portion of the unloading curve and using its slope as a measure of the stiffness. The problem is that, for nonlinear unloading data, the measured stiffness depends on how many of the data are used in the fit. (Oliver and Pharr, 1992) propose to describe the unloading data for the stiffness measurement as

$$P = B(h - h_f)^{m_s}, \tag{2.38}$$

where the constants B, m_s, and h_f are all determined by a least squares fitting procedure. Then the initial unloading stiffness S can be calculated as

$$S = \left(\frac{dP}{dh}\right)_{h=h_{\max}} = Bm(h_{\max} - h_f)^{m_s - 1}, \tag{2.39}$$

It is not sure that Eq. (2.39) would be suitable for all the unloading curves of the materials such as for the thin film on the substrate. If the whole unloading curve is used in the fit, a large error may occur. Therefore, only 25%~50% of the unloading data from the peak load are usually used in the fit.

In order to calculate the material hardness according to Eq. (2.35), the projected area A_{proj} has to be calculated. In practice, A_{proj} is directly related to the contact depth, h_c (see Fig. 2. 5(b)). According to the investigation of (Oliver and Pharr, 1992), the relationship between the contact depth h_c and the displacement of the indenter h is described as follows,

$$h_c = h - h_f = h - \varepsilon_g \frac{P_{\max}}{S}, \tag{2.40}$$

where, ε_g is a geometrical parameter – e. g. for a flat punch, $\varepsilon_g = 1$. For a conical indenter, $\varepsilon_g = 0.72$. For a spherical or pyramidal indenter, $\varepsilon_g = 0.75$. Thus, the projected contact area A_{proj}

can be calculated according to the function, $A_{proj}(h_c) = f(h_c)$. According to the investigation of (Oliver and Pharr, 1992), the area function for a perfect sharp Berkovich indenter equals

$$A_{proj}(h_c) = 24.5h_c^2 . \tag{2.41}$$

In fact, no indenter has an exact perfect sharp tip, thus the relationship between A_{proj} and h_c must be modified as proposed in (Oliver and Pharr, 1992; Balint et al., 2006):

$$A_{proj}(h_c) = 24.5h_c^2 + \sum_{i=0}^{7} C_i h_c^{1/2^i} \quad , \tag{2.42}$$

where the constant, C_i take different values according to the different indenter geometry. Normally for a given indenter tip, they are calibrated using different reference materials, such as the fused silica, steel EN31, copper and tin, the hardness and the mechanical properties of which are already known (Albrecht et al., 2005).

Hence it becomes possible to determine $A_{proj}(h_c)$ for any value of h_c. In turns a hardness value can immediately be obtained. Thus if the initial unloading stiffness *S* and the projected area A_{proj} are calculated, the hardness and the elastic modulus can be obtained by Eq. (2.35) and Eq. (2.37).

In addition, after Oliver and Pharr, other researchers (Venkatesh et al., 2000; Tuck et al., 2001; Zhao et al., 2006b) proposed to calculate the material hardness directly from the energy of indentation without the need for estimating the penetration depth. The hardness of plastic material is evaluated through the work-of-indentation as follows (Tuck et al., 2001):

$$H_p = \frac{k_c P_{\max}^3}{9W_P^2} \ , \tag{2.43}$$

where $P_{\max}$ is the maximum load. W_P is the plastic work – see Fig. 2. 5(a). k_c is a constant which takes into account the indenter geometry and the choice of hardness definition. For example, $k_c = 0.0378$ for the four-sided Vickers pyramid, or $k_c = 0.0408$ for the three-sided Berkovich pyramidal indenter with identical depth-to-area relationship (Tuck et al., 2001).

Once the hardness, H, is known, it can be used to assess the yield stress of the material. According to the investigation of (Albrecht et al., 2005), H and the maximum shear stress, $\tau_{\max}$, are correlated as below:

$$H = 2\tau_{\max}(1+\theta) , \tag{2.44}$$

where, θ expressed in radians is the equivalent cone angle of the Berkovich indenter (equivalent to 70.3°). If the von Mises yield criterion is used, one can find an equation to extract the initial yield stress, σ_y^0:

$$\sigma_y^0 = H\frac{\sqrt{3}}{2(1+\theta)} , \tag{2.45}$$

2.3.2. Fracture toughness

Indentation testing is used to initiate and control the fracture in brittle materials. In order to investigate the fracture toughness, the hardness and the elastic modulus of the studied material must be obtained. Then, as shown in Fig. 2. 6, radial fractures in the material are caused by a Cube-corner indenter. The relationship between fracture toughness ($MPa\,m^{1/2}$) and the length of radial fracture is represented as below (Lee et al., 2005),

$$K_c = a_{ec}\left(\frac{E}{H}\right)^{1/2}\left(\frac{P_{\max}}{C_F^{3/2}}\right), \tag{2.46}$$

where $P_{\max}$ is the maximum force applied to Cube-corner indenter, C_F is the length of the radial fracture, a_{ec} is an experimental coefficient relative to the shape of the indenter. Given that the tip of the Cube-corner indenter is sharper than Berkovich indenter's, larger stresses and strains around the indenter may be produced. Accordingly, it is easier to cause fractures and to make them extend.

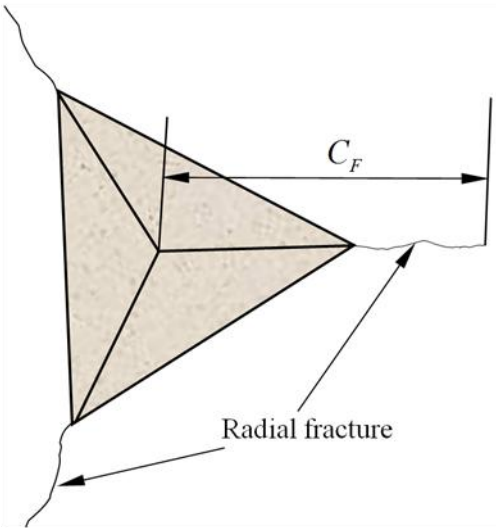

Fig. 2. 6. The radial fractures in the material are caused by a Cube-corner indenter (Zhang and Yang, 2002).

2.3.3. Viscoelastic behaviour

Indentation testing allows the researchers to evaluate the mechanical properties of viscoelastic materials. (Oliver and Pharr, 1992; Vandamme and Ulm, 2006) established a simple contact model using a spring (the initial unloading stiffness is S) and damping (the damping

coefficient is D_s, which depends on the materials and conditions at the contacted surfaces). Thus, the storage modulus E' and the loss modulus E'' are written as below (Odegard et al., 2005; Singh et al., 2005):

$$E' = \frac{\sqrt{\pi}}{2\beta_c}\frac{S}{\sqrt{A}}; \tag{2.47}$$

$$E'' = \frac{\sqrt{\pi}}{2\beta_c}\frac{D_s\omega}{\sqrt{A}}, \tag{2.48}$$

where ω is the excitation frequency.

2.3.4. Creep parameter

Indentation testing can also be used to evaluate material's creep behaviour. In the uniaxial tensile experiment for creep, the relationship between temperature, stress and creep rate can be described as following (Gao and Takemoto, 2006):

$$\dot{\varepsilon} = \alpha_{mc}\sigma^{n_c}\exp\left(-Q_c/R_cT\right), \tag{2.49}$$

where α_{mc} is a material constant, σ is the applied stress, n_c is the creep stress index, Q_c is the activation energy, R_c is the universal gas constant, T is temperature. For most of metals, the typical range of n_c is 3~5. The Eq. (2.49) can be rewritten as

$$\dot{\varepsilon} = \alpha_i H^{n_c}\exp\left(-Q_c/R_cT\right). \tag{2.50}$$

Eq. (2.50) is the equivalent expression of the indentation creep. Here $\dot{\varepsilon} = \dot{h}/h$ is the indentation strain rate, α_i is a material constant, and average contact pressure $H = P/A$ is equivalent to the stress.

2.4. Methods for the identification of material properties

2.4.1. Experimental methods

2.4.1.1. Measurement cycles

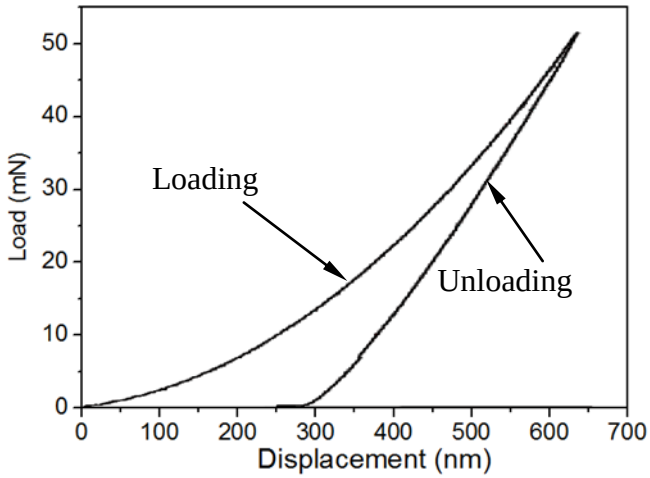

Fig. 2. 7. Load-displacement curve obtained in a nanoindentation experiment with Berkovich indenter for fused silica (Fischer-Cripps, 2002).

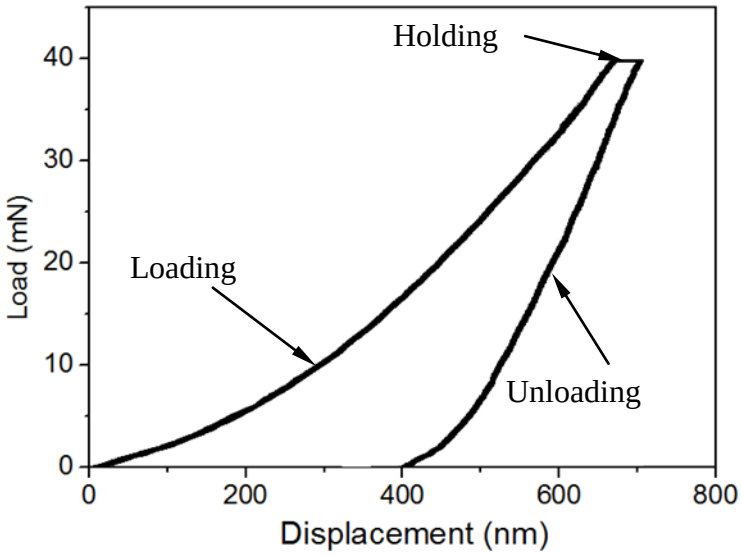

Fig. 2. 8. Load-displacement curve for fused silica at 200 ℃ (Fischer-Cripps, 2002).

For different measuring aims, the measurement cycles will be designed in different forms. A typical indentation measurement cycle consists of an application of load followed by an unloading sequence. Most often, the indented materials are measured by using a loading-unloading cycle (see Fig. 2. 7). Concerning the materials characterised by viscous properties, the load will be held at maximum for a short time before performing the unloading cycle (see Fig. 2. 8). The data of the hold period can be used to measure the creep within the specimen or the thermal drift of the apparatus during a test. Besides, repeatable loading-(holding)-unloading cycles with a fixed maximum load or with varying maximum loads may also be used, see Fig. 2. 9 (Fischer-Cripps, 2002).

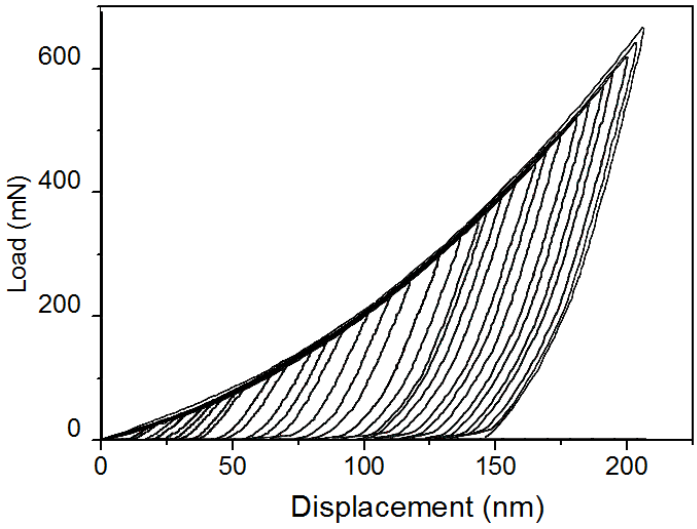

Fig. 2. 9. Load-displacement curves for varying maximum load on fused silica (Fischer-Cripps, 2002).

2.4.2. Numerical simulation methods

Thanks to the current increasing computing power, the numerical simulation method, as one of the most powerful methods, is widely used to resolve many engineering problems. In indentation investigations, the numerical simulation method is also useful for the understanding of the complex physics involved at small scales. For example, based on the numerical simulation methods, some researchers use of the forward method to calculate the hardness (Kizler and Schmauder, 2007) and the Young's modulus (Lee et al., 2005), as well as on the use of the inverse method to evaluate the strain-stress relation (Bouzakis et al., 2001) and analyze the elasto-plastic and the elasto-viscoplastic behaviours (Cheng et al., 2005; Giannakopoulos, 2006; Vandamme and Ulm, 2006).

The finite element method (FEM) has been often used to evaluate material parameters. Indeed, the FEM and commercial finite element codes such as ABAQUS, ANSYS, and MARC have developed significantly. Even the high local strain and the stress involved in indentation testing, the nonlinearities in the material, geometry and contact can be simulated accurately using the FEM (Soare et al., 2004; Komvopoulos and Yang, 2006). The material behaviours like elasto-viscoplastic constitutive laws or other highly sophisticated constitutive laws have also been developed thanks to the FEM. In addition, all the physical parameters such as the constitutive relations of material can be changed easily thanks to some algorithms. Thus, the correlations of the physical parameters and the indentation results will be studied. In order to predict the deformation behaviours – namely, the piling-up, the sinking-in, and the indentation depth during unloading – of hard-brittle materials, such as amorphous silicon and Pyrex 7740 glass (borosilicate), (Youn and Kang, 2005) performed indentation simulations for various tip radii (40, 100, 200 nm), half-angle of the conical indenter (55°, 60°, 65°), and the indenter geometries (conical, Berkovich, spherical) using the finite element method. Similar numerical simulations are also utilized by other researchers (Lee et al., 2005; Hernot et al., 2006; Pelletier, 2006) to investigate material property.

2.4.2.1. Inverse analysis

The problems solved by indentation testing are generally divided into two kinds. The first one is the so-called “forward problem” (Dao et al., 2001), and the second one is the “inverse problem” (Bolzon et al., 2004). Thanks to the forward method, a unique indentation response (e.g. $P-h$ curve) may be calculated on the basis of a given set of material properties (e.g. E and strain-stress relation) (Alcalá et al., 2000; Chen et al., 2007). As for the inverse method, it enables us to extract the material properties from a given set of experimental indentation data (Forestier et al., 2003; Bolzon et al., 2004; Bocciarelli et al., 2005; Gouldstone et al., 2007). The relationship between these two algorithms can be seen in Fig. 2. 10.

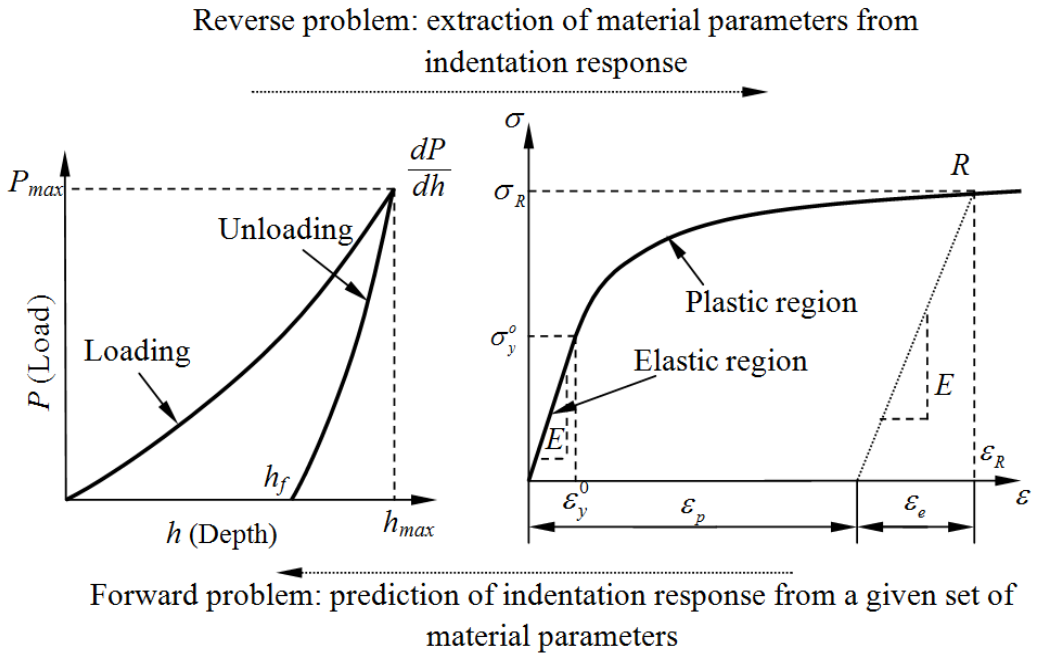

Fig. 2. 10. Graphic depiction of the forward and inverse problems in indentation for elasto-plastic materials (Gouldstone et al., 2007).

In practice, inverse methods often used in engineering design are numerical optimization methods, artificial neural networks-based methods and response surface method. They all have in common that they require a large number of calculations of a numerical model with varying parameters. Recently, the inverse methods involving the numerical modelling of the indentation test were widely used to determine the material parameters. For instance, (Constantinescu and Tardieu, 2001) used a gradient-based numerical optimization method to identify an elasto-viscoplastic constitutive law. In addition, some researchers identified the Poisson's ratio (Huber et al., 2001; Huber and Tsakmakis, 2001) and the plasticity model (Huber and Tsakmakis, 1999b; Huber and Tsakmakis, 1999a; Huber et al., 2002) by using artificial neural networks (ANN).

Considering the solution to the associated inverse problem, the artificial neural networks which are derived from the modelling of the human brain have recently become attractive tools. As flexible functions, artificial neural networks are widely used to solve complex inverse problems in computational mechanics. A highly parallel structure which consists of an interconnected group of the artificial neurons usually is designed for a neural network. Each artificial neuron has multiple inputs and a single output value. The artificial neuron processes information using a connection approach to mimic the biological brain neuron. According to the neural networks method, the so-called training patterns have to be presented in the networks (Huber et al., 2001; Huber and Tsakmakis, 2001). They can be trained to approximate any unique relation given by a number of examples. Moreover, they can be used as computer models to represent

multidimensional nonlinear problems since they often occur in the context of indentation and the identification of mechanical properties. The particular ability of neural networks is that they provide an effective way to approximate strongly nonlinear relationships between inputs and outputs or to find patterns in data (Tyulyukovskiy and Huber, 2007).

2.5. A method for the assessment of the correlation of the material parameters

In order to identify the material parameters from the $P-h$ curve registered during the loading and the unloading processes in an experiment, the inverse analysis stated in the previous section and based on the numerical optimization algorithm should be performed. The key idea of this procedure is to model the indentation test with a numerical method, i.e. the finite element method, using a starting set of material parameters and quantifying the difference between the modelled indentation curve and the experimental curve through an objective function. Subsequently, the material parameters used in the numerical model are updated using some algorithms from the numerical optimization in order to minimize the objective function. Once they lead to a good agreement between the experimental and the numerical results, the procedure will be stopped.

However, in this procedure, it was found that some material parameters are strongly coupled with each other. This parameter correlation leads to a difficulty to obtain unique and accurate material parameters. According to the investigations (Mahnken and Stein, 1996b; Rauchs, 2008), the viscosity parameters or the separation of isotropic and kinematic hardening are difficult to obtain and the reliability of the identified results is poor because of the strong parameter correlation. This stems from the fact that, in indentation tests, some physical phenomena inherent to the constitutive laws may not affect the experimental curves in a significant or a distinguishable way.

For these reasons, it is absolutely essential to find ways to reduce the correlation of the material parameters in order to obtain stable and unique material parameter results. Some improvement has been achieved by including additional experimental data in the objective function, namely, the residual imprint mappings of the residual imprint remaining after the load removal in the indentation tests (Bolzon et al., 2004; Bocciarelli et al., 2005). Residual imprint mappings include information about the sinking-in or the piling-up, which facilitates the quantification of plastic material behaviour. The deformation of the specimen surface around the indenter tip during the loading is of the outmost importance. However, this information is only available after removal of the indenter because the indenter tip itself shields that region from access by measurement devices during indentation experiment.

In the following parts, the method used for assessing the correlations of the material parameters is described.

2.5.1. Material parameter identification and correlation

Once a $P-h$ curve is obtained by a numerical model, the objective function can be calculated as the difference between the experimental and the modelled displacement-into-surface $\bar{h}$ and h respectively, which are the functions of the independent load, P:

$$F=\frac{1}{2}\sum_{i=1}^{N}\left[h(P_i)-\bar{h}(P_i)\right]^2, \tag{2.51}$$

where N is the number of the experimental data. $\bar{h}$ and h are the penetration depth of the indenter in the simulation and the experiment respectively. Thus, the sensitivity can be defined as the derivative of the objective function with respect to the material parameters x_j,

$$\frac{\partial F}{\partial x_j}=\sum_{i=1}^{N}\left[h(P_i)-\bar{h}(P_i)\right]\frac{\partial h(P_i)}{\partial x_j}. \tag{2.52}$$

Then, the Hessian matrix of the objective function can be computed as below,

$$H_{jk}=\frac{\partial^2 F}{\partial x_j \partial x_k}=\sum_{i=1}^{N}\left[\frac{\partial h(P_i)}{\partial x_j}\frac{\partial h(P_i)}{\partial x_k}+\left(h(P_i)-\bar{h}(P_i)\right)\frac{\partial^2 h(P_i)}{\partial x_j \partial x_k}\right]. \tag{2.53}$$

Given that the second term of the sum is known to adversely affect the convergence and is anyhow not easily available (Forestier et al., 2003; Papadimitriou and Giannakoglou, 2008; Rauchs, 2008; Liu et al., 2009; Amini and Rizi, 2010), an approximate Hessian matrix is generally used and it is approximated in the form,

$$\widetilde{H}_{jk}=\sum_{i=1}^{N}\frac{\partial h(P_i)}{\partial x_j}\frac{\partial h(P_i)}{\partial x_k}. \tag{2.54}$$

The material parameters are identified on the basis of gradient-based optimization method, which calculates the material parameters using,

$$x_j^{n+1}=x_j^n-\left(\widetilde{H}_{jk}\right)^{-1}\frac{\partial F}{\partial x_j}. \tag{2.55}$$

In indentation experiments, the identified hardness and the Young's modulus or other material parameters mainly depend on the contact area and the $P-h$ curve. Besides, the residual imprint mapping data are important for the identification of the material parameters, because they can describe the deformations of the piling-up and the sinking-in that occur on the surface of the specimen and which are directly dominated by the plastic properties of the specimen. The

residual imprint mapping data of the same specimen produced by different indenters are not identical or similar. Thus, it is necessary to extend the objective function by a term comprising the differences between the experimental and the modelled imprints. The corresponding objective function can be written as follows:

$$F = \frac{1}{2N}\sum_{i=1}^{N}\left[h(P_i)-\bar{h}(P_i)\right]^2 + \frac{1}{2M}\sum_{l=1}^{M}\left[\left(\bar{h}_{res}(\mathbf{r}^l)-\bar{h}_{res}(\mathbf{r}^0)\right)-\left(h_{res}(\mathbf{r}^l)-h_{res}(\mathbf{r}^0)\right)\right]^2, \quad (2.56)$$

Where $h_{res}(\mathbf{r}^l)$ is the vertical displacement of the contact surface at a set of M (M is relative to the numerical model) fixed radial locations $\mathbf{r}^l$ with respect to a chosen reference point. For example, the imprint centre called $\mathbf{r}^0$ can be used. In present study, the two terms in Eq. (2.56) have the same order of magnitude. Thus, no scaling factor is introduced in Eq. (2.56) and the two terms are only scaled with respect to the number of data, N and M.

If the Hessian matrix or the approximate Hessian matrix is available, its cosine matrix (it is defined in Eq. (2.57)) can be calculated and used to visualize the material parameter correlation. The cosine matrix can indicate whether the different sensitivities are co-linear or not. If the different sensitivities are co-linear, this means the effects of the corresponding material parameters to the objection function are difficulty decoupled. The approximated Hessian matrix can provide an accurate indication of the parameter correlation although it does not include the terms with the second order derivatives. This is due to the fact that the approximated Hessian matrix is equivalent to the Hessian matrix if the objective function exactly equals zero. Therefore, the approximated Hessian matrix can provide sufficient information to evaluate the parameter correlation. The cosine matrix of the Hessian matrix is defined according (Forestier et al., 2003; Rauchs, 2008) as

$$\lambda_{jk} = \frac{\widetilde{H}_{jk}}{\sqrt{\widetilde{H}_{jj}\widetilde{H}_{kk}}}. \quad \textit{(no summation)} \quad (2.57)$$

If the material parameters x_j, x_k are more strongly coupled, λ_{jk} is close to 1 or -1. On the other side, if the absolute value of λ_{jk} is close to zero, this denotes that x_j, x_k are almost decoupled.

2.6. Geometrical shape of classical indenters

In indentation measurements, the most frequently used indenters are divided into two types, namely, the indenters with a revolution surface and the pyramid indenters. The first type includes spherical and conical indenters, whereas the second includes three-sided Berkovich and four-sided Vickers – see their geometries in Fig. 2. 11. Besides, Cube Corner and Knoop

indenters (Zhang and Sakai, 2004; Giannakopoulos, 2006) are also frequently used indenters in experiments.

In practice, many aspects should be considered while choosing an indenter for an indentation measurement, especially in thin film or small volume materials testing, because they require an ultra-low load indentation (Pharr, 1998; Lee et al., 2005; Kizler and Schmauder, 2007). The material of the indenter and the geometry of the indenter tip shape should also be considered. Normally, some researchers assume that the indenter made of diamond is rigid in their theoretical analysis (Smith et al., 2002; Huang and Pelegri, 2007; Yan et al., 2007), because diamond has extreme high hardness and elastic modulus (about 1141 *GPa*). Moreover, the information which one wishes to obtain from the indentation experiment mainly decides the choice of the indenter. For example, the representative strain of the specimen depends solely on the effective apex angle of the Vickers and Berkovich indenters. The greater the desired strain is, the sharper the used angle must be. Therefore, for measuring very thin film coatings, high plastic strain and thus sharp indenters are required.

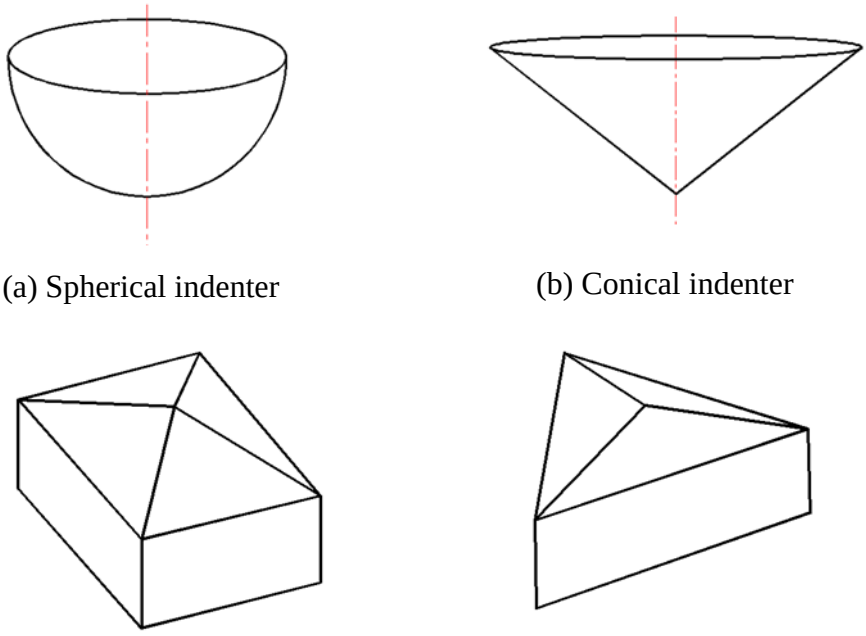

(a) Spherical indenter (b) Conical indenter

(c) Vickers (d) Berkovich

Fig. 2. 11. The tip shapes of four classical indenters.

On the other hand, spherical indenters provide smooth transitions from elastic to elastic-plastic response. They are increasingly used for measuring soft materials and for replicating contact damage for in-service conditions. Currently, radii of the spherical indenters < 1 μm are available.

2.6.1. The similarities and differences in Berkovich, Vickers, conical and spherical indenters

In the identification of hardness and Young's modulus for a given material, the projected contact area, which is a function of penetration depth, has to be calculated. If all the indenters are assumed to have a perfectly designed geometrical shape, according to the geometrical relation, when the penetration depth reaches h, the projected contact areas for these classical indenters are shown in Fig. 2. 12 (Fischer-Cripps, 2002), respectively.

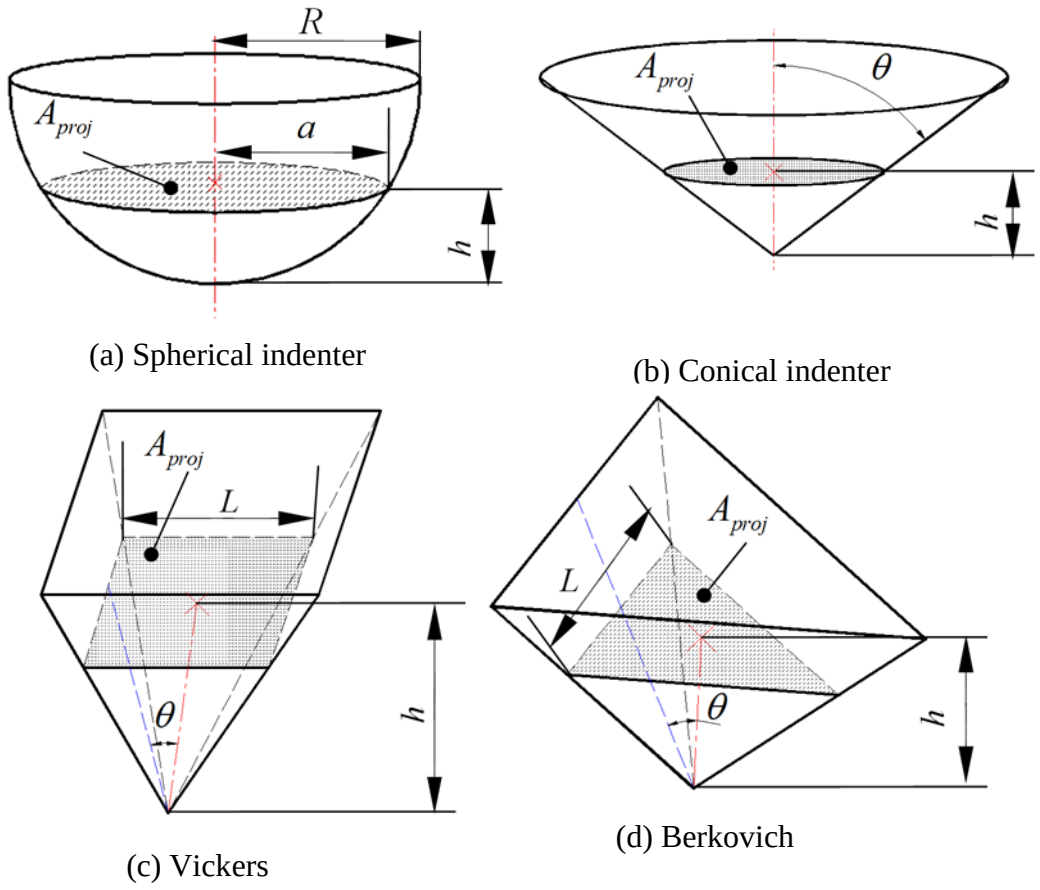

Fig. 2. 12. The geometries of the classical indenters (Fischer-Cripps, 2002).

The projected contact area produced by a spherical indenter is calculated as

$$A_{proj} = \pi a^2 = \pi h(2R - h), \tag{2.58}$$

where a is the radius of the contact area and R is the radius of the spherical indenter. For a Vickers indenter ($\theta = 68^\circ$) (Fischer-Cripps, 2002), the projected contact area is a square. Therefore, it can be calculated as

$$A_{proj}^{V} = L^2, \tag{2.59}$$

here $L = 2h\tan\theta = 2h\tan 68^\circ$, is the edge length of the projected square. Thus, Eq. (2.59) is approximated to

$$A_{proj}^{V} \approx 24.504h^2. \tag{2.60}$$

For a Berkovich indenter ($\theta = 65.3^\circ$) (Fischer-Cripps, 2002) the projected contact area is an equilateral triangle which can be written as below,

$$A_{proj}^{B} = \frac{\sqrt{3}}{2}L^2. \tag{2.61}$$

According to the geometrical relation, the edge length of the projected triangle is calculated as $L = 2h\cot 30^\circ \tan 65.3^\circ$. Thus, Eq. (2.61) is approximated to

$$A_{proj}^{B} \approx 24.56h^2. \tag{2.62}$$

The projected contact area for a conical indenter can be written as

$$A_{proj}^{C} = \pi h^2 \tan^2\theta. \tag{2.63}$$

In the papers (Mata et al., 2002b; Mata et al., 2002a; Mata and Alcala, 2004; Huang and Pelegri, 2007), the researchers used an equivalent conical indenter instead of Vickers and Berkovich indenters in calculation. In their works, the half apex angle of the conical indenter θ is chosen to impose an identical contact area-depth of penetration relation as that in Vickers and Berkovich pyramidal indenters. Therefore, if an equivalent conical indenter is used instead of Vickers and Berkovich indenters, the relations between them can be written as follows:

For a Vickers indenter:

$$\pi h^2 \tan^2\theta = 24.504h^2. \tag{2.64}$$

Thus, the half apex angel of the equivalent conical indenter should be $\theta \approx 70.2996^\circ$.

For a Berkovich indenter:

$$\pi h^2 \tan^2\theta = 24.56h^2. \tag{2.65}$$

The half apex angel of the equivalent conical indenter is equal to $\theta \approx 70.32^\circ$. We can see that both half apex angles of the equivalent conical indenters are approximated to 70.3°. Therefore, Vickers and Berkovich indenters are generally treated as conical indenters with the approximate half apex angle $\theta = 70.32^\circ$ in indentation measurements. In the next part, I will set $\theta = 70.32^\circ$ and 70.3° respectively and compare the differences between them in those simulation results.

2.6.2. Illustration

For most elasto-plastic materials, their plastic behaviours can be closely approximated by the description of the following power law (Dao et al., 2001; Bucaille et al., 2003). The evolution of yield stress due to hardening, σ_v is assumed to be

$$\sigma_v = \sigma_y^0 \left(1 + \frac{E}{\sigma_y^0} \bar{\varepsilon}_p \right)^n , \tag{2.66}$$

where σ_y^0 is the initial yield stress and n is the strain hardening exponent. In the following numerical simulations, the Poisson's ratio of the material is designated as υ. According to the above assumptions and definitions, four independent parameters (E, υ, σ_y^0, n) are defined to completely characterize the elasto-plastic properties of a testing material. Herein, the material is chosen from the published paper (Mata and Alcala, 2004) and its properties are listed in Table. 2. 1. In addition, the Coulomb friction coefficient is set as μ = 0.15 and maximum penetration depth is defined as $h_{\max}$ =19.348 μm. The investigations are carried out by the finite element code METAFOR, which performs powerfully in computation of the nonlinear materials with large deformations (Ponthot, 2010).

Table. 2. 1. The parameters of the used material (Mata and Alcala, 2004).

Name	Value
Young's modulus	E = 200 *MPa*
Poisson's ratio	υ = 0.3
Initial yield stress	σ_y^0 = 675 *MPa*
Strain hardening exponent	n = 0.19

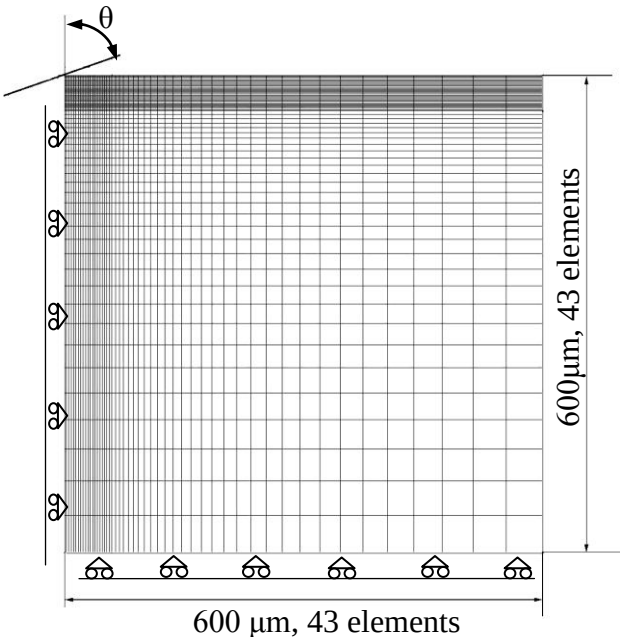

Fig. 2. 13. 2D axisymmetric finite element model with conical indenter.

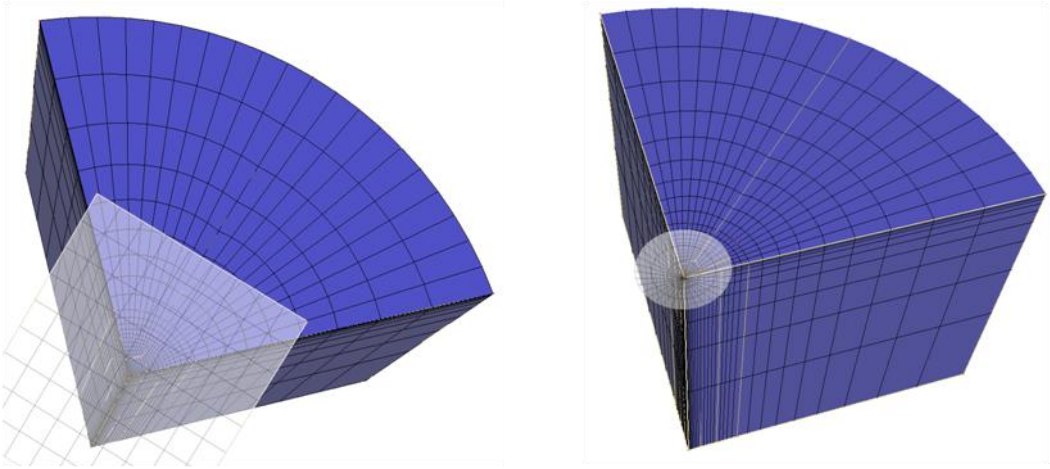

Fig. 2. 14. 3D models used in numerical simulations with Vickers and conical indenters.

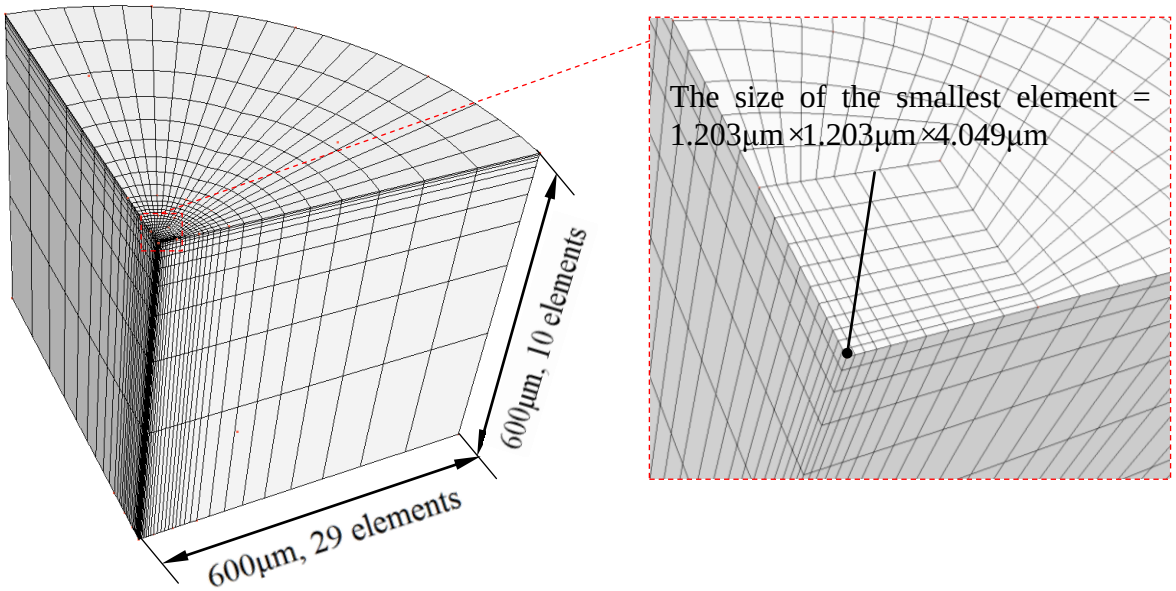

Fig. 2. 15. 3D Finite element model for Vickers indenter. The picture on the right is the detailed figure of the contact area.

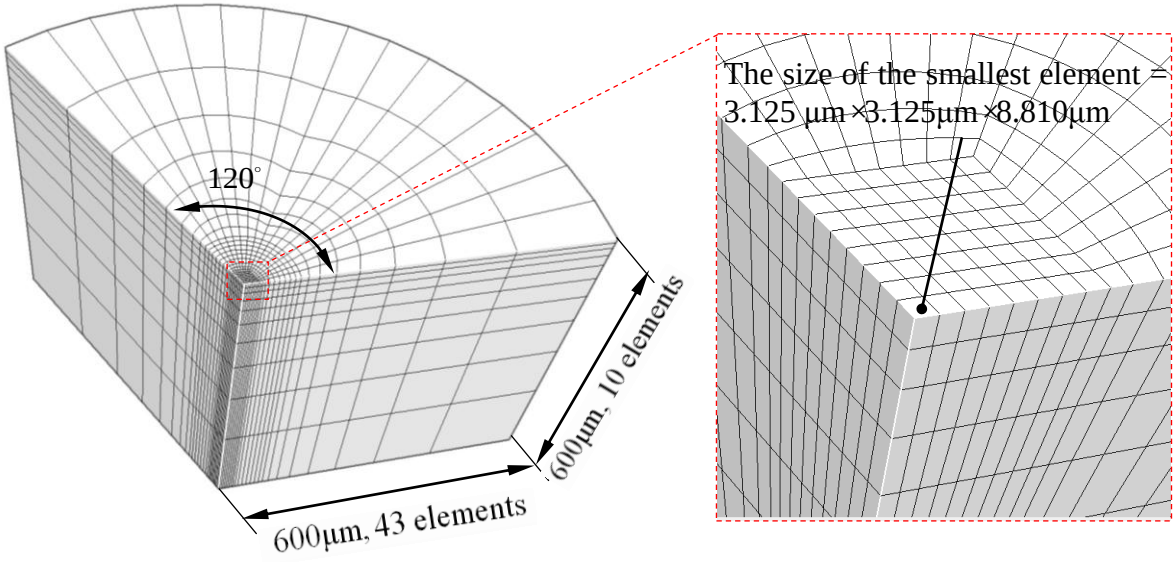

Fig. 2. 16. 3D Finite element model for Berkovich indenter. The picture on the right is the detailed figure of the contact area.

The 2D axisymmetric finite element model which is modelled by 1849 four-noded elements is shown in Fig. 2. 13. The size of the smallest element in the contact area is 2.725 $\mu m \times 2.725$ μm. The displacements of the nodes on the bottom are constrained to zero in the vertical direction and the displacements of the nodes on the left and right sides (axisymmetric axis is also on the left side) are constrained to zero in the radial direction.

One quarter of the 3D models used in numerical simulations with Vickers and conical indenters are shown in Fig. 2. 14. In 3D numerical simulations, both finite element models with Vickers and conical indenters are almost identical. They are modelled by 4800 hexahedral elements with different element densities. Finer elements are used in the neighbourhood of the indenter – see the details in Fig. 2. 15. In the contact area, the size of the smallest element is 1.203 $\mu m \times 1.203$ $\mu m \times 4.049$ μm. For the Berkovich indenter, one third of the 3D model is shown in Fig. 2. 16. The 3D finite element models were discretized by 3360 hexahedral elements with different element densities where finer elements are also used in the neighbourhood of the indenter. In the contact area, the size of the smallest element is 3.125 $\mu m \times 3.125$ $\mu m \times 8.810$ μm. For every model, the displacements of the nodes on the bottom are constrained to zero in the vertical direction and the displacements of the nodes on the side faces are constrained to zero in the radial direction.

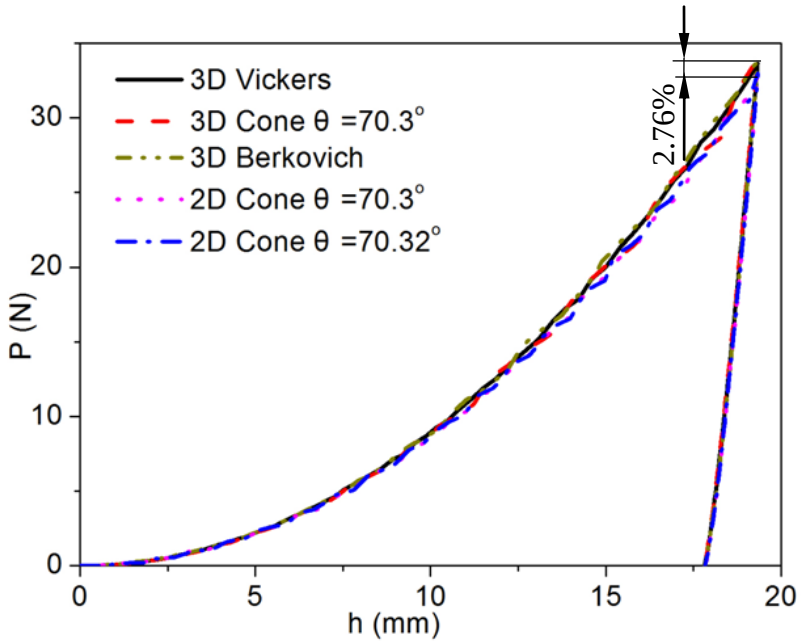

Fig. 2. 17. Comparison of the simulation results.

The corresponding simulation results are shown in Fig. 2. 17. From those $P-h$ curves, it can be seen that there is no large difference in the simulation results obtained using Vickers, Berkovich

and conical indenters. The largest difference in maximum loads is only 2.76%, which means that, we can use the conical indenter with $\theta = 70.3^{\circ}$ instead of Vickers and Berkovich in the indentation measurement and the calculated hardness without having a big error. Indeed, according to the function of hardness,

$$H = \left. \frac{P}{A_{proj}} \right|_{P=P_{\max}}, \tag{2.67}$$

when the penetration depth h reaches $h_{\max}$, the projected contact areas A_{proj} are the same for Vickers, Berkovich and conical indenters. At the same time, the maximum loads $P_{\max}$ are nearly the same (see Fig. 2. 17). Thus, from Eq. (2.67), the calculated hardness H should be approximately the same too.

CHAPTER 3
COMPARISON OF SIMULATION DATA WITH EXPERIMENTAL DATA

Overview

This chapter introduces the sources of dispersion which in numerical models affect the precision of the indentation results including: the boundary conditions, the indentation size effect (ISE), the deformations around the indenter, and the contact friction. Subsequently, the simulations and the experimental results are compared in order to verify the reliability of the numerical model which has been used. Finally, several examples are given to contribute to a deeper understanding of the effects of the contact friction and the tip rounding of imperfect indenters in indentation testing.

Contents

3.1. Indentation results and dispersion sources

In conventional indentation measurements the area of contact between the indenter and the specimen at maximum load is usually calculated from the diameter or the size of the residual impression once the load has been removed. The size of the residual impression is usually considered as identical to the contact area at full load, although the depth of penetration may of course be significantly reduced by the specimen's elastic property. The direct imaging of the residual impression, which is made in the submicron regime, cannot be directly achieved during indentation measurement because the indenter tip itself shields that region from direct access by measurement devices. Therefore, the load and depth of the penetration are usually directly measured during the loading and the unloading cycles. These measurements are then used to determine the projected contact area in order to evaluate the hardness and the elastic modulus. In practice, various errors are associated with this procedure. For example, one of them is that the zero point of the penetration depth should be calculated from the free surface of a specimen. However, the question of how to correctly identify the free surface from the measurement of load-displacement is a crucial task. Specially, the effect of the incorrect zero point of the penetration depth on the hardness will become very severe in shallow indentations (Chen and Ke, 2004; Lee et al., 2005). Another serious error arises from the environmental changes during the measurement and the non-ideal shape of the indenter. The most serious of these errors emerge as offsets to the depth measurements (Fischer-Cripps, 2002).

In addition to the issues mentioned above, there are many dispersion effects that affect the validity of the experimental indentation results. The most serious are the indentation size effect, the phenomenon of piling-up and sinking-in, and the frictional contact between the indenter and the specimen. Besides, in numerical simulations the effect of the boundary conditions should not be neglected. The sensitivity of the indentation test to these phenomena and others is a subject of ongoing research. In this chapter some of the most commonly encountered sources of dispersion and the methods of accounting for them will be reviewed.

3.1.1. Indentation size effect (ISE)

Micro-indentation and nano-indentation hardness experiments are widely used to measure the plastic flow resistance of small volume of materials, such as thin films. It has been repeatedly shown that the indentation hardness of crystalline materials display a strong size effect with conical and pyramidal indenters (Nix and Gao, 1998; Swadener et al., 2002b; Abu Al-Rub and Voyiadjis, 2004; Gao, 2006; Huang et al., 2006; Qu et al., 2006; Haj-Ali et al., 2008). Indeed, early in the 1950s (Tabor, 1951) hardness measurements had been recognized as size dependent. The hardness increase with decreasing indentation depth (or indenter size) has been observed in

numerous indentation studies. Several decades later (Nix and Gao, 1998; Huang et al., 2006) established the relation of the indentation hardness versus the indentation depth to develop a further study and obtain a good agreement with the pioneering works of (Tabor, 1951). This measured indentation hardness of metallic materials typically increases by a factor of two or three as the indentation depth decreases down to the micrometres (Suresh et al., 1999; Xue et al., 2002; Gouldstone et al., 2007). The ISE has been extensively studied in literature and research in this field has continuously increased over the last decades. This has been partly motivated by the development of advanced nano-instruments and the large-scale application of thin films in electronic components, and partly by the availability of new methods of probing mechanical properties in very small volumes. A better understanding of the strength properties of solids at nanometre scales has become increasingly important. This is why the interest in the ISE has been renewed. The studies were stimulated by the rapid development of new high-resolution research techniques.

The existence of the ISE in different materials was confirmed through the use of highly accurate depth-sensing micro- and nano-instruments and scanning probe techniques that fulfil the requirements of the similarity of the indentation shapes and the surface topography (Carpinteri and Puzzi, 2006). Since the discovery of the ISE, several different mechanisms have been suggested for explaining the ISE. The ISE was related to the surface effect including the effects of surface roughness and adhesion, the strain gradient effects, the structural non-uniformity of the deformed volume, the change in the contribution of the elastic and the plastic deformation (Fischer-Cripps, 2002; Carpinteri and Puzzi, 2006). The variety of the proposed mechanisms emphasizes the rather complicated nature of the ISE.

Recent studies (Fischer-Cripps, 2002; Carpinteri and Puzzi, 2006; Qu et al., 2006) have shown a large increase in hardness for the indentation depths which are at the micro- and nanoscales. The ISE is significant at this scale. Thus, most of the systematic investigations of the ISE were performed using a low load micro-hardness testing technique. Various authors (Fischer-Cripps, 2002; Abu Al-Rub and Voyiadjis, 2004; Carpinteri and Puzzi, 2006) proposed that the ISE results from an increase in strain gradients inherent to small localized zones, which lead to geometrically necessary dislocations that cause additional hardening. Inspired by the aforementioned ISE problems, many gradient enhanced theories which are dependent on the material mechanical properties are proposed to address these problems through the incorporation of intrinsic length-scale measures in the constitutive equations. For example, (Gao, 2006) developed an expanding cavity model (ECM) which is based on a strain gradient plasticity solution to determine the indentation hardness of elastic strain-hardening plastic materials for the investigation of the ISE. Other researchers (Carpinteri and Puzzi, 2006) proposed an original interpretation of the indentation size effect in both single crystal and polycrystalline metals

which are based on the experimental evidence of the formation of fractal cellular dislocation patterns during the later stage of the plastic deformation.

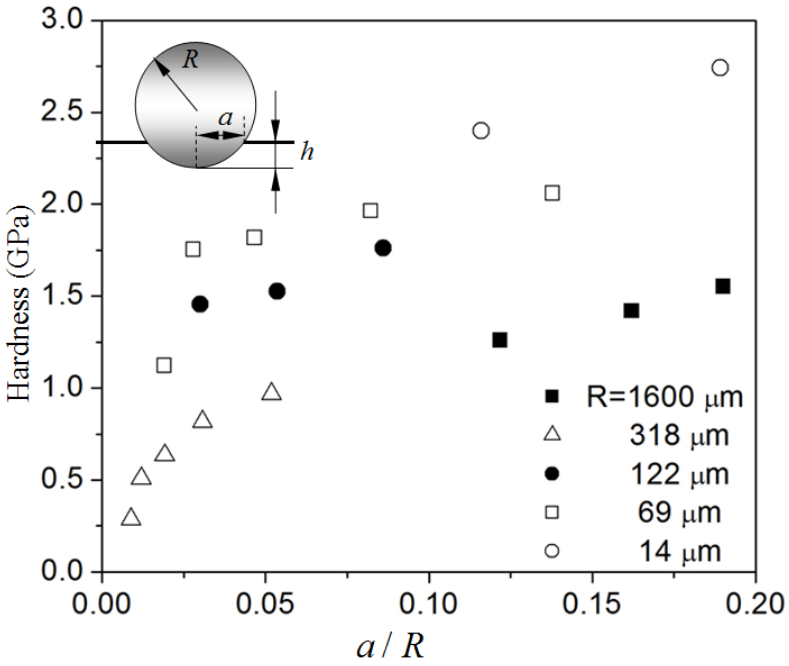

Fig. 3. 1. The indentation hardness of iridium versus the radius ratio a/R. Spherical indenters with different radii ($R=14\ \mu m$, ○; $R=69\ \mu m$, ●; $R=122\ \mu m$, □; $R=318\ \mu m$, ■; $R=1600\ \mu m$, Δ), where a is the contact radius and R is the indenter radius (Qu et al., 2006).

Those continuum-based full-field analyses (Swadener et al., 2002b; Carpinteri and Puzzi, 2006; Huang et al., 2006; Manika and Maniks, 2006; Qu et al., 2006), shed new light on the understanding of this size effect. (Swadener et al., 2002b; Qu et al., 2006) studied the indentation size effect using spherical indenters for which the indentation hardness depends not only on the indentation depth (or equivalently on the contact radius) but also on the indenter radius. (Qu et al., 2006) used five spherical indenter tips to measure the indentation size effect with various radii, namely, a diamond tip with a 14 μm radius, three sapphire tips with 69, 122 and 318 μm radii, and a 1600 μm radius steel ball. As shown in Fig. 3. 1, the indentation hardness H increases with an increase of ratio a/R which means that when the penetration depth is larger, the value of the indentation hardness tends to be larger too. In this figure, a is the contact radius and R is the indenter radius. At the same time, H increases with a decrease of the indenter radius R. However, the opposite phenomenon exists in indentation tests with the Vickers indenter. In order to ascertain the role of structural factors in the ISE, (Manika and Maniks, 2006) studied the dependence of hardness on the indentation depth (less than 300 μm) for single crystals, polycrystals and amorphous solids by using the indentation technology with

Vickers indenter. The decrease in hardness with the increase of the indentation depth for all the investigated crystals was observed in their work. Through their studies a better understanding of the nature of the ISE is achieved. They have found that the ISE occurs in various materials with different type of bonding, namely, metallic, ionic, and covalent.

3.1.2. Piling-up and sinking-in

An important feature of indentation experiments is that the material around the contact area tends to be deformed upwards or downwards with respect to the indented surface plane, see Fig. 3. 2(a). This behaviour results in the piling-up or the sinking-in of the material at the contact boundary. Such surface deformation modes influence the hardness measurements as the true contact area between the indenter and the specimen increases when the piling-up predominates and decreases when the sinking-in occurs.

A systematic investigation of the development of the surface deformation in metals and ceramics around Vickers and spherical indenters was conducted by (Alcalá et al., 2000). They studied the amount of the piling-up or the sinking-in in correlation with the strain hardening exponent of the analysed materials. The results showed that, as the strain hardening exponent increases, the sinking-in of the material around the contact boundary is favoured. Besides, related studies (Wang et al., 2004; Balint et al., 2006; Pelletier, 2006; Yan et al., 2007) showed that the piling-up or sinking-in strongly depends on the plastic work-hardening of the indented material and temperature. The occurrence of such piling-up or sinking-in patterns is usually interpreted in terms of the strain-hardening behaviour of the indented material. According to the investigation (Taljat and Pharr, 2004), the piling-up or sinking-in is also significantly affected by the contact friction.

Furthermore, according to the study of (Liu et al., 2005), the surface around the indenter tends to pile up when the indented specimen is heavily pre-strained with only little reserves for further work-hardening or has generally a low strain-hardening potential. On the other hand, when the sample is fully annealed and has a high strain-hardening potential, the surface around the indenter tends to sink in. In practice, people (Lee et al., 2005; Hernot et al., 2006; Huang et al., 2006; Gerday, 2009) usually say that the piling-up frequently occurs in soft materials whereas the sinking-in occurs in hard materials. In fact, this is not very accurate, because the degree of the piling-up or the sinking-in actually depends upon the ratio E/σ_y^0 and the strain-hardening exponent of the investigated material (Bucaille et al., 2003; Taljat and Pharr, 2004). For the non-strain-hardening materials with a large value of E/σ_y^0, the plastic zone has a hemispherical shape which complies well with the surface well outside the radius of the circle of contact. The piling-up in these materials is to be expected since most of the plastic deformation occurs in the area near the indenter. On the other hand, for materials with a low value of E/σ_y^0 (e.g., some

glasses and ceramics), the plastic zone is typically contained within the boundary of the circle of contact and the elastic deformations that accommodate the volume of the indentation are spread at a greater distance from the indenter. The sinking-in is more likely to occur in this case (Fischer-Cripps, 2002; Taljat and Pharr, 2004).

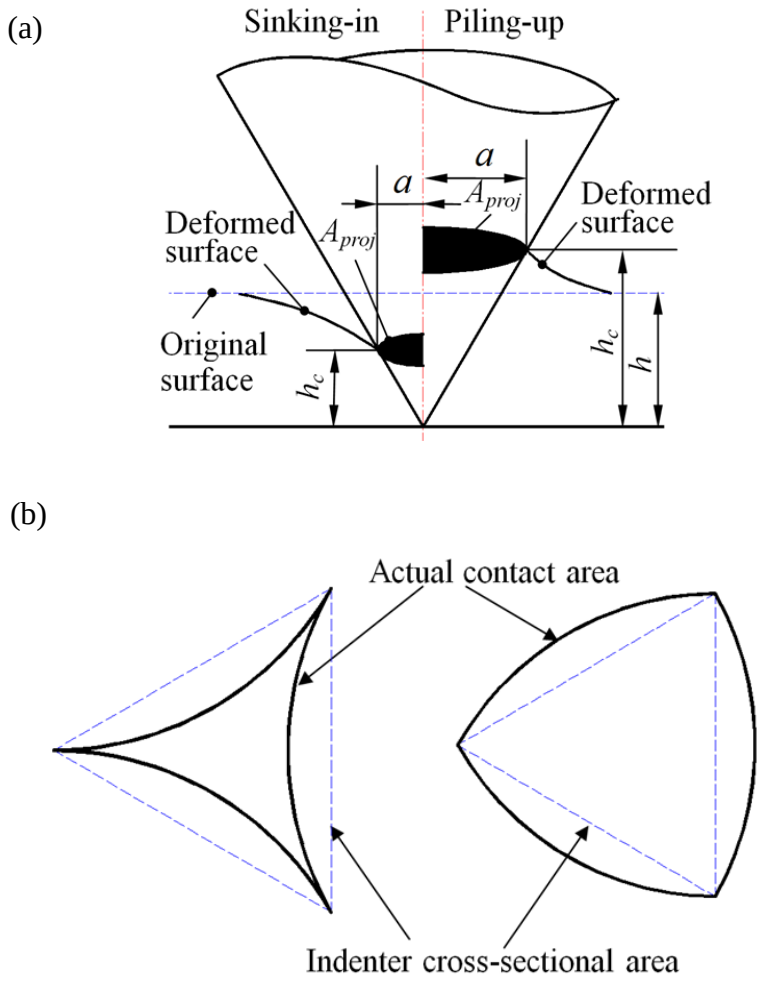

Fig. 3. 2. The effects of the sinking-in (left) and the piling-up (right) on the actual contact area for the same penetration depth. (a) Cross-sectional view (Bucaille et al., 2002); (b) Plan view (Fischer-Cripps, 2002).

Good knowledge of the deformation zone around an imprint is of considerable importance for indentation measurements because the shape of vertical displacement zone determines the actual contact area between the indenter and the specimen. In Fig. 3. 2(b), we can see that the sinking-in patterns reduce the contact area whereas the piling-up patterns increase it. Finite element analyses in which the piling-up and the sinking-in occur also have demonstrated that the true

contact area can be significantly greater or smaller than that evaluated without considering the effect of the piling-up and the sinking-in (Fischer-Cripps, 2002). According to the investigation of (Alcalá et al., 2000), errors of up to 30% can be introduced in the computation of the contact area if the development of the piling-up and the sinking-in is not taken into account. Worse still, (Fischer-Cripps, 2002) argues that the errors of up to 60% can be obtained due to the effect of the piling-up or the sinking-in on the contact area. Moreover, it goes without saying that when the piling-up or the sinking-in are taken into account in micro-indentation and nano-indentation hardness tests, they can cause significant errors when extracting the hardness values from the experimental data (Smith et al., 2002; Wang and Rokhlin, 2005; Balint et al., 2006; Kese and Li, 2006). The piling-up is also significant and it should be corrected in the indentation measurement of thin metal films in order to obtain reliable hardness and Young's modulus data (Balint et al., 2006).

3.1.3. Contact friction

Indentation testing is quite a complex contact problem. The friction between the indenter and the specimen is very important. Friction may cause errors in the determination of the contact area. Thanks to the developments in computer hardware, the use of the finite element method (FEM) has already become an important tool in the achievement of a deeper understanding of indentation measurements even for thin coating materials (Tuck et al., 2001; Fang et al., 2006; Fischer-Cripps et al., 2006; Schwarzer et al., 2006). However, for the sake of simplicity, many studies about indentation do not take into account the friction between the interface of the indenter and the specimen. More recently, the FEM has been extensively employed to study the stress fields in frictionless contact problems as well as to predict the hardness and the development of surface deformation effects in indentation experiments. These analyses suggest that the friction may have an insignificant effect in indentation (Suresh and Giannakopoulos, 1998; Kucharski and Mroz, 2001; Lee et al., 2005) (In their investigations with spherical indenters, Kucharski and Mroz set the ratio $h_{\max} / R$ as 0.0064 and 0.12 respectively. Lee defines that $h_{\max} / R$ is below 0.0325). Nevertheless, in an indentation measurement with different kinds of indenters (spherical, conical or Vickers indenters etc.), the influence of friction in the contact area has been set forth (Johnson, 1985; Bhushan and Sundararajan, 1998; Hurtado and Kim, 1999; Bucaille et al., 2003; Bureau et al., 2003; Mata and Alcala, 2004; Huang and Pelegri, 2007). For instance, in 1985, (Johnson, 1985) first studied the influence of friction in indentation using the theory of the slip-line field. Such early investigations already indicated that an increase of up to 20% in hardness occurs for adhesive contacts as compared to frictionless ones. Moreover, according to the research work (Hernot et al., 2006), if the piling-up or the sinking-in are not taken into account in the determination of Young's modulus, the error can reach 20%.

More significantly, the researchers (Mata and Alcala, 2004) showed that if the values of the yield stress and the work-hardening exponent are extracted from the $P-h$ curves regardless of the friction, they may be up to 50% larger than the actual ones.

3.1.4. Boundary conditions

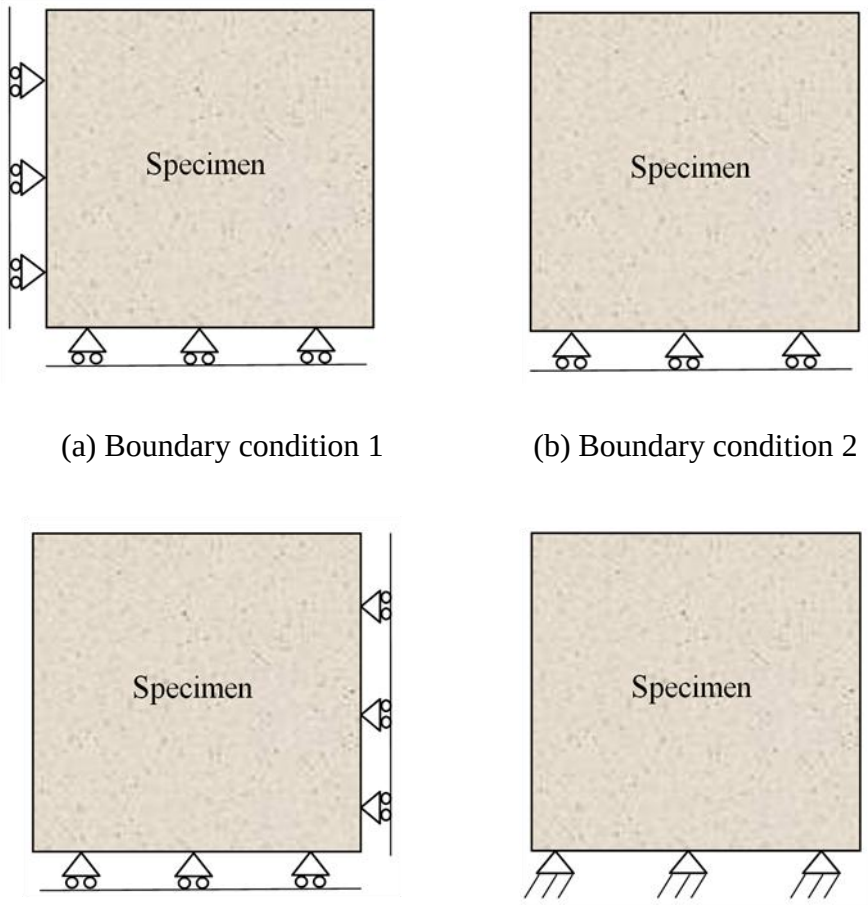

(a) Boundary condition 1 (b) Boundary condition 2

(c) Boundary condition 3 (d) Boundary condition 4

Fig. 3. 3. Boundary conditions.

In numerical simulations of indentation testing, there are several ways to fix the specimen (Komvopoulos and Yang, 2006; Sauer and Li, 2007; Solberg et al., 2007; Yan et al., 2007). Four kinds of boundary conditions are frequently used in FE simulations. Fig. 3. 3 shows the 2D axisymmetric models (axisymmetric axis is on the left side): (a) The displacements of the nodes on the bottom are constrained in the vertical direction and the displacements of the nodes on the

axis of symmetry are constrained in the horizontal direction (Komvopoulos and Yang, 2006; Sauer and Li, 2007); (b) Only the displacements of the nodes on the bottom are constrained in the vertical direction (Hernot et al., 2006); (c) The displacements of the nodes on the bottom are constrained in the vertical direction. Besides, the displacements of the nodes on the right side are constrained in the horizontal direction (Solberg et al., 2007); (d) The displacements of the nodes on the bottom are constrained in the horizontal and the vertical direction (Yan et al., 2007).

A spherical indenter with the radius $R = 2.5\,mm$ is used to study the effects of boundary conditions on indentation responses. All the studies are carried out using the finite element code METAFOR (Ponthot, 2010). The chosen material is similar to the one used in the work (Kucharski and Mroz, 2001). The properties of the specimen are listed in Table. 3. 1.

Table. 3. 1. Used material parameters (Kucharski and Mroz, 2001).

Name	Value
Young's modulus	E = 74.5 *GPa*
Poisson's ratio	$\upsilon = 0.3$
Plastic hardening law	$\sigma_v = 295 + 920\left(\bar{\varepsilon}_p\right)^{0.7}$ *MPa*

The maximum penetration depth is set as $h_{\max} = 0.3\,mm$. In order to check the influence of the size of the specimen, different sizes (*Lx*, *Ly*) have been considered. The sizes of the specimens are defined with the ratio $Ly/h_{\max}$ = 6.67, 13.33, 26.67, 40, 66.67, respectively. The schematic of the specimen sizes are shown in Fig. 3. 4. *Lx* and *Ly* are the radii and heights of the specimens. According to the aforementioned ratio of $Ly/h_{\max}$, *Lx* and *Ly* vary in the range of 2-20 *mm*. In order to eliminate the effect of the number of elements, the densities of elements are imposed to be identical in the same area. For example, in Fig. 3. 4, we assume that the specimen 1 with *Lx*=*Ly*=2 *mm* and the specimen 2 with *Lx*=*Ly*=4 *mm* in the common square 2 *mm* ×2 *mm* have exactly the same mesh. Similarly, the specimen 3 with *Lx*=*Ly*=8 *mm* in the common squares 4 *mm* ×4 *mm* and 2 *mm* ×2 *mm* has the same meshes as the specimens 2 and 1. In the same way, the specimens 4 and 5 with *Lx*=*Ly*=12 *mm* and 20 *mm*, respectively, obey the same rule. See Fig. 3. 4, the finite element model is modelled by four-noded quadrilateral elements. On the bottom and right edges, the numbers of the elements are set as *nx* = *ny* = 20. On the top edge, the numbers of the elements are set as *nx1*= *nx2*= *nx3*= *nx4*= *nx5*=20.

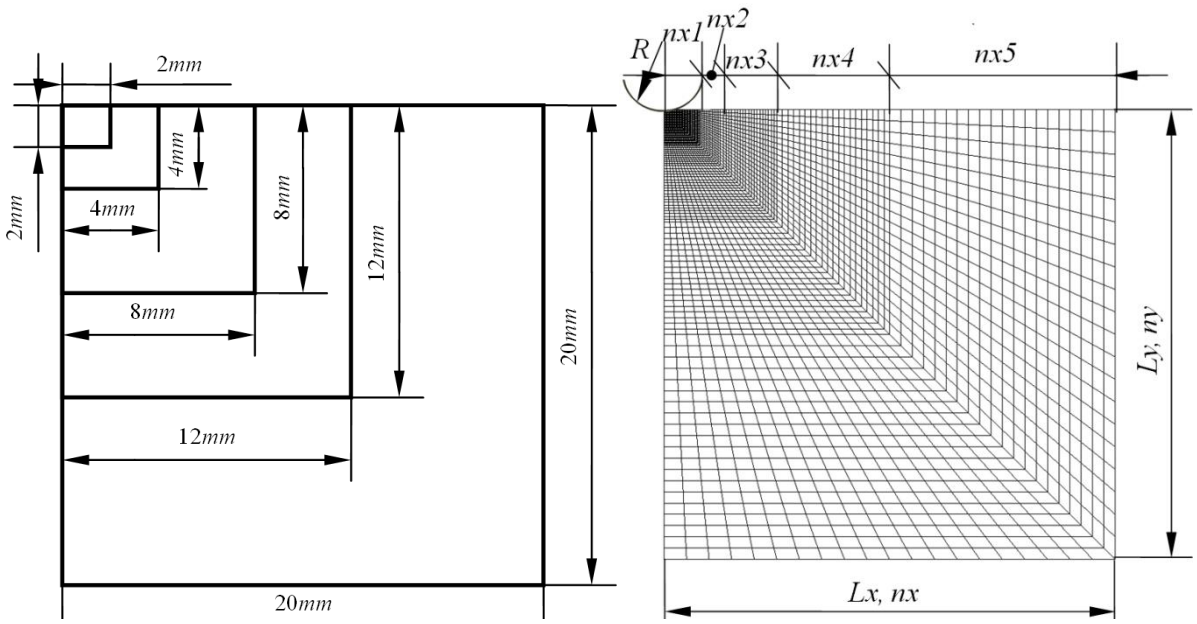

Fig. 3. 4. Schematic drawing of the sizes of the specimens and the finite element model.

The load versus the indentation depth curves for all the boundary conditions are shown in Fig. 3. 5. One can clearly notice that the boundary conditions can significantly affect the simulation results when the volume size is too small (the maximum difference between P_{max} is 23%). For example, when Ly/h_{max} = 13.33, the maximum load is obviously lower than the other cases for the boundary conditions 1, 2 and 4 because the unfixed right edge lets the material move easily in the horizontal direction while the indenter is penetrating into the specimen. However, for the boundary condition 3, the maximum load decreases with an increase of Ly/h_{max} . When we check the deformation map, the stresses and the strain on the bottom edge and the right edge are very large in the specimen with a smaller size, which means that, when the ratio of Ly/h_{max} is too small, the fixed boundaries on the bottom and the right edges resist the deformations on the horizontal and the vertical direction when the indenter is penetrating into the specimen.

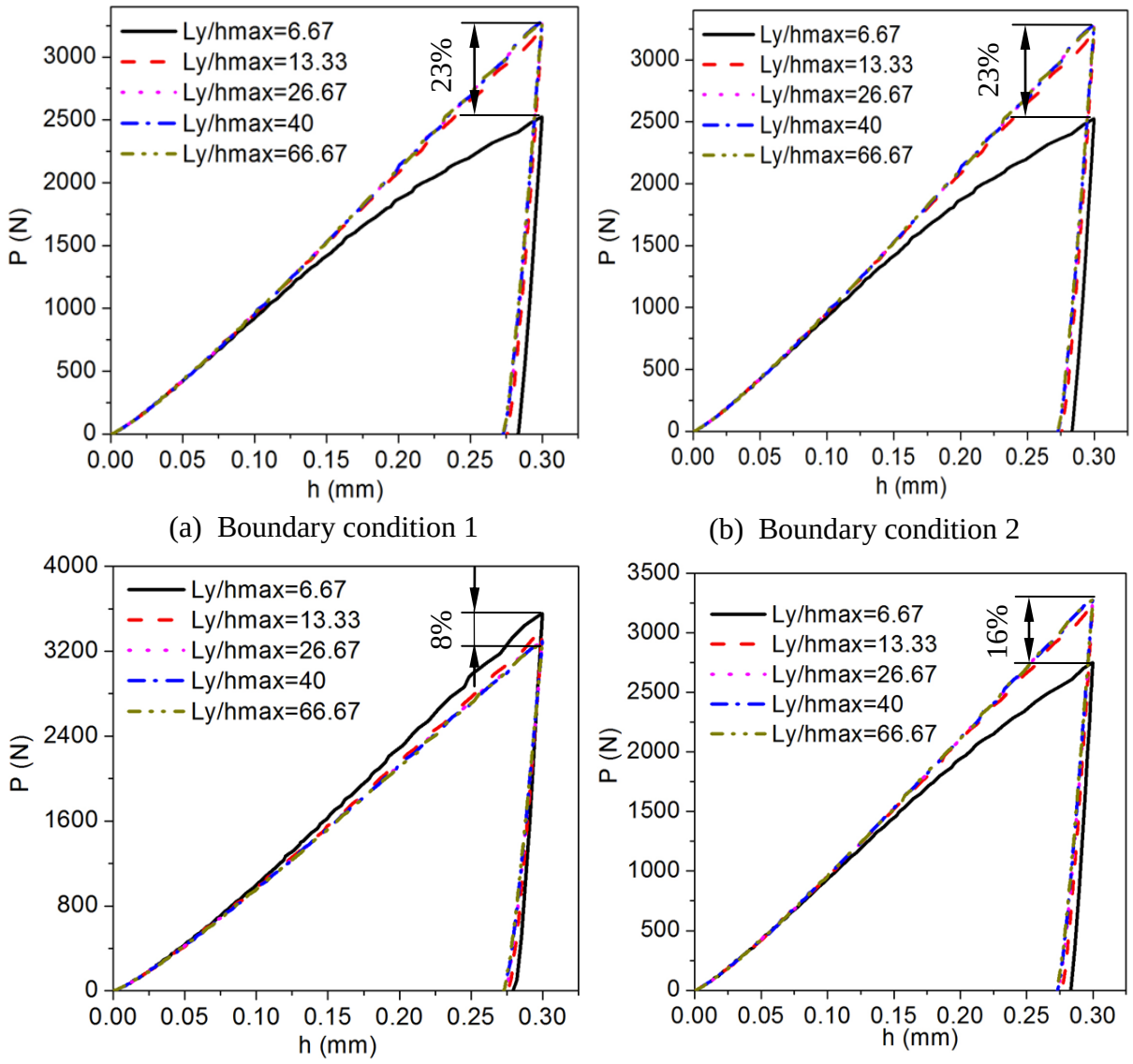

Fig. 3. 5. Effects of the boundary conditions on the indentation responses.

The maximum loads P_{max} with different sizes of volumes for all boundary conditions are shown in Fig. 3. 6. We can see that with an increase of Ly/h_{max}, the P_{max} increases for the boundary conditions 1, 2 and 4, and decreases for the boundary condition 3. When the volume size Ly/h_{max} is superior to 40, the effects of the boundaries are insignificant and the value of P_{max} tends to a horizontal line for very boundary condition. Moreover, Fig. 3. 6 shows that the P_{max} are always identical for the boundary conditions 1 and 2. This is due to the fact that in METAFOR code, for the 2D axisymmetric models, if the axisymmetric axis is on the left side, the displacements of the nodes on the left side will be automatically constrained in the

horizontal direction. Therefore, for every model in the present investigation, the displacements of the nodes on the left sides are in fact constrained in the horizontal direction. In the following parts, the boundary condition 1 is always used in numerical investigations,

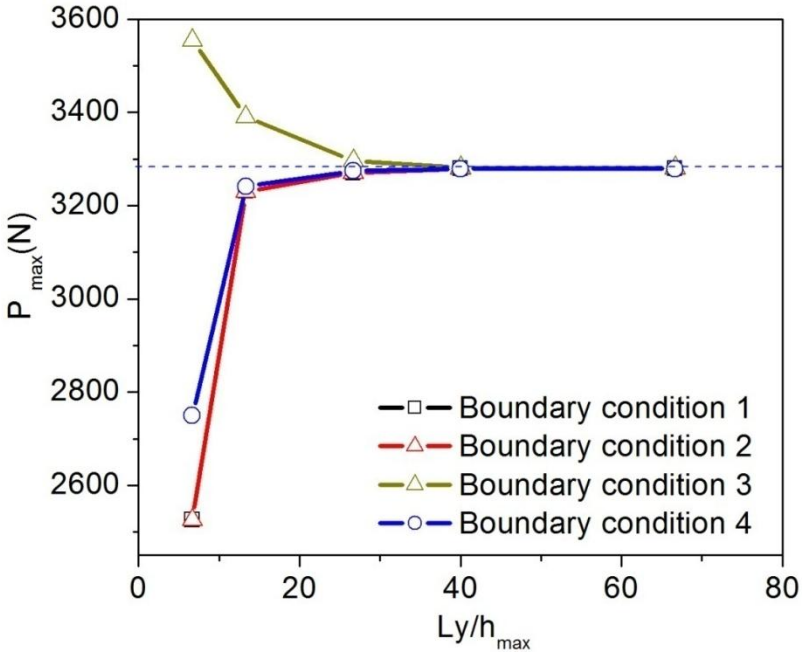

Fig. 3. 6. Maximum loads obtained on the different volumes of specimens for the different boundary conditions.

3.2. Comparison of the results obtained in the simulations and the experiments

In this section, in order to verify the accuracy of the numerical model, the results obtained in simulations and experiments are compared. Herein, the 2D finite element models and the boundary restrictions which were used are established in METAFOR code (Ponthot, 2010). In Fig. 3. 7, the model is built using quadrilateral elements. A finer mesh is near the contact region and a gradually coarser mesh is further from the contact region. The details of the contact regions with spherical and conical indenters are shown on the right of the figure. R is the radius of the spherical indenter and θ is the half apex angle of the conical indenter.

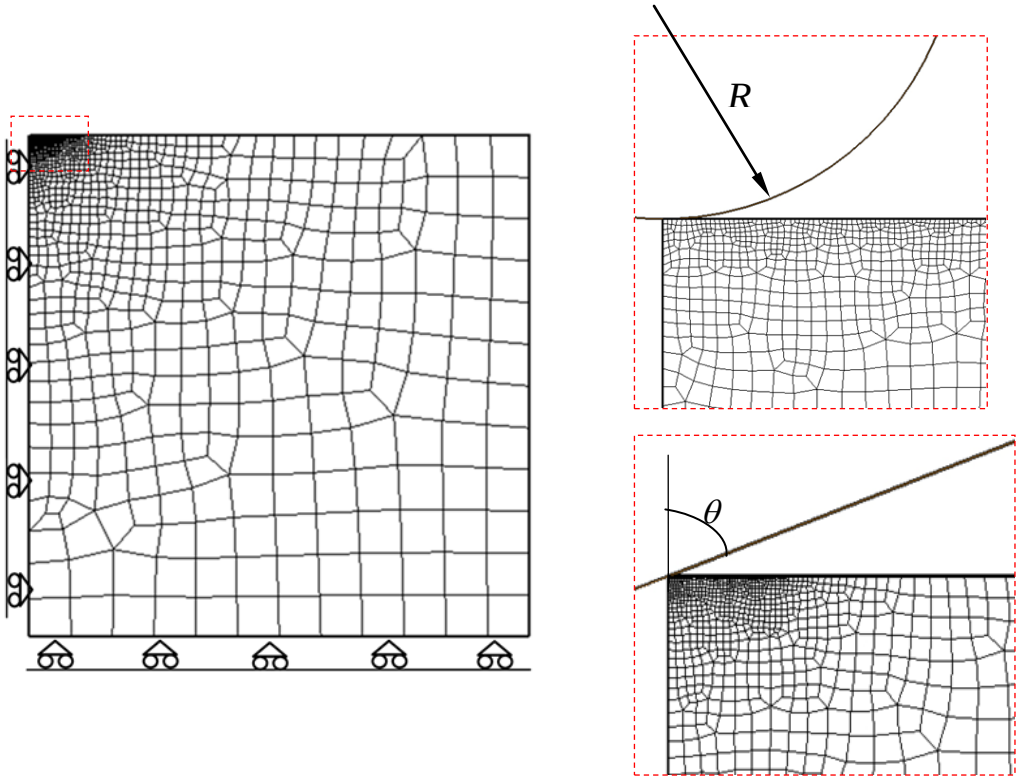

Fig. 3. 7. The 2D axisymmetric finite element model which was used.

3.2.1. Simulation with spherical indenter

Here, the simulation with a spherical indenter is performed according to the work of (Kucharski and Mroz, 2001). The parameters of the material which was used are listed in Table. 3. 1. The 2D finite element model and the boundary restrictions are like the ones shown in Fig. 3. 7. The model is designed with 648 four-noded quadrilateral elements. At the maximum load, about 30 contacted nodes are in the contact zone to ensure the accuracy of the calculation. The radius of the spherical indenter is set as $R = 1.25\,mm$ and the contact friction is ignored.

The simulation results compared with the data in literature (Kucharski and Mroz, 2001) can be seen in Fig. 3. 8. The maximum penetration force $P_{\max}$ equals to 1430 N in the 2D simulation. Compared to the maximum penetration force 1454 N in the experiment, the difference is lower than 2%. Therefore, it can be said that the simulation results agree well with the data in literature.

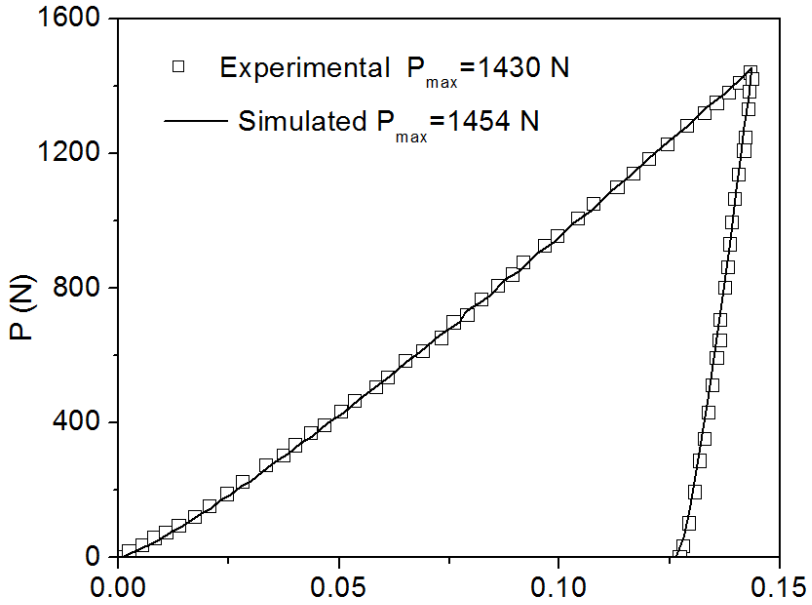

Fig. 3. 8. The comparison of the maximum penetration force with the data in literature (Kucharski and Mroz, 2001), the relative error is 1.7%.

3.2.2. Simulation with conical indenter

Here, the simulation with a conical indenter will be compared to the work (Dao et al., 2001). The material used is 6061-T6511 aluminium the properties of which are described by the material parameters (E, υ, σ_y^0, n)=(66.8 GPa, 0.28, 301 MPa, 0.05). The plastic behaviour is described by the power law, see Eq. (2.66). The contact is modelled as frictionless.

The finite element model and the boundary conditions for the conical simulation are like the one shown in Fig. 3. 7. The half apex angle of the conical indenter that was used is set as $\theta = 70.3^{\circ}$. The 2D axisymmetric model is modelled by 1324 four-noded quadrilateral elements and is like the model used in the spherical simulation.

The simulation result compared with the experimental data (Dao et al., 2001) can be seen in Fig. 3. 9. It is clear that the simulation and the experimental data are almost identical.

From the above comparisons, it can be seen that the results obtained by the numerical tool which was used are reliable.

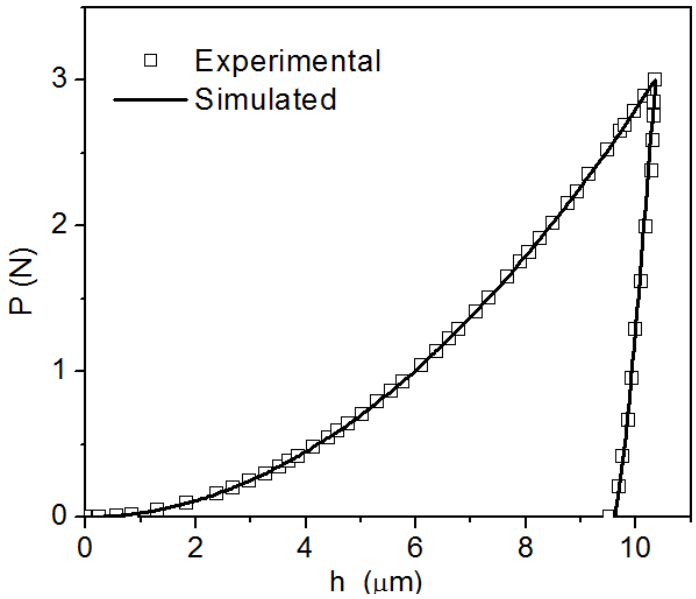

Fig. 3. 9. Experimental versus simulated indentation responses of 6061-T6511 aluminium (Dao et al., 2001).

3.3. Investigations of the effects of the contact friction and the imperfect indenter tips in indentation

3.3.1. Contact friction

Although the features of the frictional contact are nowadays studied by more and more researchers, a theoretical background to evaluate the influence of the friction coefficient on indentation measurements is still difficult to achieve. Here, some numerical studies are carried out in order to contribute to a deeper understanding of the influence of friction in indentation. The comparisons of the calculated hardness and Young's modulus will be shown in the following parts for the frictional and the frictionless cases.

3.3.1.1. Theoretical and computational consideration

If an elasto-plastic material is identified by indentation testing with a sharp indenter, during the loading, the load-displacement curve generally follows the relation described by Kick's Law (Dao et al., 2001),

$$P = Ch^2, \tag{3.1}$$

$$C = H\alpha_m f_g, \tag{3.2}$$

where, C is the loading curvature, h is the penetration depth which is directly measured by the instrumented indentation, H is the hardness of indented material, α_m is a parameter that evaluates the piling-up or sinking-in of the material at the contact boundary, and f_g is a geometrical factor. For the conical indenters, $f_g = \pi \tan^2 \theta$ with the half apex angle of the conical indenter, θ. Therefore, if $\theta = 70.3^\circ$, f_g is equal to 24.504. For the spherical indenters, f_g is close to $2\pi R$, with the radius of the spherical indenter, R (Fischer-Cripps, 2002).

By recording the data of the whole indentation procedure, the indentation hardness H and the Young's modulus E can be calculated as suggested in the work (Oliver and Pharr, 1992), see more details in the section 2.3.

The indenter is often assumed to be rigid (Lee et al., 2005; Luo and Lin, 2007), therefore, $E_i \to \infty$. The Young's modulus can be rewritten as,

$$E = (1-\upsilon^2)E_r = \frac{(1-\upsilon^2)\sqrt{\pi}}{2}\frac{S}{\sqrt{A_{proj}}}. \tag{3.3}$$

Because the hardness is defined as

$$H = \frac{P}{A_{proj}},$$

according to Eqs.(3.1) and (3.2), the above equation can be written as

$$A_{proj} = \frac{P}{H} = \alpha_m f_g h^2. \tag{3.4}$$

Considering the piling-up or the sinking-in, the true projected contact area A_{proj} should be written as

$$A_{proj} = f_g h_c^2, \tag{3.5}$$

where h_c is the contact depth which incorporates the piling-up or the sinking-in as shown in Fig. 2. 5. Eqs. (3.4) and (3.5) indicate that

$$\sqrt{\alpha_m} = h_c / h. \tag{3.6}$$

Therefore, if $\sqrt{\alpha_m} > 1$, the piling-up occurs. On the other hand, $\sqrt{\alpha_m} < 1$ denotes the sinking-in. In order to quantify the deformation of the piling-up or the sinking-in, according to Eq. (3.6), a derived parameter β is introduced to magnify the difference between h_c and h. It is defined as

$$\beta = \frac{h_c - h}{h} = \sqrt{\alpha_m} - 1. \tag{3.7}$$

This equation denotes that, when $\beta > 0$, the piling-up occurs. On the other hand, $\beta < 0$ denotes the sinking-in.

3.3.1.2. Numerical simulations

Three materials, SAF 2507 stainless steel and annealed copper used in (Mata and Alcala, 2004), and aluminium alloy used in (Bucaille et al., 2003), are chosen for illustration. The corresponding material parameters are listed in Table. 3. 2. Young's modulus is represented as E and the initial yield stress is represented as σ_y^0. n is the work-hardening exponent and υ is the Poisson's ratio.

For the elasto-plastic models, the plastic behaviours are approximated by the power law described by Eq. (2.66) (Dao et al., 2001; Bucaille et al., 2003) and von Mises plasticity with J_2 flow theory is assumed.

Table. 3. 2. Materials used in the simulations.

Material	Properties
SAF 2507 stainless steel	$(E, \upsilon, \sigma_y^0, n)$ =(200 GPa , 0.3, 675 MPa , 0.19)
Annealed copper	$(E, \upsilon, \sigma_y^0, n)$ =(110 GPa , 0.32, 20 MPa , 0.52)
Aluminium alloy	$(E, \upsilon, \sigma_y^0, n)$ =(70 GPa , 0.3, 500 MPa , 0.122)

Systematic numerical studies are carried out with a variety of indenter geometries and friction coefficients. All numerical simulations are performed using the finite element code METAFOR (Ponthot, 2010). The 2D axisymmetric finite element models constructed to simulate the indentation responses of elasto-plastic solids are similar to the ones shown in Fig. 3. 7. They are modelled using 1849 four-noded quadrilateral elements. For every indenter, the mesh is designed to ensure that the minimum number of the nodes in the contact region is never less than 35 when the indenters reach the maximum penetration depth.

For the conical indenters, the half apex angle θ is set as 63.14°, 70.3°, 75.79°, 80° and 81.5° in this part and the maximum penetration depth is set as $h_{\max} = 0.01935mm$. The finite element model for the conical indenters is designed with 600 μm height and 600 μm radius.

For the spherical indenters, R is the radius. The height and the radius of the finite element models used equal 8 mm and 1.6 mm, respectively, for $R = 1.25\,mm$ and $R = 0.25\,mm$. The maximum penetration depth is defined as $h_{\max} = 0.15mm$ and $h_{\max} = 0.33mm$ for two spherical indenters respectively.

Measured friction coefficients show that the value of μ between well polished metallic surfaces and diamond normally lies within 0.1 to 0.15 (Mata and Alcala, 2004). In this part, a wide range of μ, which varies from 0.0 to 1.0, are adopted for all the simulations with spherical and conical indenters.

3.3.1.3. Computational results and comparison for conical indenters

The $P-h$ curves obtained for the SAF 2507 stainless steel, annealed copper and aluminium alloy with different friction coefficients are shown in Fig. 3. 10(a) to Fig. 3. 12(a). Although the friction coefficient μ varies from 0.0 to 1.0, the $P-h$ curves obtained for a given half apex angle are nearly identical. The difference between values of $P_{\max}$ in Fig. 3. 10(a) to Fig. 3. 12(a) are all lower than 2.55%. However, this does not mean that there is no impact on the calculated hardness, the Young's modulus, and the yield stress too because they have a direct correlation with the true projected contact area A_{proj}. Given that A_{proj} is a function of h_c and that it is related to the piling-up or the sinking-in, the values of the piling-up or the sinking-in obtained with or without considering the friction may be absolutely different.

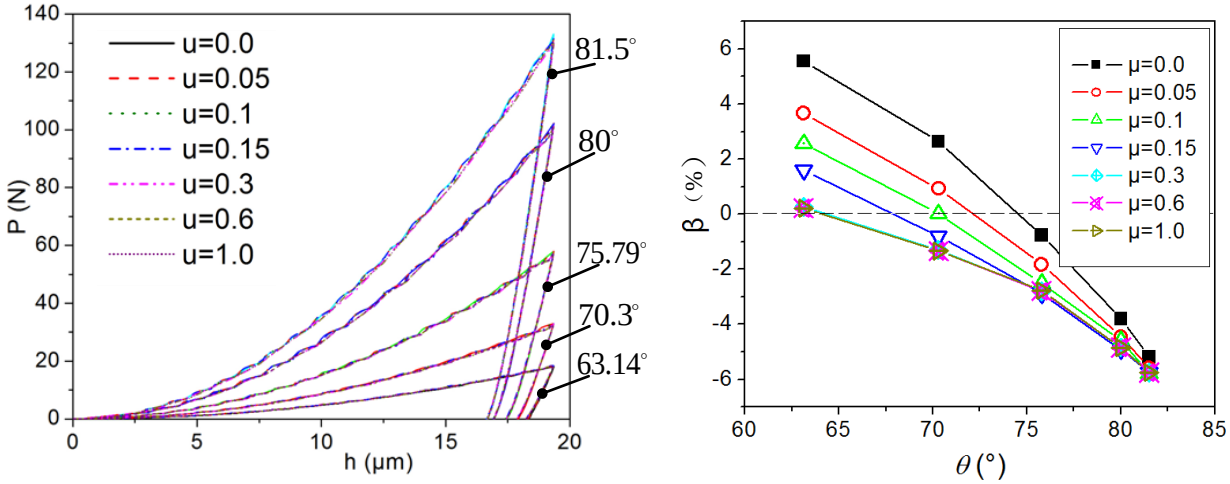

(a) $P-h$ curves for different θ

(b) β versus θ for different friction coefficient μ

Fig. 3. 10. Calculation results as obtained with the conical indenters for SAF 2507.

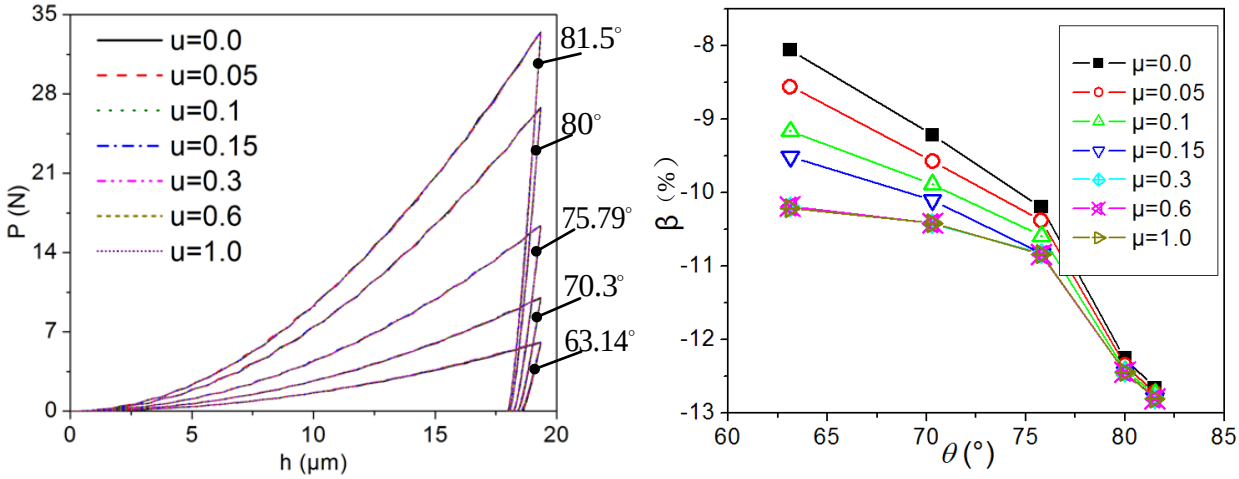

(a) $P-h$ curves for different θ

(b) β versus θ for different friction coefficient μ

Fig. 3. 11. Calculation results as obtained with the conical indenters for annealed copper.

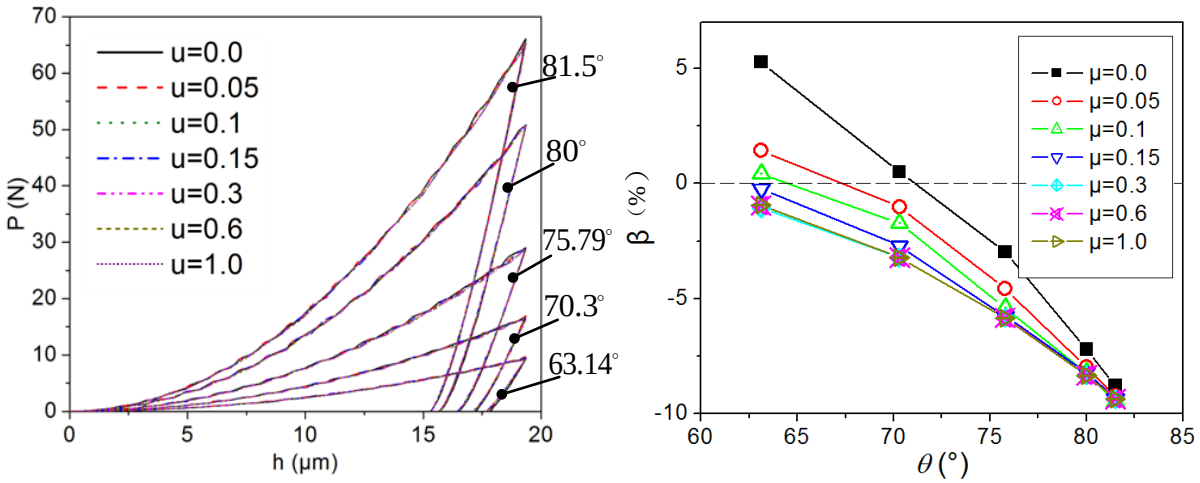

(a) $P-h$ curves for different θ

(b) β versus θ for different friction coefficient μ

Fig. 3. 12. Calculation results as obtained with the conical indenter for aluminium alloy.

Therefore, the parameters β (remind that $\beta>0$ means piling-up while $\beta<0$ means sinking-in) are shown in Fig. 3. 10(b) to Fig. 3. 12(b) for every conical indenter with different friction coefficients μ. For all the materials, the values of β tend to decrease following an increase of μ. The curve for a larger μ is always below the curve for a smaller μ. This means that the fact of adopting a larger μ can effectively restrain the piling-up from growing, especially with a smaller half apex angle. For example, in Fig. 3. 10(b), in the case of $\theta=70.3^{\circ}$, while $\mu<0.1$ the

values of β are above zero, and the deformation of the material around the indenter is piling-up. However, following an increase of μ, β becomes smaller, the piling-up disappears and the sinking-in appears. Besides, in Fig. 3. 10(b), we can see that, with the same value of μ, when the half apex angle θ increases, the amount of the piling-up decreases, and the sinking-in tends to occur. For example, for $\mu = 0$, when $\theta = 63.14^\circ$, it is piling-up, but when $\theta = 81.5^\circ$, it is sinking-in. This means that, in the indentation measurements with a smaller half apex angle, the piling-up will easily occur. On the other hand, when the half apex angle is large enough, the piling-up will be replaced by the sinking-in. The foregoing phenomena also appear in Fig. 3. 11(b) for annealed copper, and Fig. 3. 10 (b) for aluminium alloy. Here, it should be noted that, in Fig. 3. 11(b), the values of β are always below zero, which denotes that only the sinking-in occurs for the annealed copper as it has a larger work-hardening exponent n. This is in good agreement with the results presented in the works (Alcalá et al., 2000; Wang et al., 2004; Pelletier, 2006).

Furthermore, for every material, we can clearly see that in the case of $\theta = 63.14^\circ$, the differences in the deformations of the piling-up or the sinking-in with different μ ($\mu < 0.3$) are obvious and that with an increase of θ, the differences decrease. Concurrently, we can also note that, when $\mu > 0.3$, β remains unchanged following an increase in μ. After the examination of the deformed mesh, we find that the nodes on the interface between the indenter and the specimen remain stuck, which leads to the nearly same values of the piling-up or the sinking-in although the friction coefficients are different. However, this also strongly depends on the half apex angle θ. When θ is larger, even if μ takes a small value, the value of β will remain constant. In Fig. 3. 10(b), in the cases of $\theta \geq 80^\circ$, even if $\mu = 0.05$, these differences are invisible. The nodes on the interfaces prove to have nearly no slip when studying their displacements in the tangent direction. Those findings show that the value of β is less affected by the friction coefficient if the indentation is performed using a conical indenter with a larger half apex angle.

3.3.1.4. Computational results and comparison for spherical indenters

Fig. 3. 13 shows the $P-h$ curves obtained by the spherical indenters with different friction coefficients for the three materials listed in Table. 3. 2. The $P-h$ curves in Fig. 3. 13(a), Fig. 3. 15(a) and Fig. 3. 17(a) are obtained using a bigger spherical indenter ($R = 1.25\,mm$). In Fig. 3. 13(b), Fig. 3. 15(b) and Fig. 3. 17(b), the $P-h$ curves are obtained using a smaller spherical indenter ($R = 0.25\,mm$). It is similar to those obtained by the conical indenters. The $P-h$ curves cannot be distinguished although the friction coefficient μ varies from 0.0 to 1.0. The differences between the maximum and the minimum values of $P_{\max}$ are all lower than 1.4% for all the materials. A larger friction coefficient can effectively constrain the piling-up and leads to

an increase in the amount of the sinking-in. However, when $\mu > 0.3$, the nodes on the interface are sticking and the amount of the sinking-in tends to be constant. Moreover, the curves of β versus μ obtained for the different spherical indenters are almost identical – see Fig. 3. 14, Fig. 3. 16 and Fig. 3. 18. It seems that the curve of β versus μ is independent of the radius of the spherical indenter.

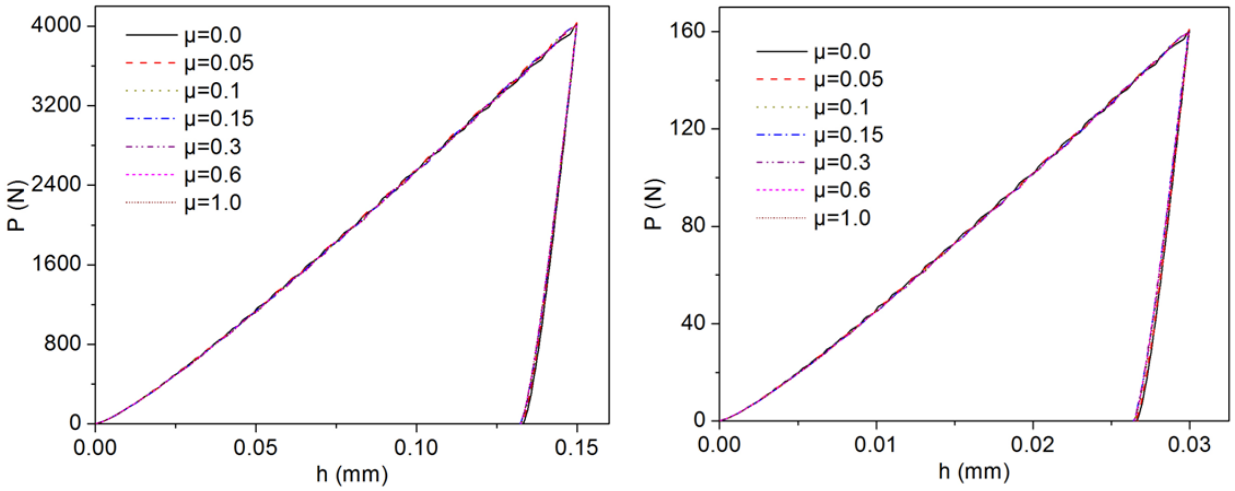

(a) $R = 1.25\,mm$ (b) $R = 0.25\,mm$

Fig. 3. 13. Numerical $P-h$ curves as obtained with the spherical indenters for SAF 2507.

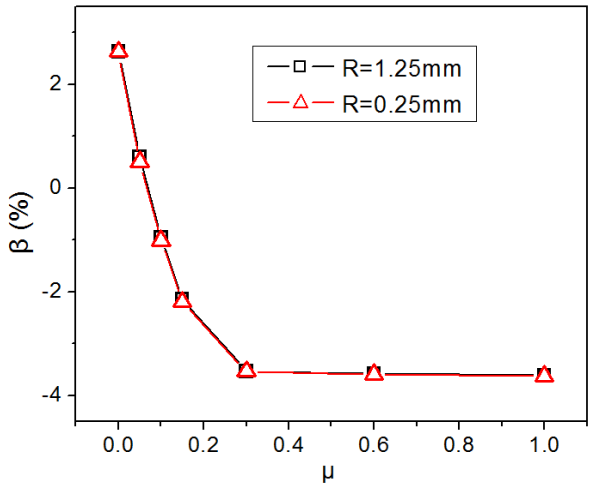

Fig. 3. 14. β versus the friction coefficient μ for SAF 2507.

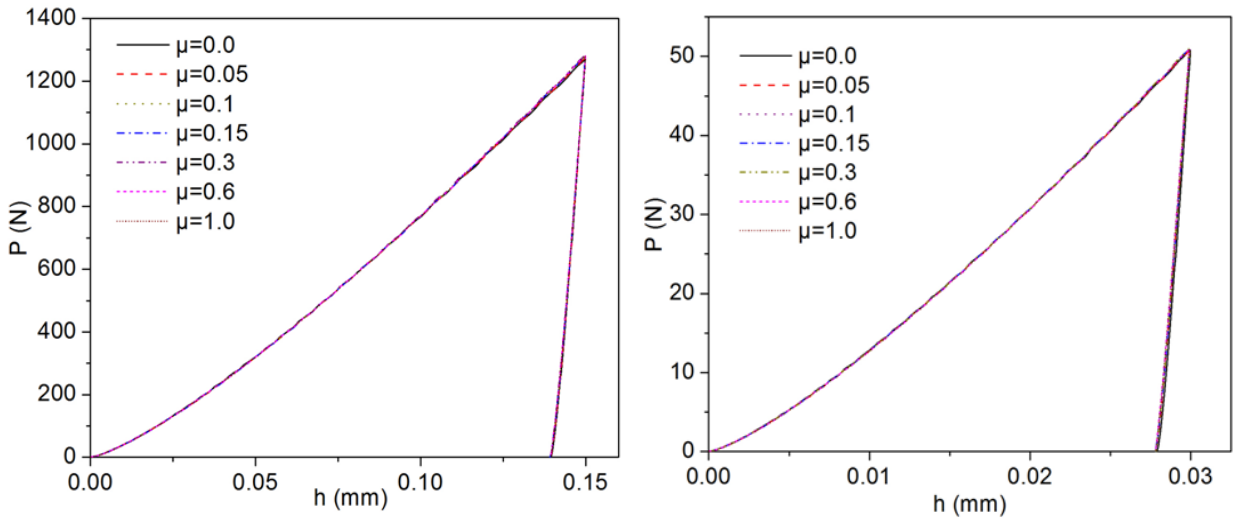

(a) $R = 1.25\,mm$ (b) $R = 0.25\,mm$

Fig. 3. 15. Numerical $P-h$ curves as obtained with the spherical indenters for annealed copper.

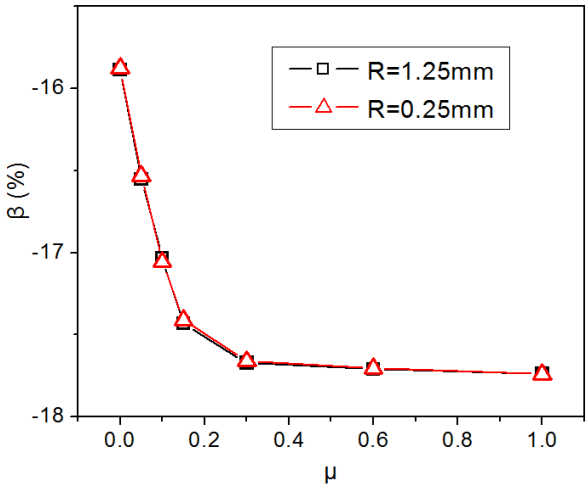

Fig. 3. 16. β versus the friction coefficient μ for annealed copper.

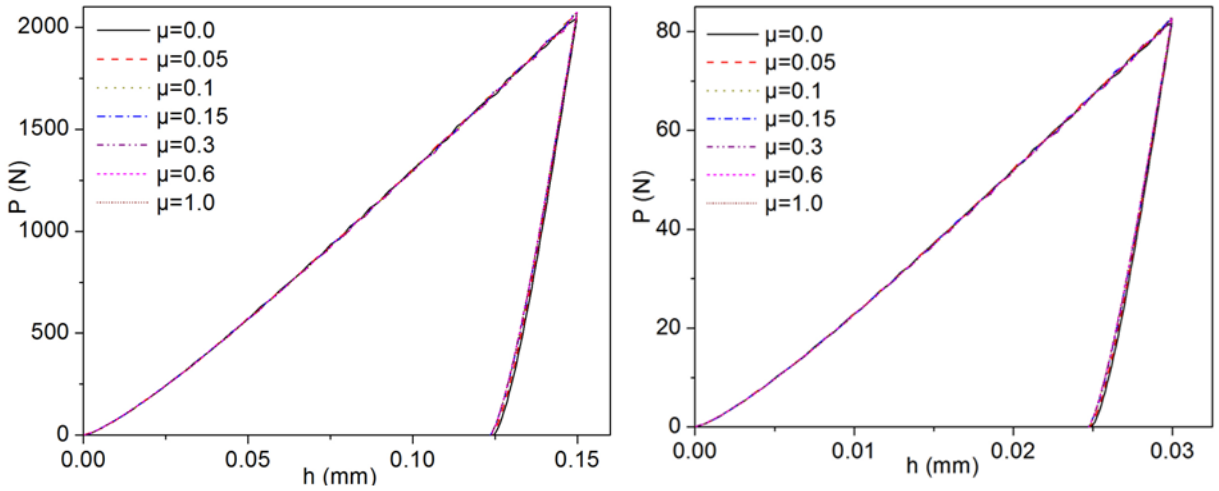

(a) $R = 1.25\,mm$ (b) $R = 0.25\,mm$

Fig. 3. 17. Numerical $P-h$ curves as obtained with the spherical indenters for aluminium alloy.

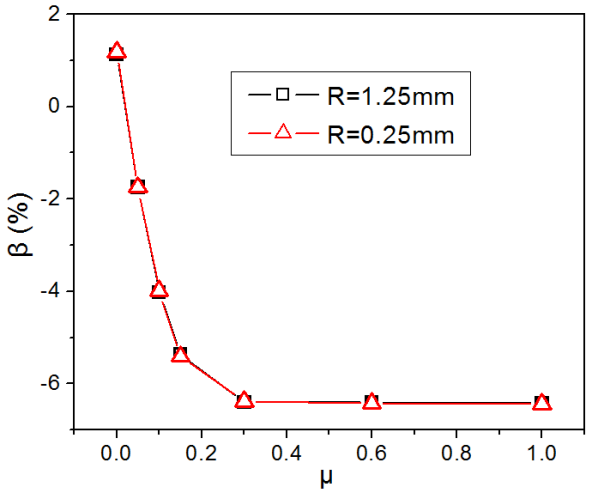

Fig. 3. 18. β versus the friction coefficient μ for aluminium alloy.

3.3.1.5. Discussions

From the foregoing comparisons we can see that the $P-h$ curves obtained either by conical or spherical indenters with different friction coefficients are nearly identical. However, through the parameter β, the influence of friction on the piling-up or the sinking-in is clearly highlighted. In Table. 3. 3 to Table. 3. 5, we illustrate explicitly how this impact influences the calculated hardness and Young's modulus, which are evaluated by the conical indenter with $\theta = 63.14^{\circ}$ and the spherical indenter with $R = 0.25\,mm$. The H and E labelled by "O&P" denote that the contact depth h_c is calculated according to the classical method (Oliver and Pharr, 1992), see

Eq. (2.40). The "FEM" denotes that the contact depth h_c is directly measured in the foregoing FEM simulations taking into account the effect of friction.

One can clearly see that, the friction coefficient also affects the calculated values of the hardness and Young's modulus. They increase with an increase of the friction coefficient. The maximum differences of the hardness and the Young's modulus appear in the simulations for aluminium alloy. The maximum difference of the hardness caused by the friction coefficient reaches 10.5% and 5.9%, for conical ($\theta = 63.14^\circ$) and spherical indenters respectively. Similarly, the maximum error of Young's modulus reaches 11.4% and 8.5% in comparison with the real input Young's modulus (i.e. Young's modulus that has been input in the FEM calculation) for conical ($\theta = 63.14^\circ$) and spherical indenters respectively.

Thus, we can say that from the foregoing analysis results, the errors of the calculated hardness and the Young's modulus caused by the influence of friction are significant and should not be neglected.

Table. 3. 3. SAF 2507 stainless steel ($E = 200\,GPa$).

	Friction coefficient	H (GPa)		E (GPa)			
		O&P	FEM	O&P	Err (%)	FEM	Err (%)
Conical indenter	μ =0	4.3	3.6	230	15.0	210	5.0
	μ =0.05	4.3	3.7	230	15.0	213	6.5
	μ =0.1	4.3	3.8	230	15.0	216	8.0
	μ =0.15	4.3	3.9	230	15.0	218	9.0
	μ =0.3	4.3	4.0	230	15.0	221	10.5
	μ =0.6	4.3	4.0	230	15.0	221	10.5
	μ =1.0	4.3	4.0	230	15.0	221	10.5
Spherical indenter	μ =0	3.8	3.4	218	9.0	206	3.0
	μ =0.05	3.8	3.5	218	9.0	208	4.0
	μ =0.1	3.8	3.6	218	9.0	210	5.0
	μ =0.15	3.8	3.6	218	9.0	212	6.0
	μ =0.3	3.8	3.7	218	9.0	213	6.5
	μ =0.6	3.8	3.7	218	9.0	213	6.5
	μ =1.0	3.8	3.7	218	9.0	213	6.5

Table. 3. 4. Annealed copper ($E = 110\,GPa$).

	Friction coefficient	H (GPa)		E (GPa)			
		O&P	FEM	O&P	Err (%)	FEM	Err (%)
Conical indenter	μ =0	1.4	1.6	108	-1.3	115	4.6
	μ =0.05	1.4	1.6	108	-1.3	116	5.5
	μ =0.1	1.4	1.6	108	-1.3	116	5.5
	μ =0.15	1.4	1.6	108	-1.3	117	6.4
	μ =0.3	1.4	1.6	108	-1.3	118	7.3
	μ =0.6	1.4	1.6	108	-1.3	118	7.3
	μ =1.0	1.4	1.6	108	-1.3	118	7.3
Spherical indenter	μ =0	1.2	1.4	105	-4.3	112	1.8
	μ =0.05	1.2	1.4	105	-4.3	112	1.8
	μ =0.1	1.2	1.4	105	-4.3	112	1.8
	μ =0.15	1.2	1.4	105	-4.3	113	2.7
	μ =0.3	1.2	1.4	105	-4.3	113	2.7
	μ =0.6	1.2	1.4	105	-4.3	113	2.7
	μ =1.0	1.2	1.4	105	-4.3	113	2.7

Table. 3. 5. Aluminium alloy ($E = 70\,GPa$).

	Friction coefficient	H (GPa)		E (GPa)			
		O&P	FEM	O&P	Err (%)	FEM	Err (%)
Conical indenter	μ =0	2.3	1.9	81	16.4	73	4.3
	μ =0.05	2.3	2.0	81	16.4	76	8.6
	μ =0.1	2.3	2.1	81	16.4	77	10.0
	μ =0.15	2.3	2.1	81	16.4	77	10.0
	μ =0.3	2.3	2.1	81	16.4	78	11.4
	μ =0.6	2.3	2.1	81	16.4	78	11.4
	μ =1.0	2.3	2.1	81	16.4	78	11.4
Spherical indenter	μ =0	2.1	1.84	78	11.3	73	4.3
	μ =0.05	2.1	1.89	78	11.3	74	5.7
	μ =0.1	2.1	1.93	78	11.3	75	7.1
	μ =0.15	2.1	1.96	78	11.3	76	8.6
	μ =0.3	2.1	1.98	78	11.3	76	8.6
	μ =0.6	2.1	1.98	78	11.3	76	8.6
	μ =1.0	2.1	1.98	78	11.3	76	8.6

3.3.1.6. Conclusions

The influences of friction in indentation with conical and spherical indenters are studied in this part. It has been found that, for some elasto-plastic materials, the $P-h$ curves obtained either by spherical or conical indenters with different friction coefficients in the range of engineering metals are nearly identical. Then, the parameter β was introduced to evaluate the piling-up or the sinking-in. The Fig. 3. 10(b) to Fig. 3. 12(b) clearly show that the friction between the indenter and the specimen can significantly affect the contact area and the amount of the piling-up or the sinking-in in the simulation with the conical indenter. Especially, when the half apex angle is smaller, the influence of the friction is obvious. It can effectively oppose the slip of nodes on the interface between the indenter and the specimen, which leads to a decrease in the amount of the piling-up or an increase of the sinking-in. However, when the half apex angle is large enough, e.g. $\theta \geq 80^{\circ}$, the influence of the friction becomes a minor factor in indentation even with a small friction coefficient because the nodes on the interface between the indenter and the specimen are stuck. In indentations with spherical indenters, the amount of the piling-up decreases or the sinking-in increases with an increase of the friction coefficient while $\mu < 0.3$. However, the friction is independent of the radius of spherical indenters. The curves of β versus μ obtained by two different spherical indenters with varying friction coefficients do not have obvious differences.

Because the friction can significantly affect the contact area and the piling-up or the sinking-in, the values of the material parameters, the hardness, the Young's modulus and the yield stress, which are related to the projected contact area A_{proj}, should be significantly different too. For all the materials, the maximum difference of the hardness with and without considering the friction can reach 10% and the error of Young's modulus can reach 11% in comparison with the input Young's modulus. These results do not agree with those proposed by the researchers who claim that the instrumented indentation experiments are not significantly affected by the friction (Dao et al., 2001; Kucharski and Mroz, 2001; Lee et al., 2005).

3.3.2. Imperfect indenter tips

According to published papers, it is well known that all the geometries of the indenter tips are usually assumed perfectly spherical for conical and pyramid indenters. The radius of an unused Berkovich indenter tip varies from 50 *nm* to 70 *nm* (Pelletier, 2006; Schwarzer et al., 2006; Zhong and Zhu, 2008). Vickers indenters usually have a larger rounded tip because it is four-sided pyramid and four sides are technologically speaking difficult to intersect to one point. Therefore, the radius of a new indenter tip is normally considered as 50 *nm*-100 *nm*. However, the indenter tip rapidly wears out. As a consequence, for old indenters (Tuck et al., 2001;

Fischer-Cripps, 2002), the radius of an indenter tip is considered as 200 nm-400 nm. In this part, it is assumed that the radius of the indenter tip varies from 0 nm to 500 nm. For this definition, if the radius of an indenter tip is equivalent to 0 nm, the indenter has a perfect sharp tip.

Herein, the materials are similar to the ones used in the last section, and their properties are listed in Table. 3. 2. However, the friction coefficient μ is fixed as 0.1.

The 2D axisymmetric finite element model constructed and used to simulate the indentation responses of the elasto-plastic solids in the METAFOR code is shown in Fig. 3. 19. The model is defined with 46 μm height and 46 μm radius and it is established by 15577 four-noded quadrilateral elements, see details in Fig. 3. 19(b). The symmetric axis is on the left side of the model, and the displacements of the nodes on this boundary are constrained in the horizontal direction. At the same time, the displacements of the nodes on the bottom side are constrained in the vertical direction. The half apex angle of the conical indenter is defined as $\theta = 70.3^{\circ}$ and the tip radius of this imperfect conical indenter is assumed as ρ, which varies from 50 nm to 500 nm. The contact problem is treated by the penalty method and the load is applied by controlling the displacement of the indenter. The maximum penetration depth is set as $h_{\max} = 700nm$. While the indenter reaches the maximum penetration depth, more than 350 nodes are in the contact region to guarantee the accuracy of the simulation data.

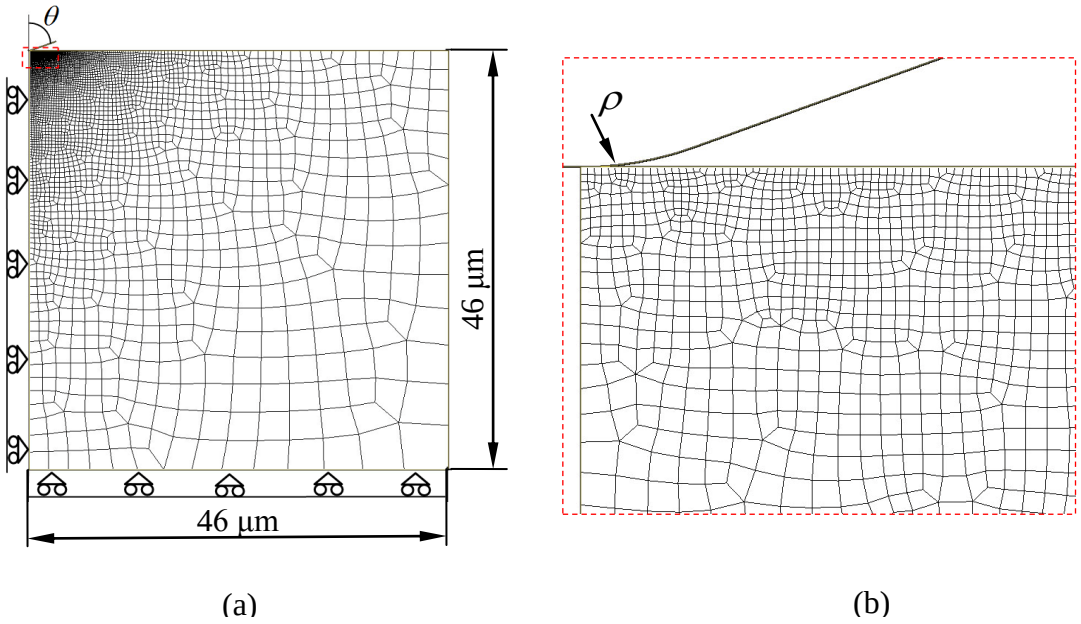

Fig. 3. 19. Finite element model used in 2D numerical simulation. (a) Overall mesh; (b) Details of the contact region.

3.3.2.1. Discussions

In many published references (Dao et al., 2001; Luo and Lin, 2007), most of the time the indenters are assumed to exhibit the perfect sharp shapes. Thus, the projected contact area can be calculated as $A_{proj} = 24.5h_c^2$. The calculated hardness for all the materials are shown in Fig. 3. 20. It is clear that the hardness increases significantly with an increase of the tip radius. The hardness obtained by an indenter with a large tip radius is not reliable. Therefore, there is a good reason to believe that in hardness calculations, the effect of the indenter tip should no longer be neglected. A failure to account correctly for the indenter tip can lead to incorrect interpretation of the experimental data. The determination of the exact shape of the indenter is critical in indentation measurements.

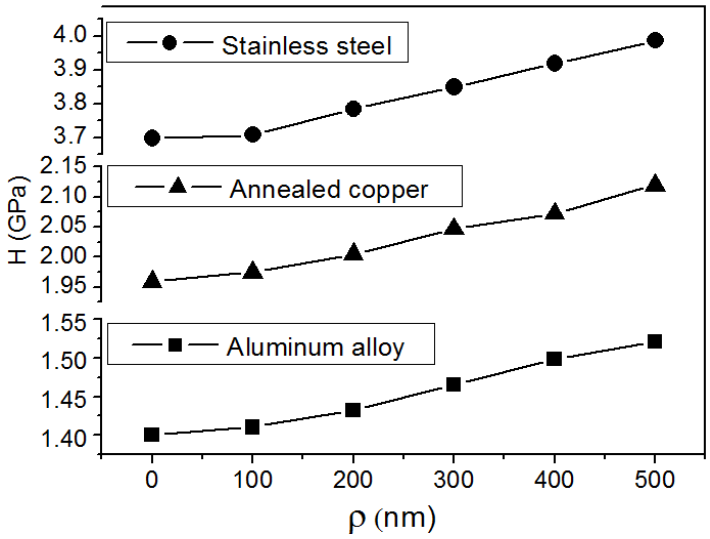

Fig. 3. 20. The hardness estimated by imperfect indenters.

Recently, more and more researchers have begun to notice the influence of the indenter tip and a number of methods or procedures have been proposed to determine the geometry of an actual indenter tip. Indeed, (Oliver and Pharr, 1992) have put forward an improved equation which is widely used in current indentation instruments to account for the influence of the indenter tip. Besides, other researchers also proposed some enhanced methods to evaluate the tip influence on the calculation of the hardness. For example, (Thurn and Cook, 2002) presented the profile of the indenter tip as a harmonic average of a conical tip and a spherical tip. They advised that the projected contact area should be written as

$$A_{T\&C} = \pi(\frac{h_c}{\cot\theta} + 2\rho\cot\theta)^2, \tag{3.8}$$

where ρ is the radius of the indenter tip and θ is the half apex angle of conical indenter.

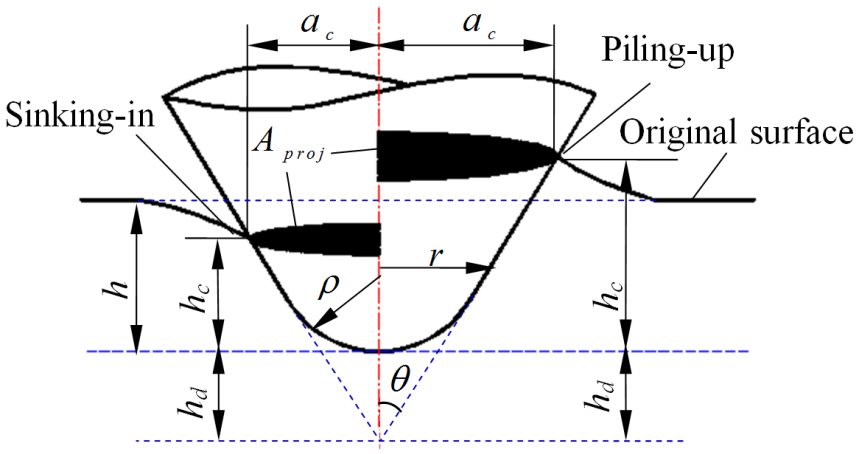

Fig. 3. 21. Schematic of the imperfect conical indentation profiles with the sinking-in and the piling-up (Bucaille et al., 2002).

Herein, we propose another modified projected area function for an imperfect indenter. It is derived from the geometrical relations of the imperfect indenter tip, see Fig. 3. 21. The contact radius a_c can be written as

$$a_c = (h_c + h_d)\tan\theta, \tag{3.9}$$

where h_d is the deviation of the penetration depth for the imperfect indenter. It is expressed by

$$h_d = \rho(\sin^{-1}\theta - 1). \tag{3.10}$$

Therefore, a modified projected contact area function for the imperfect indenter is described as bellow with Eqs. (3.9) and (3.10),

$$A_{Modified} = \pi a_c^2 = \pi(h_c \tan\theta + \frac{1-\sin\theta}{\cos\theta}\rho)^2. \tag{3.11}$$

Then, the hardness is calculated according to this modified method as:

$$H_{Modified} = \frac{P}{A_{Modified}}. \tag{3.12}$$

Moreover, some researchers advised that the hardness should be calculated directly from the energy dissipated during indentation. This method, used for the calculation of the hardness, is the so-called "work-of-indentation approach" which is performed in the investigations (Venkatesh et al., 2000; Tuck et al., 2001; Xue et al., 2002; Zhao et al., 2006a). The advantage of the work-of-indentation approach is that when we calculate the hardness of the material, the imperfection of the indenter geometry is not specially considered. In the work-of-indentation

approach, the hardness is shown in terms of the maximum applied load divided by the projected contact area, and it is equivalent to the plastic work divided by the plastically deformed volume,

$$H_{Energy} = \frac{P}{A_{proj}} = \frac{W_P}{V_P}, \tag{3.13}$$

where V_P is the volume of the plastic deformation. Here, in order to simplify the problem, given that a sharp conical indenter is used, V_P can be calculated as

$$V_P = \frac{1}{3} A_{proj} h_f = \frac{1}{3} \pi h_c^2 h_f \tan^2 \theta . \tag{3.14}$$

W_P is the plastic work which can be written as

$$W_P = W_T - W_E , \tag{3.15}$$

where W_T is the loading work. The schematic illustration of a $P-h$ curve registered in an indentation measurement can be seen in Fig. 3. 22. W_T can be calculated as

$$W_T = \int_0^{h_{\max}} P dh . \tag{3.16}$$

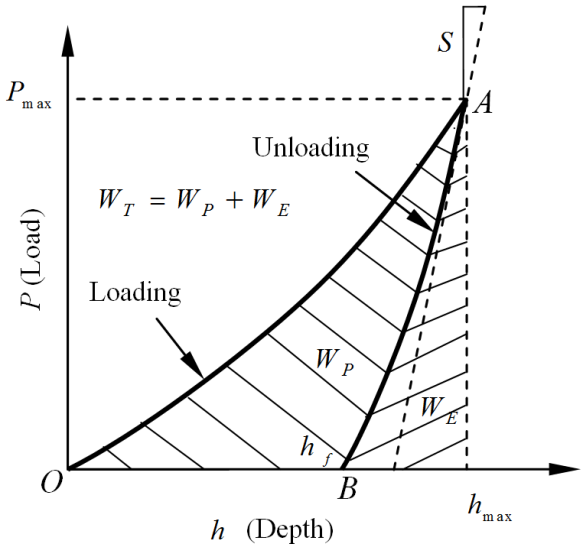

Fig. 3. 22. Typical indentation load-depth ($P-h$) curve for elasto-plastic material (Tuck et al., 2001).

It is defined as the work done by the indenter during the loading cycle, namely, it is equal the area under the curve OA. Similarly, the area underneath the unloading curve AB is the total unloading work,

$$W_E = -\int_{h_{\max}}^{h_f} P dh . \tag{3.17}$$

W_E also represents the reversible elastic work in indentation.

According to the above, we know that the differences between the foregoing three methods are mainly located in the calculation of the projected contact area except for the method of energy. The differences of A_{proj} obtained by the method of Oliver and Pharr, Thurn and Cook, and the modified method in comparison with that obtained by the sharp indenters are shown in Fig. 3. 23. The differences are defined as bellow,

$$\delta A = \frac{\left| A_{Tip} - A_{Sharp} \right|}{A_{Sharp}}, \tag{3.18}$$

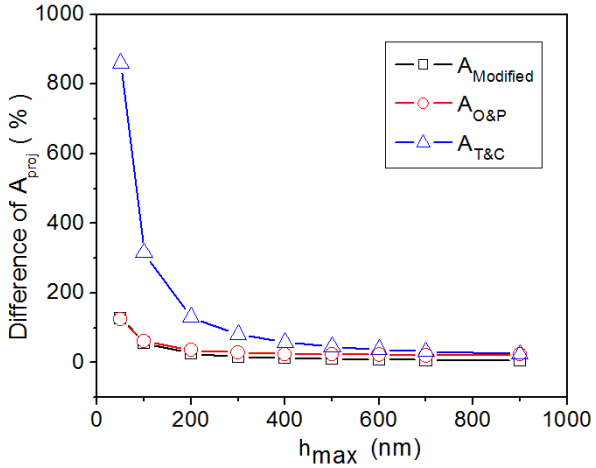

(a) Stainless steel;

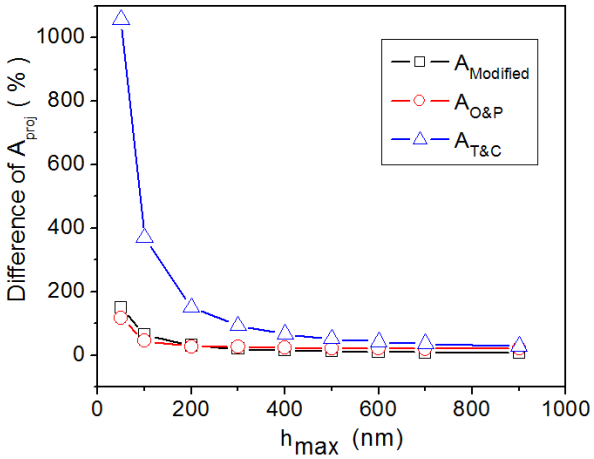

(b) Annealed copper;

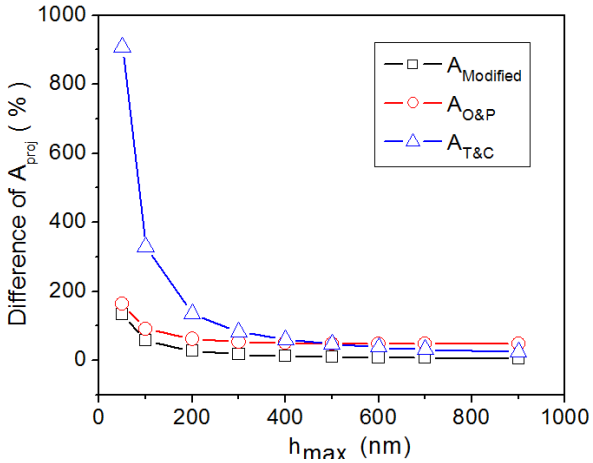

(c) Aluminium alloy.

Fig. 3. 23. The differences of A_{proj} determined by different methods at different penetration depths.

where A_{Tip} represents the projected contact area obtained by the method of Oliver and Pharr, Thurn and Cook, and the modified method which accounts for the influence of the indenter tip when it is replaced by $A_{O\&P}$, $A_{T\&C}$ and $A_{Modified}$ respectively. In this section, the tip radius of the indenter is fixed at $\rho = 400\,nm$ and the maximum penetration depth varies from $50\,nm$ to $900\,nm$. It is clear that in a shallow indentation, the influence of the indenter tip is obviously noticeable. For example, in Fig. 3. 23, while $h_{\max} = 50nm$, the differences of A_{proj} obtained by the methods which account for the influence of the indenter tip are larger than 100% in comparison with the ones that neglect the influence of the indenter tip. Particularly, for the projected contact area obtained by Thurn's and Cook's method, the differences reach more than 800% for every material. However, in the deep indentations, e.g. $h_{\max} \geq 400nm$, A_{proj} calculated according to every method are nearly identical.

Concurrently, for a further study, the comparison of the hardness calculated according to the aforementioned methods including the energy method is shown in Fig. 3. 24. It is clear that the values of the hardness calculated according to the modified method are less affected by the penetration depth in comparison with the other methods. They vary in a small range. On the other hand, the hardness $H_{O\&P}^{Sharp}$ which neglects the influence of the indenter tip has a large error in the shallow indentation, see Fig. 3. 24. $H_{O\&P}^{Sharp}$ decreases significantly with an increase of $h_{\max}$. Here, we should note that, only in deep indentations $H_{O\&P}^{Sharp}$ tends to be constant, e.g. the ratio of $h_{\max} / \rho$ is above 1.75, the influence of the indenter tip may be ignored. This is in good agreement with the experiment results (Xue et al., 2002). Moreover, the hardness obtained by the work-of-indentation approach, Thurn's and Cook's method also exhibit large errors in shallow indentations. H_{Enegry} decreases with an increase of the indentation depth, whereas Thurn's and Cook's method leads to the increase of the hardness followed by the increase of the indentation depth. The hardness $H_{O\&P}^{Tip}$ obtained by Oliver's and Pharr's method, which takes into account the tip influence, is also less affected by the indenter tip and it varies in a small range with an increase of the indentation depth. However, even in deep indentations, $H_{O\&P}^{Tip}$ always seems to be smaller than $H_{O\&P}^{Sharp}$ because the h_c calculated by the method proposed Oliver and Pharr is indeed different from the one measured directly from the finite element model, which leads to the calculated projected contact areas and the calculated hardness different values of.

We can clearly notice, in Fig. 3. 24, that the calculated hardness of $H_{Modified}$, H_{Enegry} and $H_{O\&P}^{Sharp}$ have a good agreement in deep indentations. However, $H_{O\&P}^{Tip}$ and $H_{T\&C}$ are little smaller than the other ones.

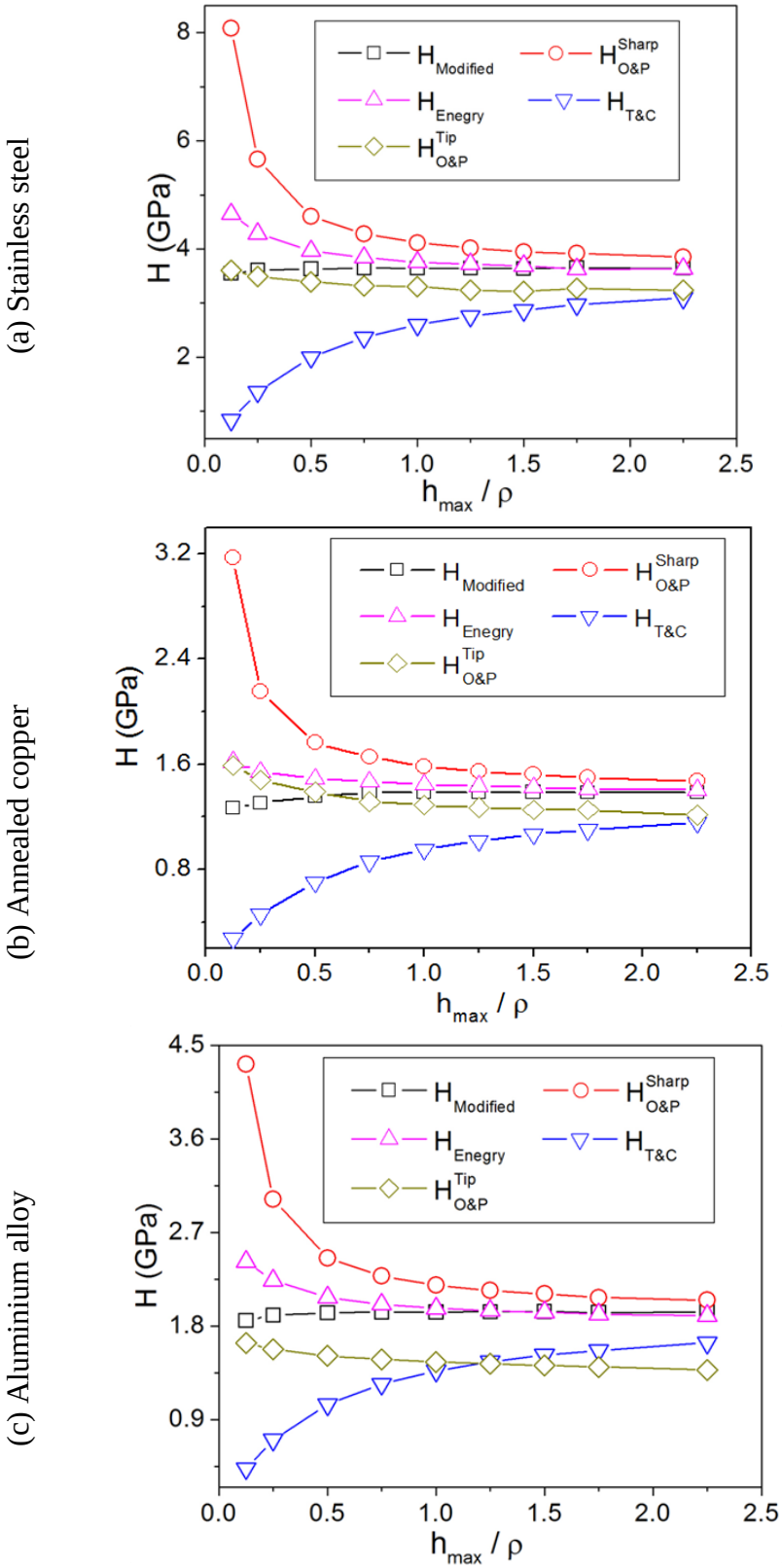

Fig. 3. 24. The hardness of materials determined by different methods.

3.3.2.2. Conclusions

This chapter examines the tip effects of the imperfect indenters on the calculation of hardness. The results show that the hardness will have a large error if the imperfection of the indenter tip is neglected, particularly when the imperfect indenter has a larger shape deviation. Subsequently, a modified method is derived from the geometrical relations of the imperfect indenter tip and comparisons with other frequently used methods, including the work-of-indentation approach which can account the tip effects of the imperfect indenters, are shown in Fig. 3. 24. Once all the methods for the estimation of the hardness are compared, we notice that they are outstandingly affected by the penetration depth. When the indentation depth is ultra low, they lead to a significant error in the estimation of the hardness. However, all of them tend to be constant as the indentation depth is increased. Especially, the calculated hardness which are obtained according to the Oliver's and Pharr's method, the energy method and the modified method in deep indentation are nearly identical. Furthermore, the illustrations show that the modified method can perfectly improve the accuracy of the calculated hardness even at an ultra shallow indentation depth. For example, when $h_{\max} / \rho \geq 0.5$, $H_{Modified}$ starts to be a constant.

3.4. Example

3.4.1. Identification of the material properties of a thin film coating

The experiment was carried out in "the Characterization Laboratory in the Engineering Physics Department at Ecole Polytechnique" in Canada. In this experiment, a sample with ~100 μm thickness of plasma-sprayed coating (ZrO_2-Y_2O_3) formed on a stainless steel substrate was chosen for illustration. The proportion of ZrO_2 and Y_2O_3 is 93:7 (mol) and the porosity of the coating is in the range of 5-10%. A Nano-triboindenter instrument (Hysitron, 2005) equipped with a Berkovich indenter was used. The measurement procedure involved continuous monitoring of the load and of the indenter displacement during the loading and the unloading processes. In the left part of Fig. 3. 25, the experimental data are represented by black squares. The indentation processes were executed by force control and the maximum load was 4908 μN. The loading history can be seen in the right part of Fig. 3. 25. The loading process lasts from 0 to 5 seconds. Then, the loading is held constant at the maximum load for 2 seconds. Afterwards, the unloading process is performed during 7 to 12 seconds.

Correspondingly, the indentation hardness of the coating H equals 16.5 GPa, and the reduced Young's modulus E_r equals 192.0 GPa, when they are calculated on the basis of the method

proposed in (Oliver and Pharr, 1992). If the Poisson's ratio of the plasma-sprayed coating is assumed to be 0.3, its Young's modulus equals $E = 209.9\ GPa$. More details for calculating H and E can be seen in chapter 2.

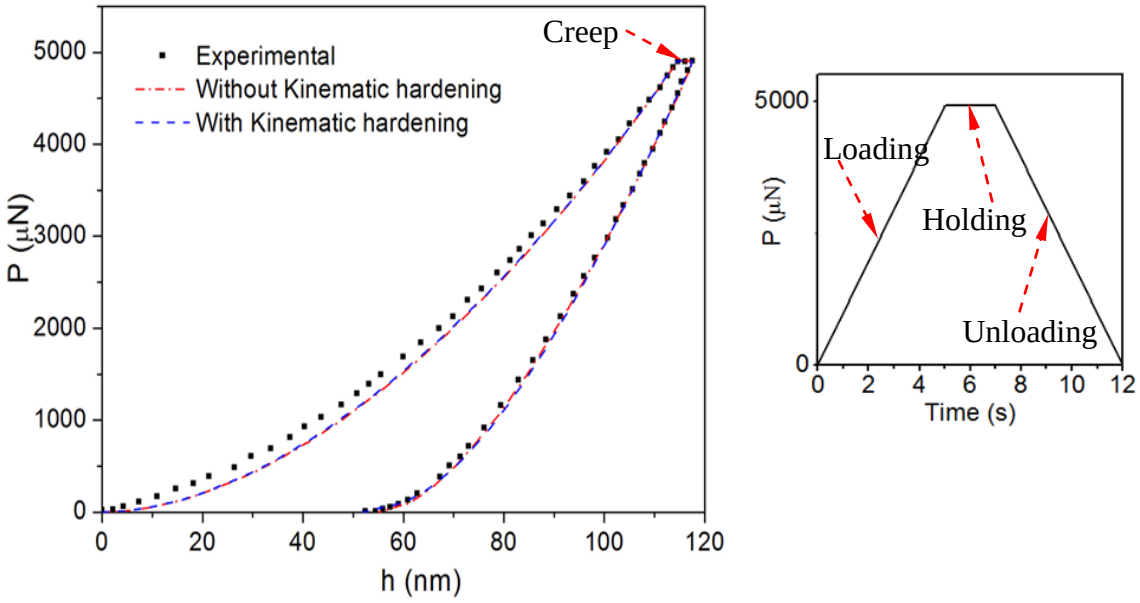

Fig. 3. 25. Experimental load-displacement curves and optimized load-displacement curves obtained with a perfect conical indenter. Black squares are experimental data; dash dot curve and dash curve are optimized curves.

In this experiment, the loading history used to measure the material parameters of the plasma-sprayed coating is loading-holding-unloading. Thus, the kinematic hardening may be ignored because according to (Dettmer and Reese, 2004), the effect of kinematic hardening is not significant without reloading. In order to evaluate this, two constitutive formulations: one with kinematic hardening and another without kinematic hardening, are respectively introduced into the numerical model. Then the material parameters of the coating are evaluated by inverse analysis involving the Gauss-Newton method, see details in chapter 2. In the following parts, all the simulation studies are performed using the finite element code METAFOR.

Given that the thickness of the coating of the measured sample is ~100 μm and the maximum indentation depth is lower than 120 nm (see Fig. 3. 25), the indentation depth is below 1/800 of the thickness of the coating. Therefore, it can be considered that the experimental $P-h$ curve is not affected by the substrate as it has been demonstrated that for hard coating and soft substrate material, the measured results are normally no longer affected by the substrate when the indentation depth is under 1/30 of the thickness of the coating (Chen and Vlassak, 2001). Thus, herein, in order to simplify the problem and to save computation time, a 2D finite element model

is adopted and it is modelled only with the coating material (see Fig. 3. 26). The 2D axisymmetric finite element is defined with 7 μm radius and 7 μm height. It is established using 1062 four-noded quadrilateral elements. In the experiment, the indenter which is used is a three-sided Berkovich indenter. Therefore, in 2D computations, the Berkovich indenter can be replaced by a conical indenter with the half apex angle of $\theta = 70.3^{\circ}$ according to the investigation of (Albrecht et al., 2005). Furthermore, the Coulomb friction model is assumed in the contact region with the friction coefficient μ =0.15. The indentation processes are executed by imposing the load on the indenter and the maximum load equals 4908 μN , which is identical to the maximum load executed in the experiment. The loading history is also exactly the same as that performed in the experiment as we can see in the right figure of Fig. 3. 25.

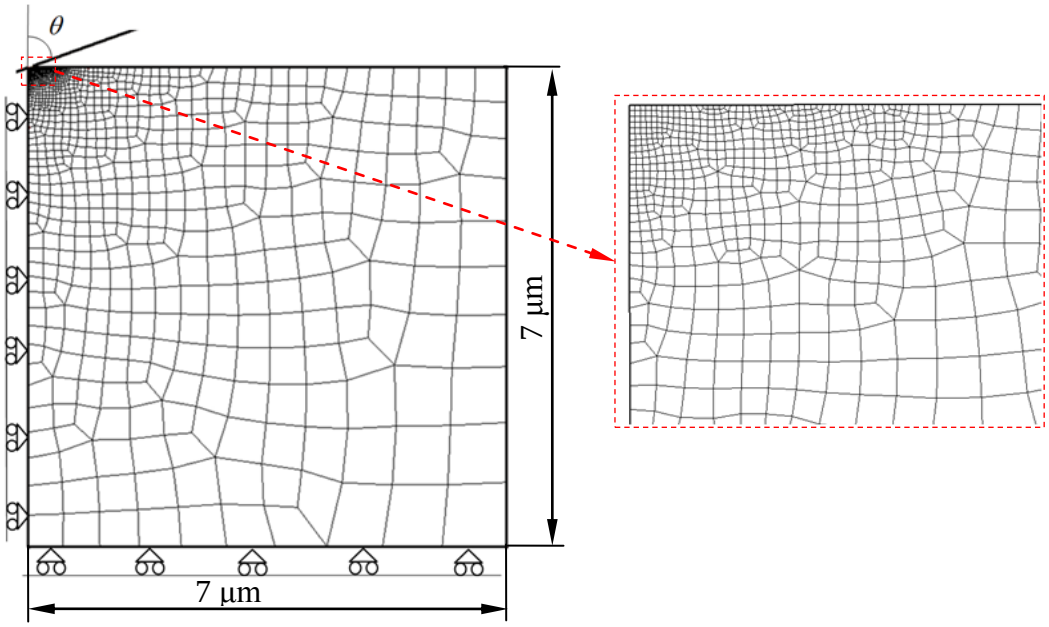

Fig. 3. 26. 2D axisymmetric finite element model for the identification of the coating property.

The optimized results of the two cases compared to the experimental data are shown in Fig. 3. 25. The cases with and without the kinematic hardening are represented by the dash curve and the dash dot curve, respectively. It is clear that the optimized $P-h$ curves have a good agreement with the experimental one especially for the unloading curves and that the optimized $P-h$ curves for the cases with and without kinematic hardening are almost identical. The final identified coating parameters are listed in Table. 3. 6. As we can see in the first two rows of the table, most identified material parameters do not have a significant difference in both cases except the plastic parameters of Q and ξ.

The corresponding simulated hardness are 15.0 and 15.2 GPa, respectively, for both cases. The differences are lower than 9% compared to the experimental hardness, H =16.5 GPa. Moreover,

when the identified Young's moduli are compared to the experimental one, $E = 209.9\,GPa$, the differences are lower than 3%. Besides, it can be seen that D and m also agree well in both cases.

Table. 3. 6. The identified material parameters for the investigated coating.

ρ (nm)	E (GPa)	σ_y^0 (GPa)	Q (GPa)	ξ	H_{kh} (GPa)	H_{kb}	D (s^{-1})	m	H (GPa)
0	206.8	8.91	0.21	0.52	68.41	0.11	0.040	0.58	15.0
0	203.8	8.99	15.89	5.41	×	×	0.046	0.54	15.2
282	171.4	5.15	1.61	0.76	42.55	0.32	1.018	4.04	11.0
219	167.6	7.70	0.03	8.34	×	×	0.056	2.06	11.5

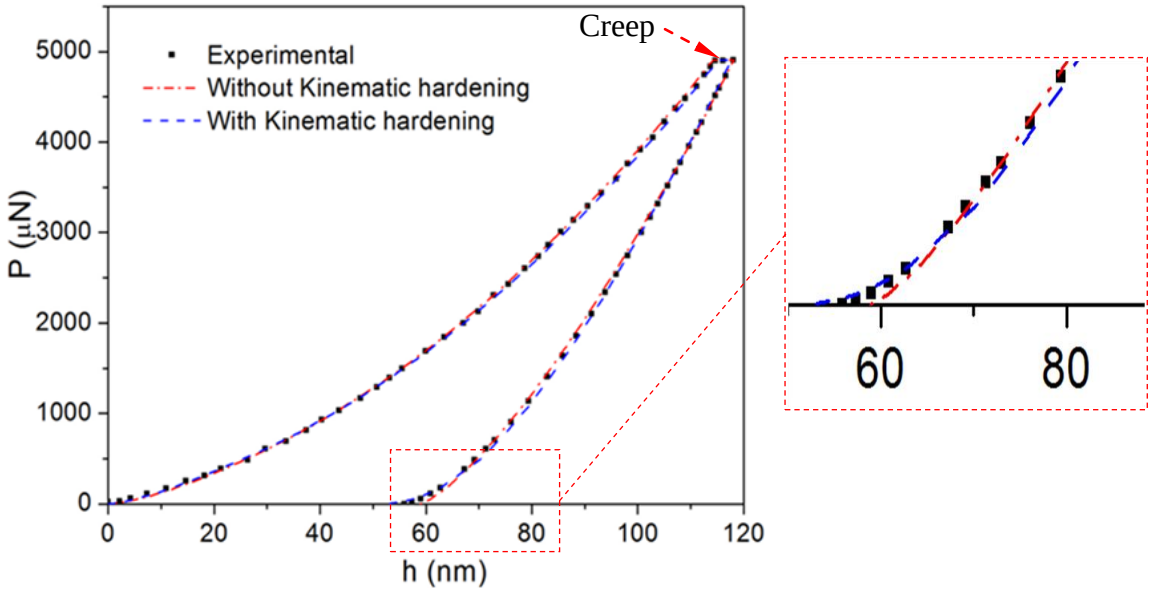

Fig. 3. 27. Experimental load-displacement curves and optimized load-displacement curves obtained by an imperfect conical indenter. Black squares are experimental data; dash dot curve and dash curve are optimized curves.

However, we can clearly see that in Fig. 3. 25, when the indenter starts penetration into the specimen, the optimized unloading curves are lower than the experimental curve. This is supposed to be due to the tip rounding of the indenter used in the experiment because it never has a perfect sharp tip as designed (Yu et al., 2004; Jeong and Lee, 2005; Antunes et al., 2007). For this reason, a conical indenter with a rounded tip is modelled like the one shown in Fig. 3. 21. The radius of the indenter rounded tip, ρ is defined as a variable parameter in the optimization procedure. The optimized load-displacement curves for the cases with and without

the kinematic hardening are shown in Fig. 3. 27. It is clear that the optimized load-displacement curves have a good agreement with the experimental curve.

The corresponding identified material parameters for this coating and the optimized radius of the rounded tip are listed in Table. 3. 6. As can be seen in the last two rows of this table, the optimized radius of the rounded tip equals 282 and 219 nm, respectively, for the cases with and without the kinematic hardening. Both are in the reasonable range according to the investigation (Fischer-Cripps, 2002).

The corresponding hardness and Young's modulus calculated by the methods used for the imperfect indenters, which are discussed in chapter 3.3.2, can also be seen in Table. 3. 6. The differences of the hardness and Young's moduli are over than 30% and 18%, respectively, in comparison with the experimental ones. Concerning to the differences between simulated data and experimental data, they may be led by the factors: the calculation of the contact depth, the surface roughness of the specimen and the porosity of the coating. For calculating A_{proj}, the contact depth h_c is calculated according to Eq. (2.40) in the experiment. In the simulations, h_c is directly measured from the finite element model, which includes the effect of piling-up or sinking-in. In addition, the differences include also the influence of surface roughness of the specimen. Particularly, for a conical indenter with a large rounded tip, the influence of the surface roughness should be significant. In the numerical simulations, the friction coefficient is set to 0.15 to simplify the problem. Furthermore, when plasma-sprayed coating is being built, some void spaces exist in the coating. According to the investigations (Winnubst et al., 1983; Zhao et al., 2009), the Young's modulus of a coating is dependent on this porosity. The Young's modulus will decrease significantly with an increase of the porosity. The relationship of them can be fitted according to experimental results for a ZrO_2-Y_2O_3 coating (Winnubst et al., 1983),

$$E(GPa) = (221 \pm 4)\exp[(-2.7 \pm 0.5) \times \text{porosity}]. \tag{3.19}$$

Thus, for a coating with 10% porosity, its Young's modulus would decrease to 169 GPa. This denotes that the experimental Young's modulus may have a large error.

Simultaneously, it is clear that the optimized load-displacement curves which take into account the tip rounding are closer to the experimental one. Particularly, for the case with kinematic hardening, the unloading curve is closer to the experimental data in comparison with the optimized load-displacement for the case without the kinematic hardening, e.g. when $h_{\max} < 65\,nm$, see the right part of Fig. 3. 27. Therefore, it is believed that the identified material parameters determined by the imperfect conical indenters for the case with the kinematic hardening are more reliable because the corresponding load-displacement curve is almost identical compared to the experimental curve.

3.4.2. Hardness testing

In order to simplify the problem, the hardness of the coating is investigated by a perfect sharp conical indenter in the following parts and the coating's mechanical properties are described by the material parameters without kinematic hardening. They are listed in the second row in Table. 3. 6.

3.4.2.1. Hardness on top surface of coating

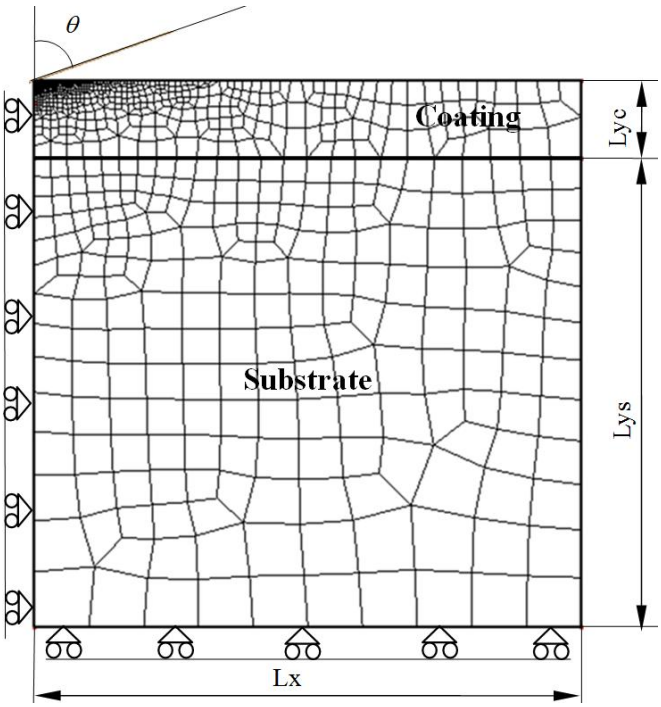

Fig. 3. 28. 2D axisymmetric finite element model for coated material.

Generally, the hardness on the top surface of coating is focused on in most of the published papers (Lin and Berndt, 1995; Leigh and Berndt, 1997; Li et al., 2004). It represents the work condition of the coating in practical applications. However, it is reported that hardness depends on the indentation depth. In order to investigate this problem, another 2D axisymmetric finite element model is modelled using 958 four-noded quadrilateral elements. There are 737 elements for the coating and 221 elements for the substrate. A finer mesh near the contact region and a gradually coarser mesh further from the contact region are designed to ensure numerical accuracy, see Fig. 3. 28. The model is designed with the radius, $Lx = 7\ \mu m$. The thickness of the coating is presumed as $Lyc = 1\ \mu m$ and the thickness of the substrate is presumed as $Lys = 6\ \mu m$. Herein, the substrate is assumed as stainless steel, which is also used in (Mata and Alcala, 2004).

Its plastic behaviour is approximated by the power law description as Eq. (2.66). The work-hardening exponent, the Young's modulus and the initial yield stress are defined as $n = 0.19$, $E = 200\,GPa$ and $\sigma_y^0 = 675\ MPa$, respectively and the Poisson's ratio is set to 0.3.

The hardness are computed at the maximum load P_{max} varying from 251 to 13195 μN. The hardness versus the ratio of the indentation depth and the coating's thickness are shown in Fig. 3. 29. It can be seen that for moderate loads, i.e. the indentation depth is lower than about 5% of the coating's thickness, the hardness are nearly constant and agree well with the calculated hardness. This one has previously been estimated by the pure coating model shown in Fig. 3. 26. However, the hardness decreases significantly with an increase of h_{max} as expected, because when h_{max} increases, the identified hardness of the coating gets influenced more by the substrate (the hardness of the substrate is 4.3 GPa. It can be seen in Fig. 3. 32). Therefore, as usual, the indentation depth is required not exceed to 5% to 10% of the thickness of the coating (Chen and Vlassak, 2001). This allows for eliminating the substrate effects. Whereas, on the other hand, an indentation depth as large as possible should be used in order to eliminate indentation size effect (ISE) and specimen roughness effect which are usually more significant at lower indentation depth. Thus, the definition of the critical ratio of coating thickness to indentation depth is a challenge in identification of thin coatings.

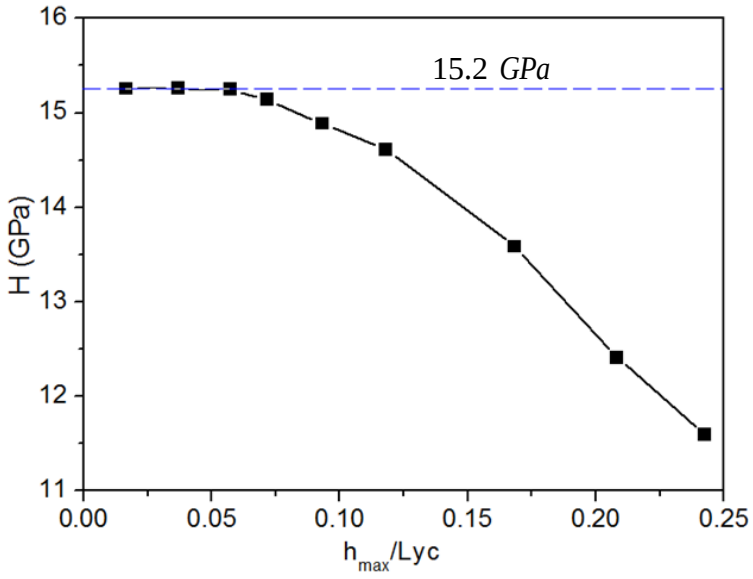

Fig. 3. 29. Hardness versus the ratio of the indentation depth versus the coating's thickness.

3.4.2.2. Hardness on vertical cross section

In some published papers (Lin and Berndt, 1995; Leigh and Berndt, 1997; Li et al., 2004), researchers measured the hardness on the top surface of a coating, as stated in the section 3.4.2.1. The hardness is normally reported as an average value over a certain number of readings from random indentations on the top surface of the coating. But, such hardness is not sufficient to understand the mechanical properties and their relationships with the microstructure of the coating. Thus, it is necessary to evaluate the hardness within coating and assess its relation with the substrate. Herein, a 3D model is designed and shown in Fig. 3. 30 to describe the schematic of different indentation impressions and geometrical characteristics of the finite element models, which are used in the following investigations.

In order to obtain the same projected contact areas, in the following computations, the load is applied through control of the displacement of the indenter. The maximum indentation depth is set as, $h_{\max} = 118\ nm$, which is nearly identical as the indentation depth reached in the experiment. As a consequence, the radius of the projected contact area at the maximum indentation depth is about 329 nm. Thus, for decreasing the number of elements and save computer time, the size of the used model is designed with 200 μm length and 4 μm height. The thickness of the coating is 100 μm and the thickness of the substrate is assumed as 70 μm, see Fig. 3. 30.

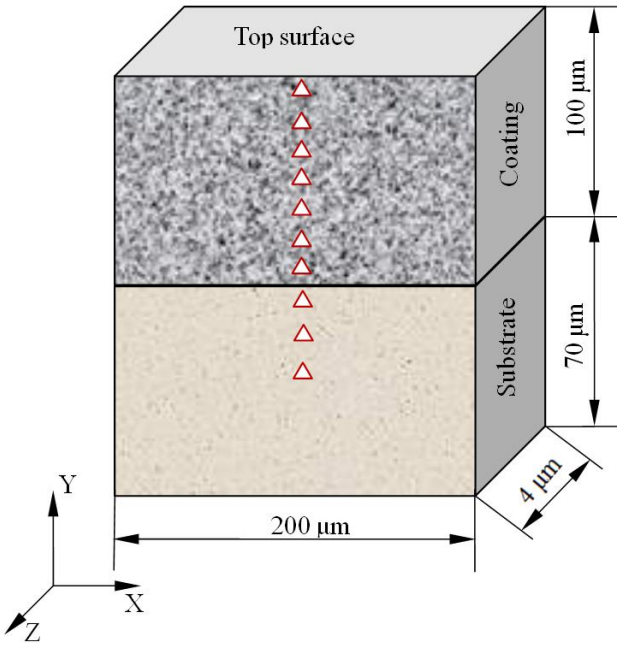

Fig. 3. 30. Schematic of different indentation impressions (triangles) and microstructural characteristics of the used model.

On the cross section of the coating, seven hardness values are calculated, which are positioned at a distance of 0.52, 2.5, 25, 50, 75, 97.5 and 99.48 μm from the coating-substrate interface, respectively. Besides this, on the cross section of the substrate, the hardness positioned at 0.52, 5 and 10 μm from the coating-substrate interface are calculated. Therefore, a total of ten 3D finite element models are designed for the foregoing hardness investigations. The half symmetric 3D finite element model for the hardness testing on the distances of 50 μm from the coating-substrate interface within coating is shown in Fig. 3. 31. This model is established by 11870 eight-noded 3D solid elements. There are 11510 elements in the coating and 360 elements in the substrate. At maximum load, more than 800 contacted nodes are active in the contact region. The bottom surface of the model located on the X-Y plane is fixed as boundary condition and the surface on Y-Z plane is defined as symmetric surface. The computed results are evaluated to ensure they are not affected by the boundaries before the hardness testing.

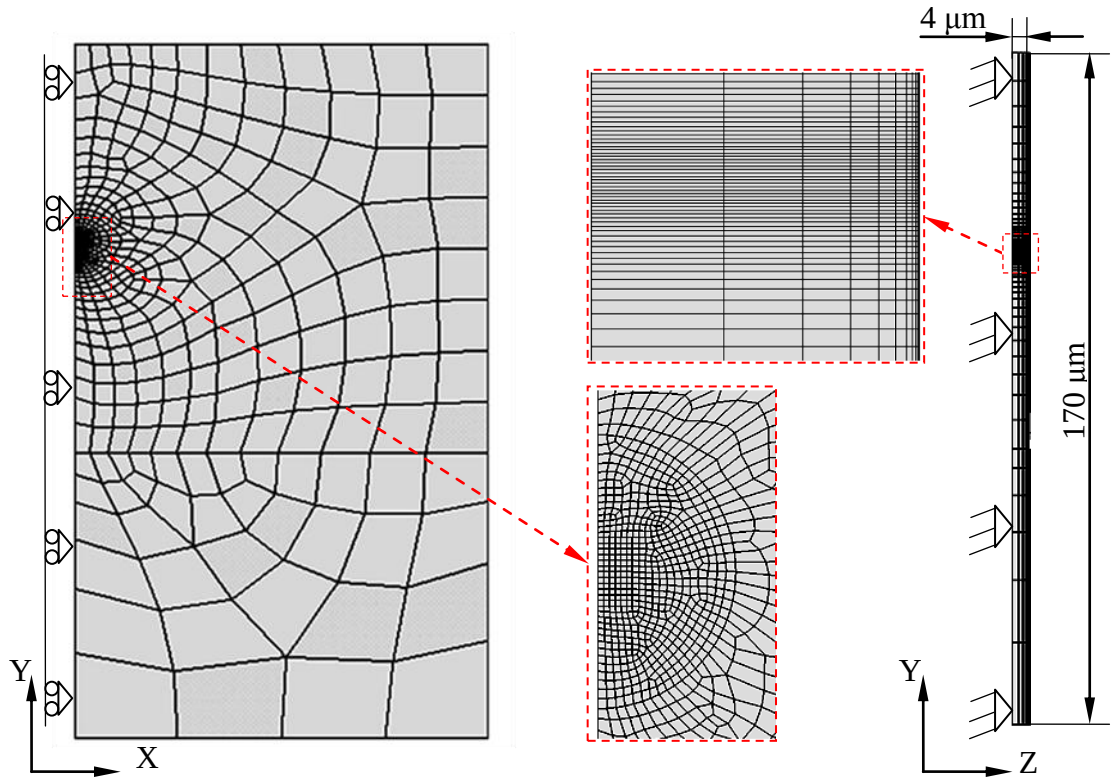

Fig. 3. 31. 3D Finite element model for hardness tests. The indentation position is on the distance of 50 μm from the coating-substrate interface.

The hardness distribution over the cross section of the sample is shown in Fig. 3. 32. It can be seen that within the coating, where the indentation positions are far from the coating-substrate interface and the top surface, the hardness is not affected by external effects. The maximum hardness is 15.4 GPa, which appears in the middle of the coating. It agrees well with the

calculated hardness (15.2 *GPa*), which is obtained by use 2D model. The difference is less that 2%.

However, it must be noted that the coating's hardness is affected significantly by the substrate close to the interface. It can be seen that the hardness of the coating decreases largely with a decrease of the distance from the coating-substrate interface, because the substrate's hardness is much smaller than the coating's hardness. The hardness at a distance of 0.52 μm from the coating-substrate interface within the coating decreases to 7.4 *GPa* as the substrate is too soft compared to the coating. Besides, when the indentation position is too close to the free surface of the coating, the hardness decreases again because the top surface is not constrained.

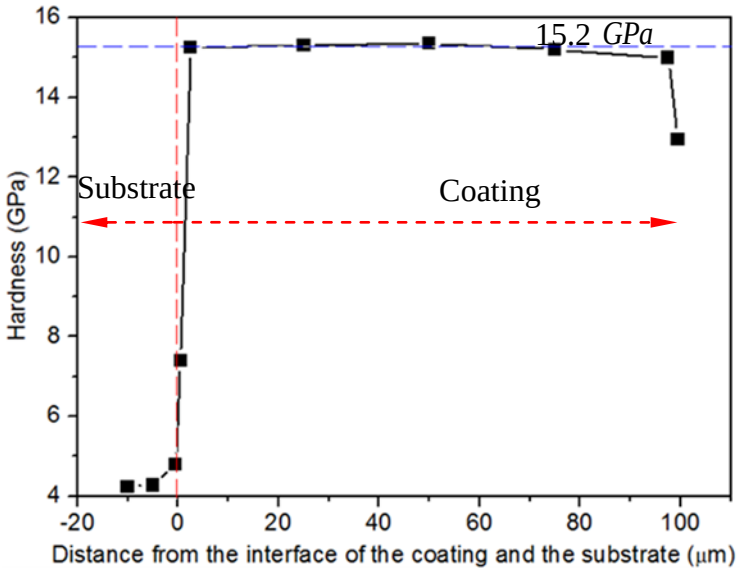

Fig. 3. 32. Hardness distributions on the cross section of the sample (black squares), (the blue dash line represents the calculated hardness of 15.2 *GPa*. It is obtained by the 2D model shown in Fig. 3. 26).

3.4.3. Conclusions

In the present work, the mechanical properties of a plasma-sprayed coating are evaluated using nanoindentation testing. According to the experimental $P-h$ curve data, the material parameters of the plasma-sprayed coating are determined via numerical optimization algorithms combined with reverse analysis. The $P-h$ curves produced by the perfect sharp indenter and the indenters with rounded tips are compared. It is found that the identified material parameters determined by the imperfect indenter for the case with the kinematic hardening are more reliable although the calculated hardness and Young's modulus have large differences compared to the

ones obtained in the experiment. This is because the $P-h$ curve produced by the imperfect indenter is nearly identical compared to the experimental data.

Subsequently, based on the identified material parameters, the hardness on the top surface of the plasma-sprayed coating as a function of the indentation depths is studied. The results show that the measured hardness will decrease significantly with an increase of the indentation depth. Furthermore, the relation of the hardness on the vertical cross section of the coating and the substrate is assessed. The results show that the hardness on the cross section of the coating are decreased significantly under the effect of the soft substrate, e.g. when the indentation impression is too close to the coating-substrate interface.

CHAPTER 4
STRATEGIES FOR THE IMPROVEMENT OF THE IDENTIFIABILITY OF MATERIAL PARAMETERS

Overview

This chapter illustrates how the correlations of the material parameters are assessed using the cosine matrix of the Hessian matrix which is derived from the objective function. The aforementioned optimization method combined with sensitivity analysis is used to minimize the objective function. The efficiency and reliability of direct differentiation sensitivity are shown by comparing with finite difference sensitivity. At the same time, the effect of the residual imprint data on identification of the material parameters is compared to the case without taking into account the imprint data. Subsequently, two strategies for improving the identifiability of material parameter are introduced. One relies on changing the tip shape of indenter and another relies on altering the loading history.

Contents

4.1. Assessment of the correlation of the material parameters

This part illustrates the assessment of the correlation of the material parameters through the use of the aforementioned optimization method combined with sensitivity analysis. The illustrations are perform in HEPPERDANG finite element code because the programs for the assessment of the correlation of the material parameters were developed in HEPPERDANG by (Rauchs, 2009). Because contact friction does not affect the correlation of the material parameters, in the following parts, the contact friction is ignored and the friction coefficient is set as zero.

4.1.1. Identification of material parameters

Herein, the objective function is defined as the difference between the experimental and the modelled displacement-into-surface, $\bar{h}$ and h. The sensitivity is defined as the derivative of the objective function with respect to the material parameter, x_j. After defining the objective function and the sensitivity analysis, the objective function can be minimized by using some gradient-based numerical optimization algorithms because they offer the potential for a fast parameter identification. In the present work, Gauss-Newton method is used. The whole optimization procedure is shown in Fig. 4. 1.

The elasto-plastic material listed in Table. 4. 1 is chosen for illustrations. Young's modulus is represented as E and the initial yield stress is represented as σ_y^0. The evolution of the yield stress σ_v are described by the Voce-type hardening law,

$$\sigma_v = \sigma_y^0 + Q[1-\exp(-\xi s)], \tag{4.1}$$

where, s is the plastic arc length. The material kinematic hardening is described by Armstrong-Frederick law with the non-linear kinematic hardening parameters, H_{kin} and H_{nl}. According to (Rauchs, 2008), the relationship between back stress and plastic strain rate is written as

$$\dot{\alpha} = \sqrt{\frac{2}{3}} H_{kin} H_{nl} \dot{\varepsilon}_p - \sqrt{\frac{3}{2}} H_{nl} \dot{s} \alpha, \tag{4.2}$$

where ε_p is the plastic strain.

The 2D finite element model which was used is shown in Fig. 4. 2. It is designed with 15 *mm* radius and 15 *mm* height. This model includes 509 nine-noded quadrilateral elements where a finer mesh near the contact region and a gradually coarser mesh further from it are designed to ensure numerical accuracy. The spherical indenter which has a long shaft is modelled as a

flexible body. It is modelled by 141 nine-noded quadrilateral elements and its radius equals 1.25 mm.

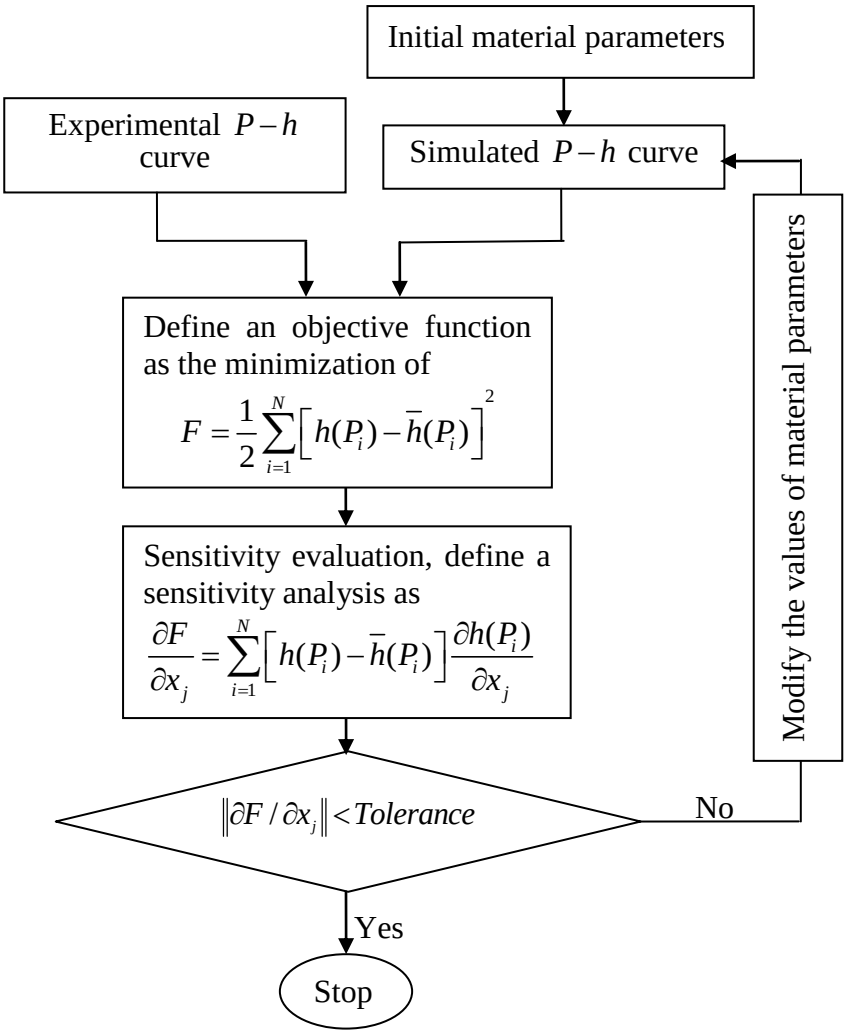

Fig. 4. 1. The schematic flow chart of the identification the material parameters.

Table. 4. 1. The material properties of elasto-plastic materials (isotropic hardening).

	$E\ (GPa)$	υ	$\sigma_y^o\ (MPa)$	$Q\ (MPa)$	ξ
Real input	74.5	0.3	295	350	5
Initial value	100	0.2	300	300	1
Identified	73.8	0.19	321	335	4.3
Error (%)	0.9	36.9	8.8	4.3	14.0

Herein, the experimental $P-h$ curve is in fact a set of pseudo experimental data which are obtained by applying a load on the spherical indenter in HEPPERDANG code (Rauchs, 2009). In order to simplify the problem, experimental noise is neglected in the present work. The input material parameters corresponding to isotropic hardening are listed in the first row of Table. 4. 1. The initial values of the material parameters are listed in the second row of Table. 4. 1. Then, the whole optimization procedure is performed in HEPPERDANG code.

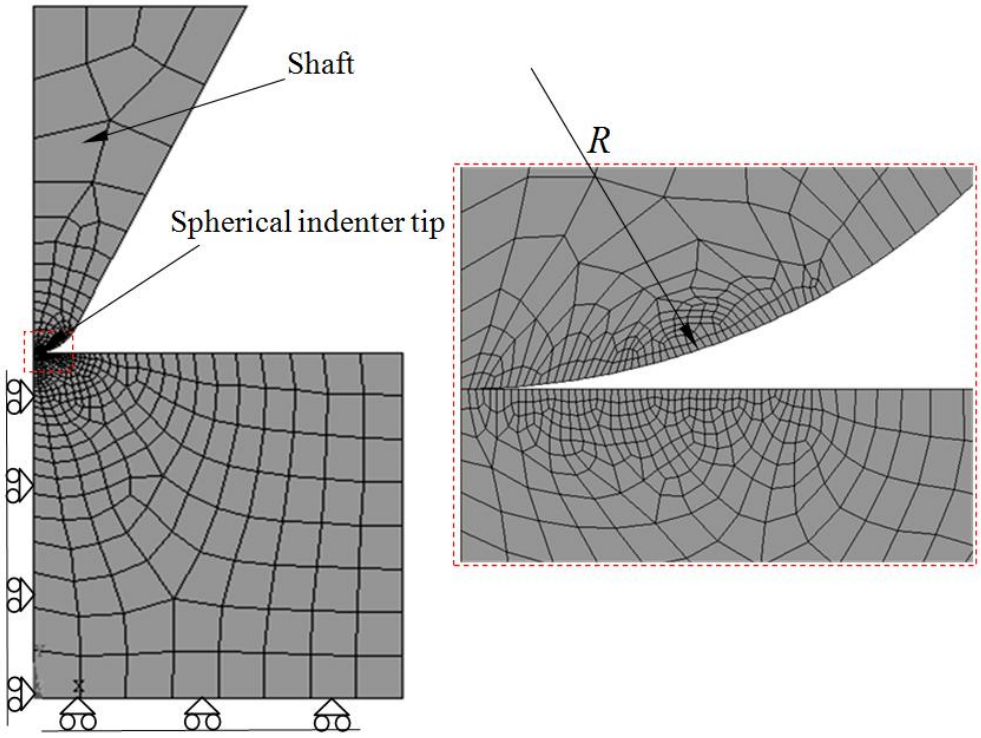

Fig. 4. 2. 2D axisymmetric finite element model (509 elements for specimen and 114 elements for indenter).

Fig. 4. 3 shows the convergence history of the objective function as well as the optimized $P-h$ curve and which is compared to the pseudo experimental one. It is obvious that the optimal $P-h$ curve has a good agreement with the pseudo experimental one. The corresponding optimal material parameters are listed in the third row of Table. 4. 1. We should note that, except for Young's modulus, most of the material parameters do not have a good agreement with the real input material parameters. Particularly, for υ and ξ, the errors are absolutely significant. Both are larger than 14% as we can notice in the last row of Table. 4. 1. Moreover, the evolutions of the material parameters are shown in Fig. 4. 4.

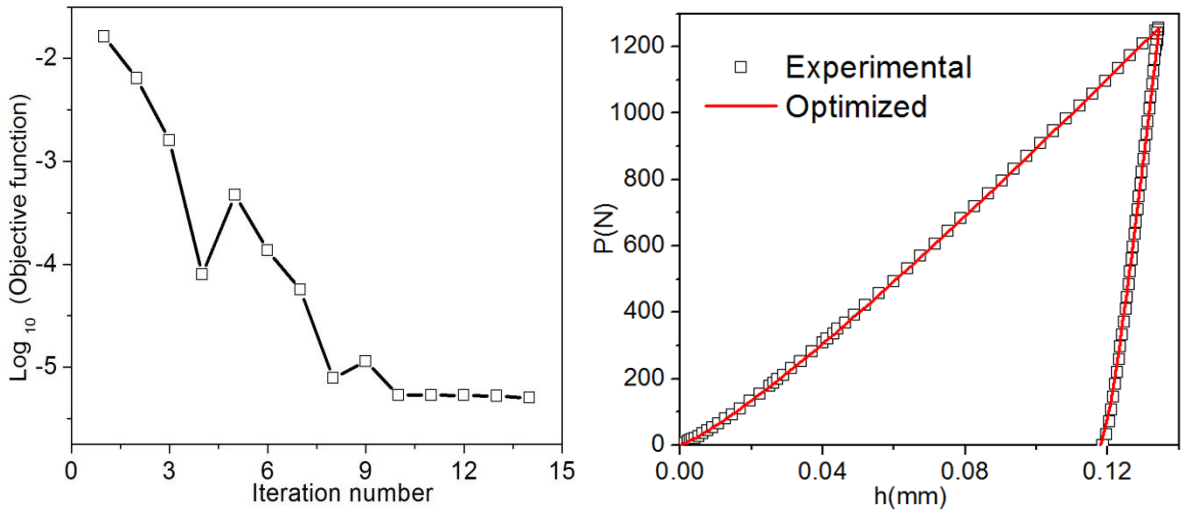

Fig. 4. 3. The convergence history of the objective function (left) and the optimized load versus the indentation depth curve compared to the pseudo experimental one (right).

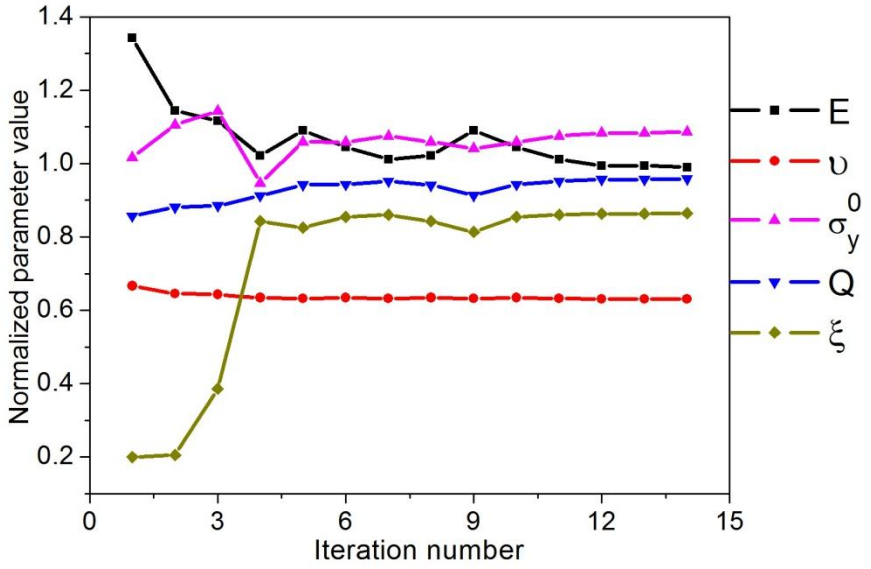

Fig. 4. 4. The evolutions of the material parameters.

For many metals, the Young's moduli and the Poisson's ratios are known. Thus, the Young's moduli and the Poisson's ratios of the previous material are fixed in the following part. Only three plastic parameters are evaluated to investigate the accuracies of evaluated material parameters. Three sets of initial values for the plastic parameters are listed in Table. 4. 2. The same optimization procedure is used. The optimized $P-h$ curves compared to the pseudo experimental one are shown in Fig. 4. 5. It is clear that the optimized $P-h$ curves have a good agreement with the pseudo experimental one for the initial values which are set as the cases 1

and 2. For the case 3, the loading curve agrees well with the experimental one, whereas the unloading curve does not have a good agreement with the experimental unloading curve. The identified material parameters are listed in Table. 4. 3. It is noted that for the case 1, all identified material parameters have a larger error. For the case 2, the errors of σ_y^0 and Q are below 5%, yet the error of ξ is 16.0% compared to the input value. For the case 3, the error of σ_y^0 is 2.0%, whereas the errors of the other two plastic parameters are very large. Particularly for ξ, its error reaches 36%. Moreover, the convergence histories of the objective function and the evolutions of the material parameters can be seen in Fig. 4. 6 and Fig. 4. 7, respectively. In Fig. 4. 7, the normalized material parameter value is defined as the evaluated material parameter value divides the input material parameter value.

Table. 4. 2. Initial values of material parameters.

	σ_y^o (MPa)	Q (MPa)	ξ
Case 1	500	300	4
Case 2	200	400	6
Case 3	400	300	7

Table. 4. 3. Identified material parameters for the different sets of initial values.

	σ_y^o (MPa)	Q (MPa)	ξ
Real input	295	350	5
Case 1	318	288	3.9
Error (%)	7.8	17.7	22.0
Case 2	283	365	5.8
Error (%)	4.1	4.3	16.0
Case 3	289	288	6.8
Error (%)	2.0	17.7	36.0

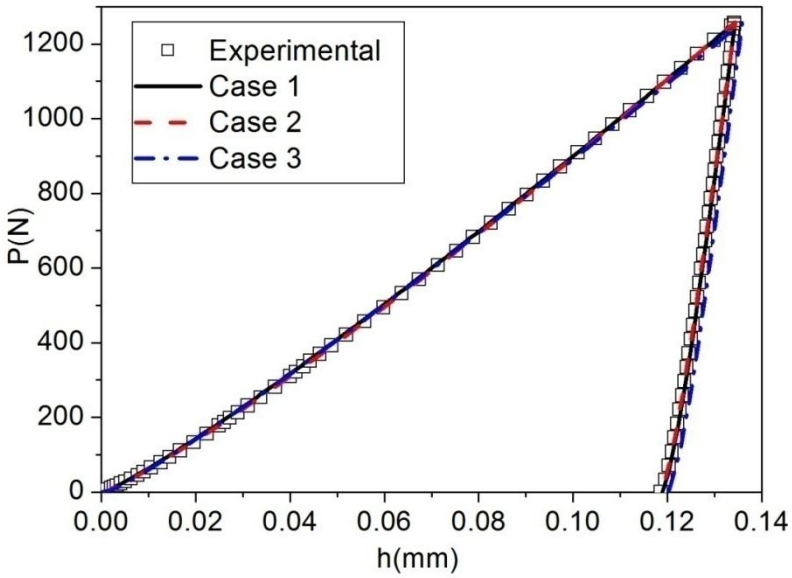

Fig. 4. 5. The optimized load versus the indentation depth curves for the different sets of the initial values compared to the pseudo experimental one.

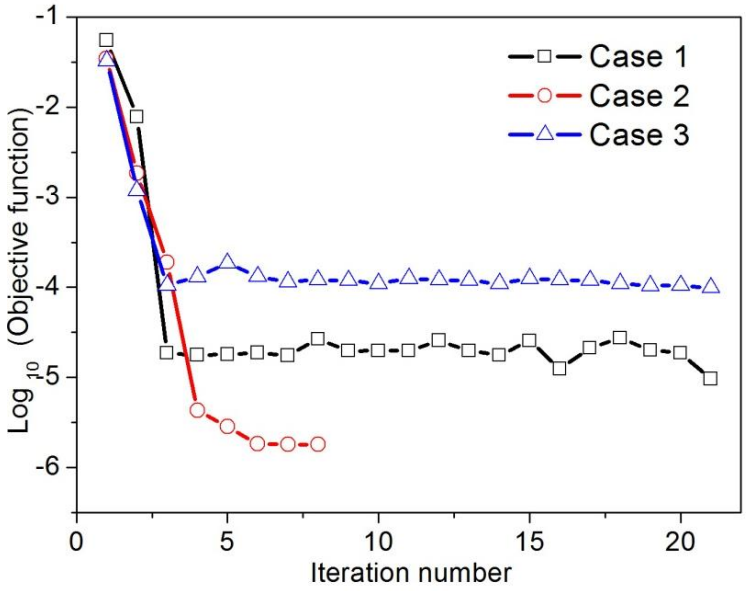

Fig. 4. 6. Convergence histories of the objective function for the different sets of the initial values.

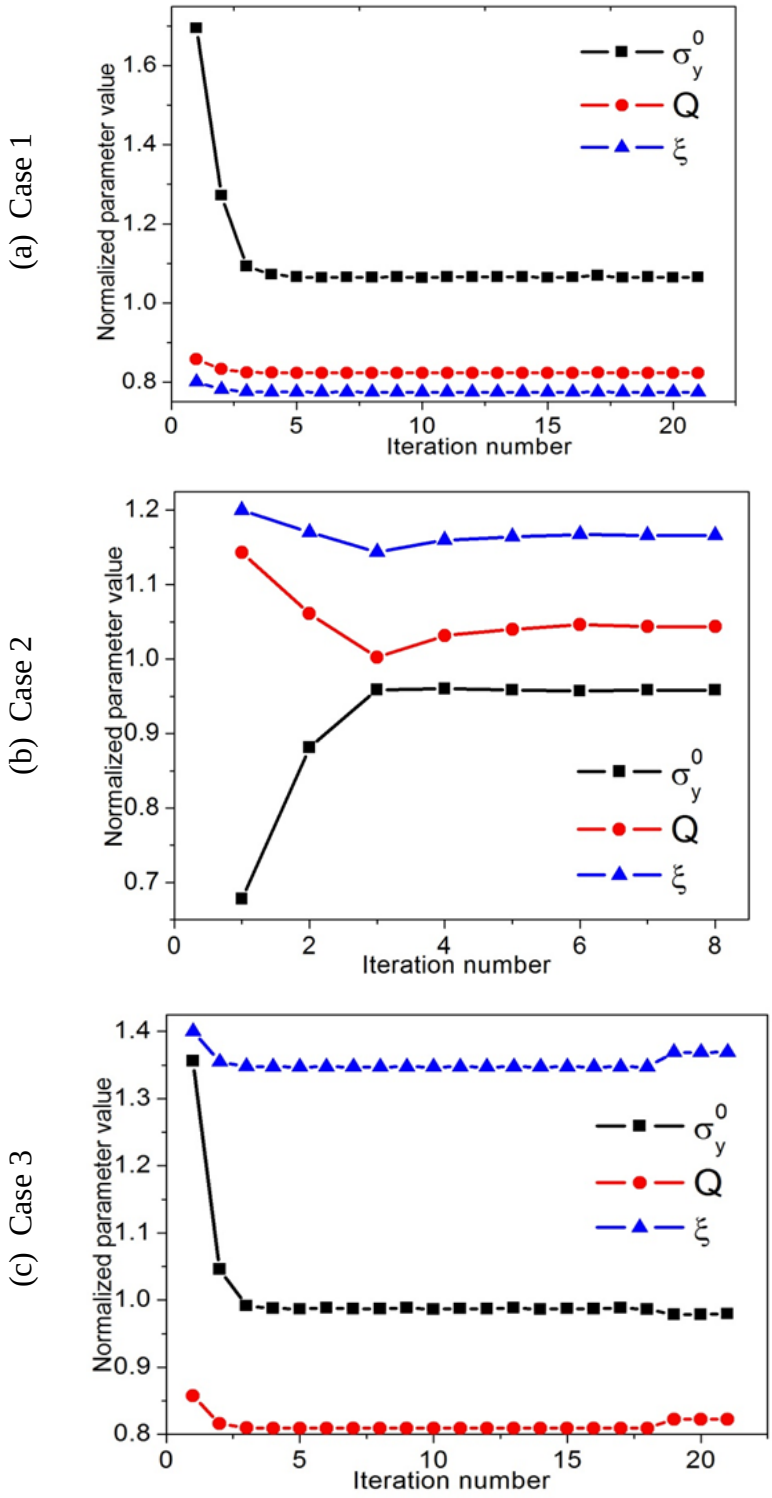

Fig. 4. 7. Parameter evolutions for the different sets of the initial values.

The effective plastic strain-effective plastic stress curves for the finial evaluated material parameters and the real input material parameters are compared in Fig. 4. 8. It is clear that all the curves do not have a good agreement with the one for the real input material parameters.

Through the previous investigation, it can be seen that the evaluated material parameters always have a larger error compared to the real input ones although the $P-h$ curves have a good agreement with the pseudo experimental one. Furthermore, the accuracies of the evaluated material parameters cannot be improved by decreasing the number of identified material parameters. The large errors for the identified material parameters may be due to the fact that some material parameters are strongly coupled with each other.

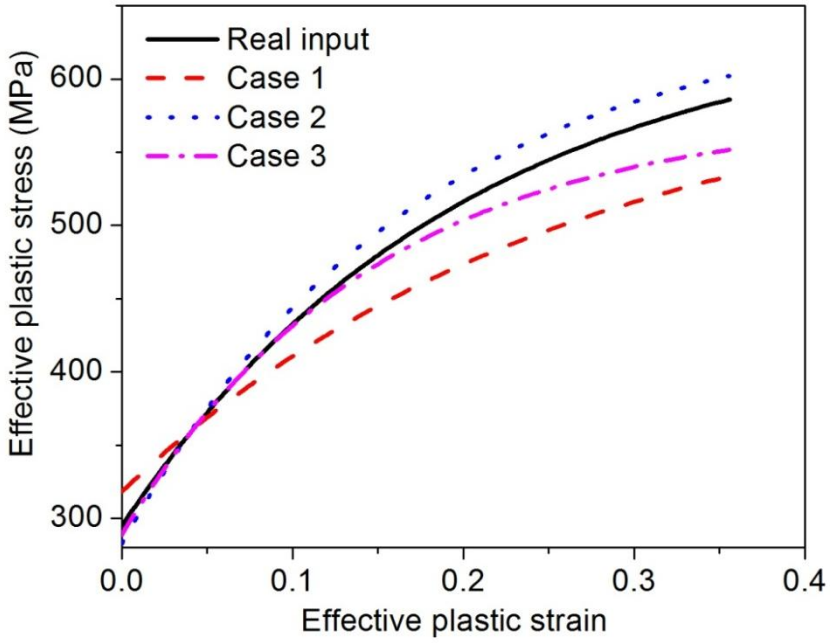

Fig. 4. 8. The effective plastic strain-effective plastic stress curves for the identified material parameters and the real input material parameters.

4.1.2. Comparison of parameter correlations

The correlations of the material parameters, which are assessed by the cosine matrix of Hessian matrix, can be computed by Eq. (2.67). In Table. 4. 4, the data in the upper triangle are obtained from an objective function including residual imprint data. On the other hand, the data in lower triangle are obtained from an objective function which does not include imprint data. See the data in upper triangle, the correlations of E with other material parameters decrease due to the effect of the imprint data. However, the couplings among the plastic parameters, σ_y^0, Q and ξ,

do not decrease due to the effect of such data: they are always 1.0. It is the same for υ: the imprint data do not improve its correlations with the plastic parameters in a significant way.

Table. 4. 4. Cosine Hessian matrices of the tested material: upper triangle with imprint data, lower triangle without imprint data.

	E	υ	σ_y^o	Q	ξ
E	1	0.96	0.90	0.86	0.88
υ	0.98	1	0.97	0.94	0.96
σ_y^o	0.94	0.97	1	1.00	1.00
Q	0.91	0.94	1.00	1	1.00
ξ	0.93	0.96	1.00	1.00	1

4.2. Improvement of the indenter tip shapes

As discussed in chapter 3, one of the important features in indentation experiments is that the piling-up or the sinking-in normally occurs on the specimen's surface around the contact area, and it depicts the deformation of the indented material at the contact boundary. This behaviour is reported to be strongly related to the plastic properties (Wang et al., 2004; Liu et al., 2005; Pelletier, 2006; Yan et al., 2007). Besides, the residual imprint mapping data of the same material produced by different indenters are not identical. Especially, the degree of the piling-up or the sinking-in may not be the same. Therefore, we may conclude that the residual imprint mapping data, which include the piling-up and the sinking-in, contain some valuable additional information and may be very important for the quantification of the material properties.

In addition, according to the recent investigations (Cheng et al., 2006; Kozhevnikov et al., 2008; Kozhevnikov et al., 2010), the indenters with some arbitrary shapes are useful for the evaluation of the material properties of viscoelastic materials. Moreover, some researchers (Chollacoop et al., 2003; Cao and Lu, 2004; Le, 2009) proposed a new method which uses "dual sharp indenters[2]" to determine the material parameters. This method can be applied to a wide range of materials and it has been proved to be more effective and robust than using single indenter. In (Cheng et al., 2006; Kozhevnikov et al., 2008; Kozhevnikov et al., 2010), the researchers supposed that an indenter with complex geometrical shapes can lead to a complex mechanical response, namely, the distribution of contact pressure which is useful for the determination of the material parameters.

[2] The properties of investigated material are determined by using two sharp indenters with different tip shapes, e.g. Berkovich/Vickers indenter and a conical indenter with the 60° half apex angle or two conical indenters with the half apex angles of 70.3° and 60°.

Therefore, some indenters with special shape tips are designed in this chapter. Hopefully they may improve the identifiability of material parameters because they may produce a residual imprint which will provide us with more plastic information.

In the following parts, the efficiencies of three arbitrary shapes of indenters will be compared to two classical indenters. The investigation is carried out by applying a load on the indenters in HEPPERDANG code (Rauchs, 2009). All indenters are modelled as flexible bodies which have a long shaft. Nine nodes quadratic elements with displacement degrees of freedom are used. The classical indenters are a sphere with the radius of 1.25 *mm* and a cone with the half apex angle of 70.3°, see Fig. 4. 9. The geometries of the arbitrary shape indenters can be seen in Fig. 4. 10. The arbitrary shape indenters 1 and 2 are modelled by 3 arcs with different radii.

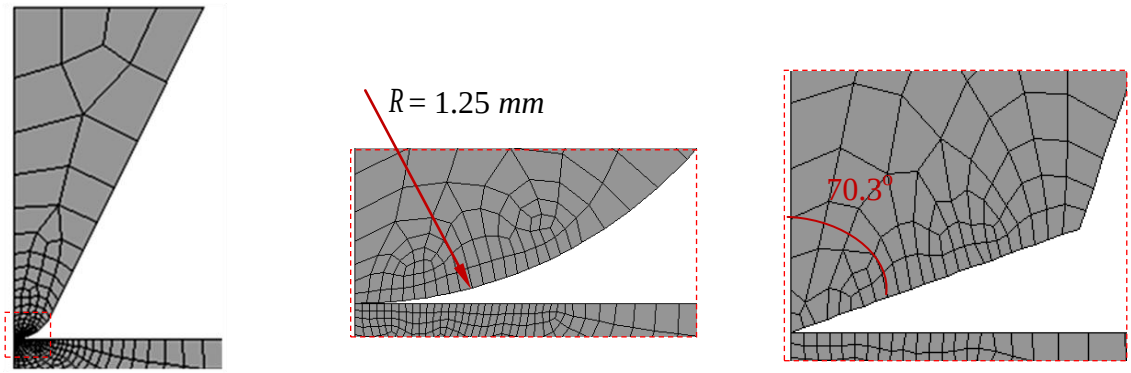

(a) Overall shapes of the indenters (b) Spherical indenter (c) Conical indenter

Fig. 4. 9. The geometries of the spherical and the conical indenters which were used.

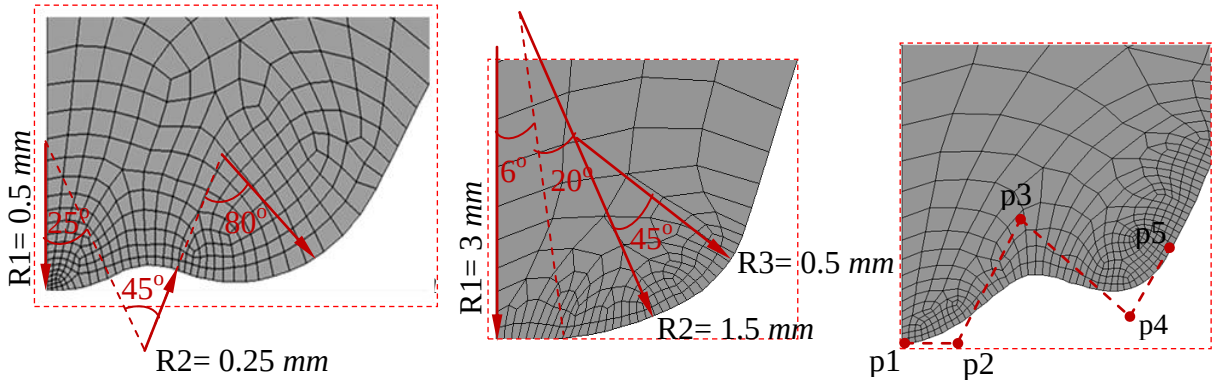

(a) Arbitrary shape indenter 1 (b) Arbitrary shape indenter 2 (c) Arbitrary shape indenter 3

Fig. 4. 10. The geometries of the arbitrary shape indenters.

The profile of the arbitrary shape indenter 1 contains two convex arcs with the radius of 0.5 *mm* and one concave arc with the radius of 0.25 *mm*. It is like using two spherical indenters simultaneously and more complex mechanical response will be produced. The produced imprint is expected to have more information than the one produced by a single spherical indenter.

For the arbitrary shape indenter 2, its profile is convex. The arc 1 in the centre with a large radius is expected to produce more material flow when it penetrates into the specimen. The arc 3 in the periphery with a small radius lets the material easily deforms up.

The profile of the arbitrary shape indenter 3 is similar to the profile of the arbitrary shape indenter 1. However, it is modelled by smooth NURBS curves which let us design an indenter with a complex geometrical shape. It contains two convex sections and one concave section. The convex section in the periphery is higher than the convex section in the centre. When the indenter is penetrating into the specimen, the material gradually contacts to the convex section, the concave section and the convex section. Thus, the material surface around the indenter will deform up or deform down. The imprint mapping may contain additional information to improve material parameters.

The details of NURBS curve can be seen in the work (Rogers, 2001). The degree of the NURBS curve is 3 and 5 control points are defined to describe the shape of the NURBS curve. The positions of the control points and the corresponding weights are listed in Table. 4. 5. Moreover, nine knot vectors are set as 0, 0, 0, 0, 0.5, 1, 1, 1, 1.

Table. 4. 5. Control points and weights.

Control point	Position (x, y) (mm, mm)	weight
p1	0,15	1.0
p2	0.125, 14.99875	0.7
p3	0.375, 15.375	1.0
p4	0.75, 15.0125	1.0
P5	1.125, 15.625	1.0

4.2.1. Illustrations

Since most of the investigations in this chapter are based on numerical simulations, the accuracy of the simulated result strongly depends on the finite element model that was used. Particularly, for the arbitrary shape indenters, the exact descriptions of the residual imprint mappings highly rely on the number of the contact nodes under the indenters. For this reason, three finite element models are tested with different element densities to study the accuracy of simulated results. Every finite element model is designed with a total 15 *mm* radius and 15 *mm* height. A finer

mesh is near the contact region and a gradually coarser mesh is further from the contact region – see the entire finite element mesh in Fig. 4. 11(a). Model 1 is designed with 469 nine-noded quadrilateral elements and about 21 contacted nodes in the contact region at the maximum load, see Fig. 4. 11(b). Model 2 includes 544 nine-noded quadrilateral elements and about 58 contacted nodes are in the contact region at the maximum load, see Fig. 4. 11(c). Model 3 includes 5599 nine-noded quadrilateral elements and there are about 290 contacted nodes at maximum load, see Fig. 4. 11(d).

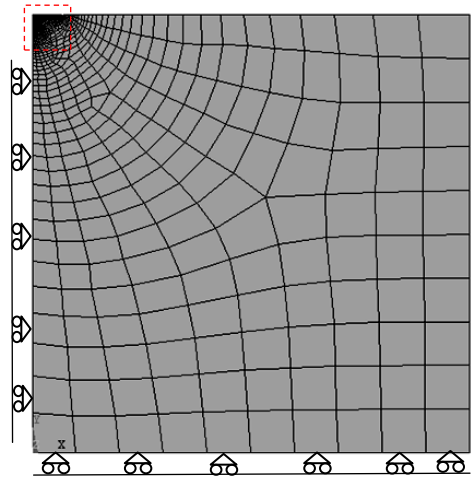

(a) Entire finite element mesh and boundary conditions

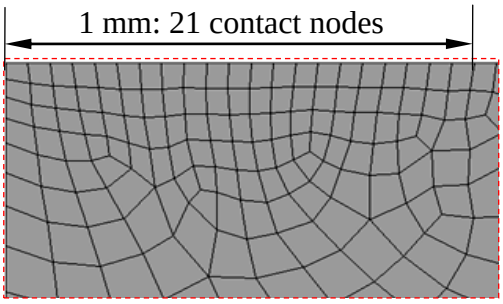

(b) Model 1: 21 contact nodes

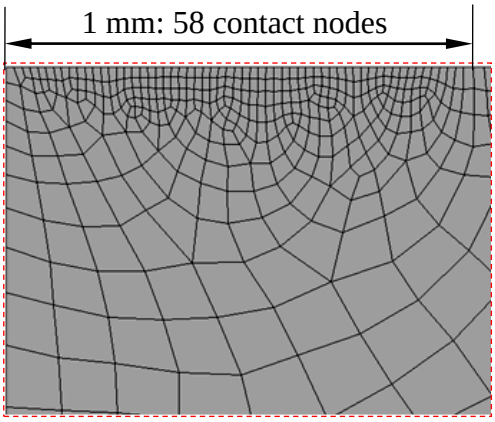

(c) Model 2: 58 contact nodes

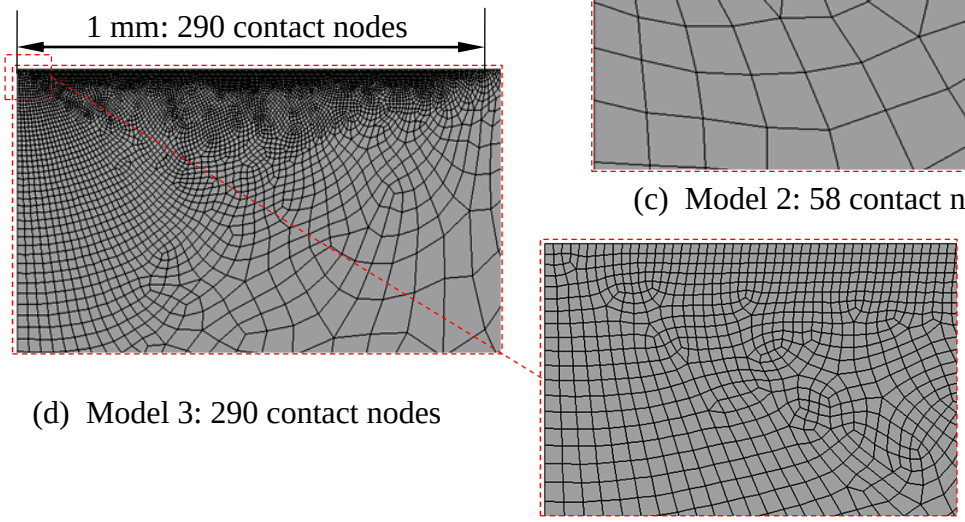

(d) Model 3: 290 contact nodes

Fig. 4. 11. Finite element models with different element densities in the contact region.

In the following part, all investigations are carried out in HEPPERDANG code. The loads applied on the indenters are set to produce a same contact area, namely, let the radii of the contact areas equal 1.0 mm.

4.2.1.1. Mechanical responses obtained by coarse model and fine model

The $P-h$ curves and the corresponding residual imprints obtained by the finite element models with different element densities are compared in Fig. 4. 12. It is obvious that many humps are present on the $P-h$ curves obtained by the model 1 which has a coarse mesh. This occurs because of the fact that the nodes in contact are not sufficient to obtain a precise and continuous result. Particularly, for the arbitrary shape indenters 1 and 2, the maximum penetration depths obtained by the coarse model are normally a little larger than the ones obtained by the models with finer meshes.

We can also note that the imprint data obtained by the model 1 for the arbitrary shape indenters 1 and 3 are not smooth enough. That is due to the fact that the few nodes located in the contact region cannot exactly describe the profiles of the indenters which have complex geometrical shapes. Particularly, at the intergraded parts[3] of the indenters and at $r^I = 1.0\,mm$, where the piling-up or the sinking-in occur, the coarse model with a small number of elements cannot provide a completely precise residual imprint. In the right figures of Fig. 4. 12(a) and (c), the continuous lines obtained from the model 1 are not smooth enough at $r^I = 1.0\,mm$. The imprint data are thus not fully consistent with the profiles of the indenters. In the meantime, it is clear that the residual imprint data obtained by the fine mesh models with a large number of elements are improved in order to have a more accurate description of the profiles of the indenters since more nodes are in contact. For the indenter 2 – see Fig. 4. 12(b) – since its geometrical shape is relatively simple, even the coarse model provides good computed results.

The corresponding computing times can be seen in Table. 4. 6: the model 3 costs much computing time compared to the models 1 and 2 regardless of any indenter. Therefore, in order to improve the efficiency of computation, the model 2 shall be used in the following studies. Indeed, given that it contains about 58 contact nodes at maximum loading. Model 2 can provide an almost identical computation accuracy compared to the model 3 which has about 290 contacted nodes at maximum loading.

[3] Intergraded part: the transitional part is between convex and concave sections on the profile of indenter.

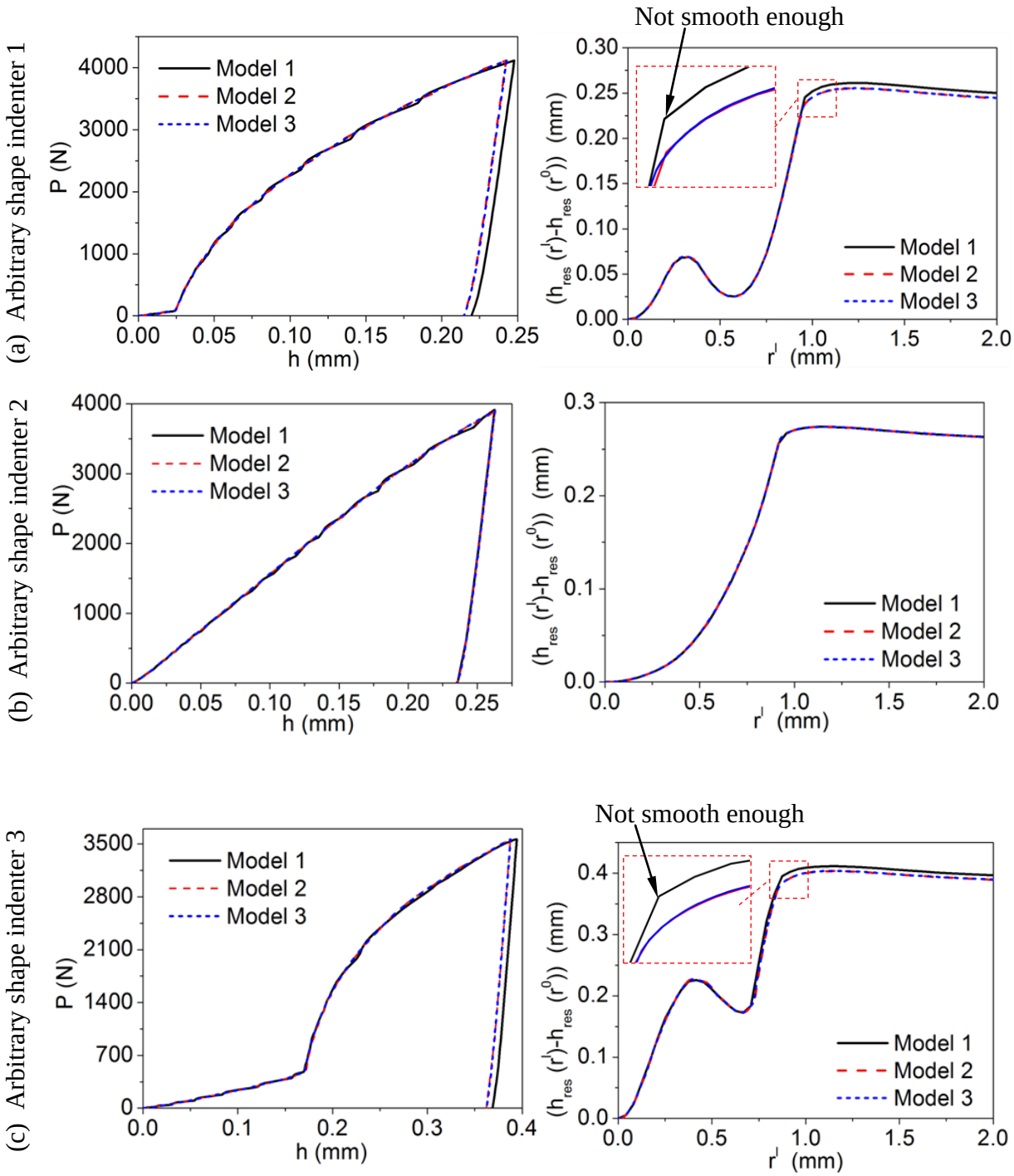

Fig. 4. 12. The $P-h$ curves (Figures on the left) and the corresponding residual imprints (Figures on the right) obtained by the models with different meshes.

Table. 4. 6. Computing time (hour:minute:second).

	Model 1	Model 2	Model 3
Arbitrary shape indenter 1	0:43:39	1:32:15	11:41:48
Arbitrary shape indenter 2	0:20:27	0:59:24	12:07:55
Arbitrary shape indenter 3	0:54:20	1:48:07	12:11:31

4.2.1.2. Comparison of parameter correlations

Table. 4. 7. Parameter correlations: the upper triangle for model 2; the lower triangle for model 3.

	Sphere					Cone				
	E	υ	σ_y^0	Q	ξ	E	υ	σ_y^0	Q	ξ
E	1	0.96	0.90	0.86	0.88	1	0.95	0.91	0.87	0.88
υ	0.94	1	0.97	0.94	0.96	0.94	1	0.98	0.94	0.96
σ_y^0	0.88	0.97	1	1.00	1.00	0.91	0.99	1	0.99	0.99
Q	0.85	0.96	1.00	1	1.00	0.89	0.97	0.99	1	1.00
ξ	0.87	0.97	1.00	1.00	1	0.90	0.98	1.00	1.00	1

	Arbitrary shape indenter 1					Arbitrary shape indenter 2				
	E	υ	σ_y^0	Q	ξ	E	υ	σ_y^0	Q	ξ
E	1	0.97	0.91	0.87	0.88	1	0.97	0.88	0.83	0.85
υ	0.97	1	0.95	0.92	0.93	0.97	1	0.94	0.89	0.91
σ_y^0	0.90	0.95	1	1.00	1.00	0.92	0.98	1	0.99	1.00
Q	0.87	0.92	1.00	1	1.00	0.89	0.97	1.00	1	1.00
ξ	0.88	0.93	1.00	1.00	1	0.90	0.97	1.00	1.00	1

	Arbitrary shape indenter 3				
	E	υ	σ_y^0	Q	ξ
E	1	0.97	0.94	0.92	0.93
υ	0.99	1	0.99	0.97	0.98
σ_y^0	0.96	0.99	1	1.00	1.00
Q	0.94	0.98	1.00	1	1.00
ξ	0.95	0.98	1.00	1.00	1

The parameter correlations obtained by the aforementioned model 2, which contains about 58 nodes in contact at the maximum load, and the model 3, which has about 290 nodes in contact at

the maximum load, are compared in Table. 4. 7. The accurate description of the computed imprint data highly depends on the number of nodes in contact. Herein the objective function is defined to take into account the imprint data.

In Table. 4. 7, the data in the upper triangle are obtained by the model 2 and the data in the lower triangle are calculated by the model 3. It is clear that the parameter correlations obtained by the models 2 and 3 do not have significant differences: all the differences are lower than 0.08. Therefore, the model 2 has again proved to be eligible to be used for the assessment of the parameter correlations. Moreover, the accuracy of the corresponding results is not much affected by the number of elements of the finite element model.

4.3. Loading history

According to the investigations on uniaxial tension and compression tests for the identification of the parameters of elasto-plastic materials (Mahnken and Stein, 1996b; Dettmer and Reese, 2004), the researchers suggested that the compressive cycle is necessary to determine the isotropic and kinematic hardening parameters. In the absence of a compressive cycle with reverse plastic flow, it is not possible to separate the kinematic hardening from the isotropic hardening. However, the previous work (Huber and Tsakmakis, 1998) shows that the indentation test can be used to evaluate the effects of kinematic hardening in the material response. In indentation measurements, the reloading cycle is proved to be critical to identify the effects of kinematic hardening in the material response. However, this identification may highly rely upon the measurement of the opening of the hysteresis loop produced in the load-displacement diagram by considering the unloading and the reloading curves. Afterwards, some authors (Huber and Tsakmakis, 1999b; Huber and Tsakmakis, 1999a) successfully extracted the kinematic hardening parameters from the hysteresis loop, which consists of the unloading and the reloading curves, by using artificial neural networks. Therefore, it is well known that the reloading cycle in indentation tests is necessary for identifying the kinematic hardening of the indented material. On the basis of the published papers, two forms of unloading and reloading cycles are frequently seen when the load reaches the maximum, namely, the partial unloading followed by a reloading (Oliver and Pharr, 1992) and the completely unloading and then reloading (Huber and Tsakmakis, 1999a). In this thesis, in order to produce a large size for the hysteresis loop, the second form of unloading-reloading cycle is implemented.

In addition, for the identification of the viscosity of the material, a holding cycle is often used in the indentation process (Huber and Tyulyukovskiy, 2004; Cheng et al., 2006; Vandamme and Ulm, 2006; Rauchs, 2008). The examples in the investigations (Huber and Tyulyukovskiy, 2004) demonstrate that the holding cycle is very helpful to determine the viscous parameters and that the accuracy of the identification can be significantly increased with the holding period.

For this reason, the loading histories with multi-loading, holding and unloading cycles are studied for the materials with different mechanical behaviours. In this thesis, for the multi-load cases, the peak load in the first loading cycle equals 50% of the peak in the third loading cycle and the peak load in the second loading cycle is 75% of the peak load in the third loading cycle.

4.3.1. Illustrations

Two materials, listed in Table. 4. 8, have been chosen for illustrations. Material 1 is an elasto-plastic material with isotropic hardening. The kinematic hardening evolution of Material 2 is described by the Armstrong-Frederick law with the non-linear kinematic hardening parameters H_{kin} and H_{nl}. The plastic behaviours of both materials are also approximated by the Voce-type hardening law.

Table. 4. 8. Materials used for illustrations.

	$E\,(GPa)$	υ	$\sigma_y^0\,(MPa)$	$Q\,(MPa)$	ξ	$H_{kin}\,(MPa)$	H_{nl}
Material 1	74.5	0.3	295	350	5	×	×
Material 2	74.5	0.3	295	350	5	1000	5

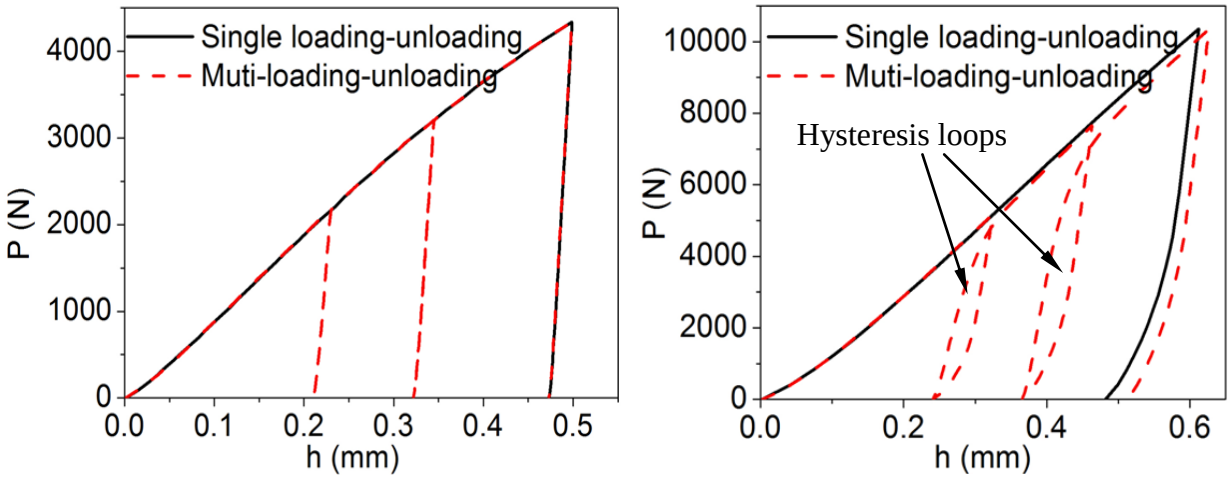

(a) Material 1 (b) Material 2

Fig. 4. 13. The $P-h$ curves for Materials 1 and 2.

The finite element model that was used in the spherical indentation is similar to the model 2 shown in Fig. 4. 11. The radius of the spherical indenter is 1.25 *mm* and the model of the

specimen is designed with 15 *mm* radius and 15 *mm* height. At least 58 nodes are in contact at the maximum load for every case.

Table. 4. 9. Cosine Hessian matrices of material 1: the upper triangle for single loading-unloading cycle; the lower triangle for the multi-loading-unloading cycles.

	E	υ	σ_y^0	Q	ξ
E	1	0.96	0.90	0.86	0.88
υ	0.95	1	0.97	0.94	0.96
σ_y^0	0.89	0.95	1	1.00	1.00
Q	0.84	0.92	0.99	1	1.00
ξ	0.87	0.94	1.00	1.00	1

Table. 4. 10. Cosine Hessian matrices of material 2: the upper triangle for the single loading-unloading cycle; the lower triangle for the multi-loading-unloading cycles.

	E	υ	σ_y^0	Q	ξ	H_{kin}	H_{nl}
E	1	0.96	0.86	0.89	0.90	0.72	0.79
υ	0.95	1	0.97	0.97	0.98	0.87	0.92
σ_y^0	0.87	0.98	1	0.98	0.99	0.97	0.99
Q	0.87	0.96	0.98	1	1.00	0.94	0.97
ξ	0.88	0.97	0.99	1.00	1	0.94	0.97
H_{kh}	0.77	0.92	0.98	0.97	0.97	1	0.99
H_{kb}	0.82	0.95	0.99	0.98	0.98	1.00	1

The corresponding $P-h$ curves obtained by the single loading-unloading cycle and the multi-loading-unloading cycles are compared in Fig. 4. 13. For Material 1, the loading and unloading curves in the third unloading cycle, obtained under the multi-loading-unloading cycles, are of course exactly identical compared to the ones obtained under the single loading-unloading cycle, since Material 1 does not have a kinematic hardening behaviour.

However, for Material 2 – see Fig. 4. 13(b). The load-displacement curves obtained in both the loading cases are significantly different due to the effects of kinematic hardening parameters. It is clear that the hysteresis loops appear in the second and third loading cycles.

The parameter correlations obtained by both loading histories can be seen in Table. 4. 9 and Table. 4. 10, respectively. The imprint data are taken into account into the objective function. The data in the upper triangle are obtained under the loading-unloading cycles and the data in the lower triangle are calculated on the basis of the multi-loading-unloading cycles. For Material 1, it can be seen that the parameters correlations decrease a little under the multi-loading cycles.

The amount of the decrease is about 0.01 for the couplings of E with other parameters and 0.02 for the couplings of υ with other parameters. The couplings among the plastic parameter do not have any changes. It is the same for Material 2: all the material parameter correlations are not obviously reduced by the introduction of the multi-loading cycles.

CHAPTER 5
ASSESSMENT OF THE EFFECT OF INDENTER TIP GEOMETRY IN MATERIAL PARAMETER IDENTIFICATION

Overview

This chapter examines the effects of the indenter tip geometries on the identification of material parameters on the basis of several representative materials, namely, the materials with elasto-plastic and elasto-viscoplastic constitutive laws. It also assesses the sensitivities of the material parameters towards the indenter tip geometries.

Contents

5.1. Elasto-plastic materials

Three elasto-plastic materials, listed in Table. 5. 1, are used for illustration. The isotropic hardening is approximated by Voce-type hardening law. The investigations (Balint et al., 2006; Pelletier, 2006; Yan et al., 2007) demonstrated that the piling-up and the sinking-in are mainly affected by the ratio of Young's modulus to the initial yield stress. When the material has a small ratio of E/σ_y^0, piling-up easily occurs. On the other hand, sinking-in often appears when the ratio E/σ_y^0 is large. For this reason, the ratio of Young's modulus and the initial yield stress is designed to be equal to 25, 252.54 and 1000, for the different material models. Here the contact friction is ignored and the friction coefficient is set as zero.

The finite element model which is used is the model 2, which is shown in the Fig. 4. 11, because this model has already proved to ensure the accuracy of computation and does not cost too much computing time. It is designed with 15 *mm* radius and 15 *mm* height and about 58 contact nodes in the contact region at maximum load. The radial and normal displacements are fixed at the central and bottom lines as boundary conditions. The maximum loads applied on different indenters are set to let the indenters produce a nearly same contact area, namely, let the radii of the contact areas equal 1.0 mm. Thus, piling-up or sinking-in will occur about at $r^l = 1.0\ mm$.

Table. 5. 1. Material properties of elasto-plastic materials.

Material	$E\,(GPa)$	$\sigma_y^0\,(MPa)$	υ	$Q\,(MPa)$	ξ	E/σ_y^0
1	50	2000	0.3	200	5.0	25
2	74.5	295	0.3	200	5.0	252.54
3	200	200	0.3	200	5.0	1000

Given that, the mechanical behaviours of elasto-plastic materials are time-independent, the single loading-unloading cycle without the holding period is applied herein. When the load reaches the maximum, the unloading starts immediately after.

The corresponding cosine matrices of the Hessian matrices identified by different indenters are listed in Table. 5. 2 to Table. 5. 4. The data in the upper triangles are obtained from an objective function including imprint data. The data in the lower triangles are obtained from the objective function which does not include imprint data.

The parameter correlations of the material 1 with a smaller ratio of E/σ_y^0 are shown in Table. 5. 2. It can be seen that most correlation parameters obtained by the spherical indenter are above 0.96, except the correlations of Young's modulus with the plastic material parameters σ_y^0, Q and ξ when the imprint data are taken into account in the objective function (see the data in the lower triangle). Especially, for the plastic material parameters σ_y^0, Q and ξ, all the correlation

parameters are equal to 1.0. Besides, the Poisson's ratio υ is also strongly coupled with the plastic material parameters.

Table. 5. 2. The cosine matrices of Hessian matrices for material 1 ($E/\sigma_y^0 = 25$): upper triangle with imprint data, lower triangle without imprint data.

	Sphere					Cone				
	E	υ	σ_y^0	Q	ξ	E	υ	σ_y^0	Q	ξ
E	1	0.86	0.77	0.74	0.75	1	0.71	0.50	0.43	0.46
υ	0.95	1	0.98	0.96	0.97	0.92	1	0.96	0.93	0.94
σ_y^0	0.88	0.98	1	1.00	1.00	0.80	0.97	1	0.99	1.00
Q	0.85	0.97	1.00	1	1.00	0.75	0.95	1.00	1	1.00
ξ	0.87	0.98	1.00	1.00	1	0.77	0.96	1.00	1.00	1

	Arbitrary shape indenter 1					Arbitrary shape indenter 2				
	E	υ	σ_y^0	Q	ξ	E	υ	σ_y^0	Q	ξ
E	1	0.80	0.63	0.63	0.63	1	0.76	0.57	0.54	0.54
υ	0.93	1	0.97	0.96	0.96	0.93	1	0.97	0.95	0.95
σ_y^0	0.82	0.97	1	1.00	1.00	0.81	0.97	1	1.00	1.00
Q	0.80	0.96	1.00	1	1.00	0.77	0.95	1.00	1	1.00
ξ	0.80	0.96	1.00	1.00	1	0.78	0.96	1.00	1.00	1

	Arbitrary shape indenter 3				
	E	υ	σ_y^0	Q	ξ
E	1	0.90	0.83	0.82	0.82
υ	0.95	1	0.99	0.98	0.98
σ_y^0	0.90	0.99	1	1.00	1.00
Q	0.89	0.98	1.00	1	1.00
ξ	0.89	0.98	1.00	1.00	1

When the objective function takes into account the imprint data, it is clear that the correlations of the elastic parameters with the plastic material parameters are reduced although some reductions are not significant. For example, the correlations of E with other material parameters decrease obviously, but the correlations of υ with the plastic material parameters σ_y^0, Q and ξ only reduce by 0.01. Besides, the reduction between the elastic parameters E and υ is visible. However, the three plastic material parameters σ_y^0, Q and ξ are still strongly coupled

between each other. The correlation parameters are always close to 1.0 regardless of the effect of the imprint data.

Similar phenomena appear in the cosine matrix of the Hessian matrix obtained for the conical indenter. When the imprint data are not counted, all the parameter correlations are high. When the objective function takes into account the imprint data, the parameter correlations decrease. Particularly, for Young's modulus, it is significantly decoupled from the other material parameters due to the fact that the objective function takes into account the imprint data. However, the plastic material parameters are always strongly coupled with each other and the correlations of υ with the plastic material parameter do not reduce significantly.

The parameter correlations obtained by the three arbitrary shape indenters are similar to the ones obtained by the classical indenters. Through the introduction of the imprint data in the objective function, most the parameter correlations are reduced. Especially, the correlations of Young's modulus with the other material parameters decrease obviously. The couplings among the other material parameters do not reduce significantly. The comparison shows that the conical indenter and the arbitrary shape indenter 2 perform better than the others.

The parameter correlations of the material 2 can be seen in Table. 5. 3. All the material parameters are strongly coupled when the imprint data are not taken into account in the objective function. For instance, when we examine the data obtained by the spherical indenter, we notice that all the parameter correlations in the lower triangle are above 0.87. Unfortunately, the parameter correlations do not reduce significantly although the objective function takes into account the imprint data. Even the correlations of E with other material parameters do not reduce significantly (see the data in the upper triangle).

The same phenomena also appear in the cosine matrices obtained by the other indenters. That is due to the fact that the material 2 has a ratio of $E/\sigma_y^0 = 252.54$ hardly larger compared to material 1. The deformations of the specimen around the indenters are not sensitive to the geometries of the indenter tips and cannot provide additional information for the decrease of the parameter correlations.

Table. 5. 3. The cosine matrices of Hessian matrices for material 2 ($E/\sigma_y^0 = 252.54$): upper triangle with imprint data, lower triangle without imprint data.

	Sphere					Cone				
	E	υ	σ_y^0	Q	ξ	E	υ	σ_y^0	Q	ξ
E	1	0.95	0.85	0.81	0.83	1	0.95	0.91	0.85	0.87
υ	0.98	1	0.94	0.91	0.93	0.99	1	0.98	0.92	0.94
σ_y^0	0.91	0.95	1	1.00	1.00	0.96	0.99	1	0.98	0.99
Q	0.87	0.92	1.00	1	1.00	0.94	0.98	0.99	1	1.00
ξ	0.90	0.94	1.00	1.00	1	0.95	0.98	1.00	1.00	1

	Arbitrary shape indenter 1					Arbitrary shape indenter 2				
	E	υ	σ_y^0	Q	ξ	E	υ	σ_y^0	Q	ξ
E	1	0.97	0.84	0.79	0.80	1	0.96	0.86	0.82	0.83
υ	0.99	1	0.92	0.88	0.89	0.99	1	0.94	0.91	0.92
σ_y^0	0.89	0.93	1	1.00	1.00	0.89	0.94	1	1.00	1.00
Q	0.84	0.88	0.99	1	1.00	0.84	0.90	0.99	1	1.00
ξ	0.86	0.90	1.00	1.00	1	0.87	0.92	1.00	1.00	1

	Arbitrary shape indenter 3				
	E	υ	σ_y^0	Q	ξ
E	1	0.99	0.96	0.94	0.95
υ	0.99	1	0.98	0.97	0.98
σ_y^0	0.96	0.98	1	1.00	1.00
Q	0.94	0.97	1.00	1	1.00
ξ	0.95	0.97	1.00	1.00	1

The parameter correlations of the material 3 can be seen in Table. 5. 4. The parameter correlations obtained by the spherical indenter are high when the imprint data are not taken into account. They do not reduce significantly due to the effects of the imprint data. For instance, the correlations of E with the other material parameters are above 0.88 when the objective function does not include the imprint data. When the imprint data are counted in the objective function, the correlations are only reduced by 0.02.

It is noted that all the material parameters are strongly coupled when the material 3 is evaluated by the conical indenter. All the parameter correlations are above 0.98 when the imprint data are absent. However, the imprint data do not provide a large contribution to the decrease of the

couplings. The correlations of the elastic parameters with the plastic parameters reduce slightly and the correlation parameters among the plastic parameters are always 1.0.

Table. 5. 4. The cosine matrices of Hessian matrices for material 3 ($E/\sigma_y^0 = 1000$): upper triangle with imprint data, lower triangle without imprint data.

	Sphere					Cone				
	E	υ	σ_y^0	Q	ξ	E	υ	σ_y^0	Q	ξ
E	1	0.96	0.89	0.86	0.88	1	0.98	0.96	0.94	0.95
υ	0.98	1	0.97	0.95	0.96	0.99	1	0.99	0.98	0.98
σ_y^0	0.92	0.96	1	1.00	1.00	0.98	1.00	1	1.00	1.00
Q	0.88	0.93	1.00	1	1.00	0.98	1.00	1.00	1	1.00
ξ	0.90	0.95	1.00	1.00	1	0.98	1.00	1.00	1.00	1

	Arbitrary shape indenter 1					Arbitrary shape indenter 2				
	E	υ	σ_y^0	Q	ξ	E	υ	σ_y^0	Q	ξ
E	1	0.98	0.93	0.90	0.91	1	0.98	0.91	0.89	0.90
υ	0.99	1	0.97	0.95	0.96	0.99	1	0.97	0.95	0.96
σ_y^0	0.94	0.96	1	1.00	1.00	0.92	0.95	1	1.00	1.00
Q	0.91	0.93	1.00	1	1.00	0.88	0.92	1.00	1	1.00
ξ	0.92	0.95	1.00	1.00	1	0.90	0.93	1.00	1.00	1

	Arbitrary shape indenter 3				
	E	υ	σ_y^0	Q	ξ
E	1	0.97	0.93	0.89	0.90
υ	0.98	1	0.98	0.97	0.97
σ_y^0	0.93	0.98	1	1.00	1.00
Q	0.89	0.96	0.99	1	1.00
ξ	0.90	0.97	1.00	1.00	1

This is also the case of the parameter correlations obtained by the other arbitrary shape indenters. All the parameter correlations are strongly coupled and they are larger than 0.88 even if the imprint data are counted in the objective function.

Compared to the materials 1 and 2, the material 3 has the largest ratio of $E/\sigma_y^0 = 1000$, and its material parameters are even less sensitive to the geometries of the indenter tips.

5.1.1. Conclusions

From the above tables, it is can be seen that E is the most easiest to be separated from the other material parameters and the plastic material parameters of σ_y^0, Q and ξ are the most difficult to be distinguished from each other, because they are always strongly coupled among themselves regardless of the effect of the imprint data and the shape geometries of the indenter tips.

For the material 1 with a small ratio of E/σ_y^0, where the piling-up occurs. The parameter correlations decrease obviously under the effect of the imprint data. Particularly, Young's modulus is significantly decoupled from the other material parameters. Here, it is noted that the conical indenter and the arbitrary shape indenter 2 perform better in the determination of the material parameters because the parameter correlations assessed by such indenters are normally lower than the ones assessed by the other indenters.

However, for the materials 2 and 3 which have a large ratio of E/σ_y^0, the material parameters are not sensitive to the shape geometries of the indenter tips and the imprint data do not seem to provide a large contribution to the decrease of the parameter correlation. For this kind of materials, it can be seen that the spherical indenter performs a little better than the other indenters.

5.2. Elasto-viscoplastic material

An elasto-viscoplastic material used in the work of (Rauchs, 2008) is chosen for the investigation in the present part. The material properties of this material are given in Table. 5. 5. The plastic behaviour is described by Voce-type hardening law (see Eq. (4.1)) and the non-linear kinematic hardening is approximated by Armstrong-Frederick law with the non-linear kinematic hardening parameters H_{kin} and H_{nl} (see Eq. (4.2)). The viscosity is described according to (Rauchs, 2008) with the viscosity η and the viscosity exponent m,

$$\sigma_{visco} = \sqrt{\frac{2}{3}}\left(\dot{s}\eta\right)^{\frac{1}{m}}. \tag{5.1}$$

Table. 5. 5. The properties of elasto-viscoplastic material.

E (GPa)	σ_y^0 (MPa)	υ	Q (MPa)	ξ	H_{kin} (MPa)	H_{nl}	η $(MPa/\mathrm{s}^{1/\mathrm{m}})$	m
200	400	0.3	200	10	100	5	1000	2

The finite element model which is used is similar to the one used in the previous part. The 2D axisymmetric model is designed with 15 *mm* radius and 15 *mm* height. At maximum load, there are 58 nodes in contact. The radial and normal displacements are fixed at the central and bottom lines, respectively, as boundary conditions.

The material parameter correlations assessed by different indenters with different load histories are shown in Table. 5. 6. This table is similar to the ones shown in the foregoing parts. The data in the upper triangles are obtained from an objective function including the imprint data. The data in the lower triangles are obtained from the objective function which does not include the imprint data.

Table. 5. 6. The cosine matrices of the Hessian matrices obtained by the loading-unloading cycle: upper triangle with imprint data, lower triangle without imprint data.

Spherical indenter									
	E	υ	σ_y^0	Q	ξ	H_{kin}	H_{nl}	η	m
E	1	0.97	0.88	0.85	0.87	0.83	0.85	0.87	-0.87
υ	0.98	1	0.95	0.92	0.94	0.91	0.93	0.94	-0.93
σ_y^0	0.93	0.97	1	1.00	1.00	0.99	1.00	1.00	-0.99
Q	0.91	0.95	1.00	1	1.00	1.00	1.00	1.00	-1.00
ξ	0.93	0.97	1.00	1.00	1	0.99	1.00	1.00	-0.99
H_{kin}	0.89	0.94	1.00	1.00	0.99	1	1.00	0.99	-0.99
H_{nl}	0.92	0.96	1.00	1.00	1.00	1.00	1	1.00	-1.00
η	0.94	0.97	1.00	0.99	1.00	0.99	1.00	1	-1.00
m	-0.94	-0.97	-1.00	-0.99	-1.00	-0.99	-0.99	-1.00	1

Conical indenter									
	E	υ	σ_y^0	Q	ξ	H_{kin}	H_{nl}	η	m
E	1	0.97	0.93	0.88	0.90	0.84	0.87	0.90	-0.84
υ	0.99	1	0.97	0.93	0.95	0.89	0.92	0.93	-0.87
σ_y^0	0.97	1.00	1	0.99	1.00	0.97	0.98	0.98	-0.92
Q	0.95	0.99	1.00	1	1.00	1.00	1.00	0.98	-0.93
ξ	0.96	0.99	1.00	1.00	1	0.99	1.00	0.98	-0.93
H_{kin}	0.94	0.98	1.00	1.00	1.00	1	1.00	0.97	-0.93
H_{nl}	0.95	0.99	1.00	1.00	1.00	1.00	1	0.98	-0.93
η	0.95	0.97	0.97	0.97	0.97	0.97	0.97	1	-0.98
m	-0.88	-0.89	-0.89	-0.88	-0.89	-0.88	-0.89	-0.97	1

Arbitrary shape indenter 1									
	E	υ	σ_y^0	Q	ξ	H_{kin}	H_{nl}	η	m
E	1	0.99	0.87	0.84	0.86	0.82	0.84	0.85	-0.84
υ	0.99	1	0.90	0.87	0.89	0.86	0.87	0.88	-0.87
σ_y^0	0.92	0.94	1	1.00	1.00	0.99	1.00	1.00	-1.00
Q	0.89	0.91	1.00	1	1.00	1.00	1.00	1.00	-1.00
ξ	0.91	0.93	1.00	1.00	1	1.00	1.00	1.00	-1.00
H_{kin}	0.87	0.90	0.99	1.00	1.00	1	1.00	1.00	-1.00
H_{nl}	0.89	0.91	1.00	1.00	1.00	1.00	1	1.00	-1.00
η	0.90	0.92	1.00	1.00	1.00	1.00	1.00	1	-1.00
m	-0.89	-0.92	-1.00	-1.00	-1.00	-1.00	-1.00	-1.00	1

Arbitrary shape indenter 2									
	E	υ	σ_y^0	Q	ξ	H_{kin}	H_{nl}	η	m
E	1	0.98	0.87	0.83	0.86	0.82	0.83	0.84	-0.83
υ	0.99	1	0.92	0.89	0.91	0.88	0.89	0.90	-0.89
σ_y^0	0.91	0.94	1	1.00	1.00	0.99	1.00	1.00	-1.00
Q	0.87	0.91	1.00	1	1.00	1.00	1.00	1.00	-1.00
ξ	0.90	0.94	1.00	1.00	1	1.00	1.00	1.00	-1.00
H_{kin}	0.86	0.90	0.99	1.00	0.99	1	1.00	1.00	-1.00
H_{nl}	0.88	0.92	1.00	1.00	1.00	1.00	1	1.00	-1.00
η	0.88	0.92	1.00	1.00	1.00	1.00	1.00	1	-1.00
m	-0.87	-0.91	-1.00	-1.00	-1.00	-1.00	-1.00	-1.00	1

Arbitrary shape indenter 3									
	E	υ	σ_y^0	Q	ξ	H_{kin}	H_{nl}	η	m
E	1	0.99	0.94	0.92	0.94	0.91	0.93	0.93	-0.92
υ	0.99	1	0.96	0.95	0.96	0.94	0.95	0.95	-0.95
σ_y^0	0.95	0.98	1	1.00	1.00	1.00	1.00	1.00	-1.00
Q	0.94	0.96	1.00	1	1.00	1.00	1.00	1.00	-1.00
ξ	0.96	0.98	1.00	1.00	1	1.00	1.00	1.00	-1.00
H_{kin}	0.93	0.96	1.00	1.00	1.00	1	1.00	1.00	-1.00
H_{nl}	0.95	0.97	1.00	1.00	1.00	1.00	1	1.00	-1.00
η	0.94	0.97	1.00	1.00	1.00	1.00	1.00	1	-1.00
m	-0.94	-0.96	-1.00	-1.00	-1.00	-1.00	-1.00	-1.00	1

The material parameter correlations obtained under the loading-unloading cycle are shown in Table. 5. 6. From the data obtained by the spherical indenter, it can be seen that all the material parameters are strongly coupled when the objective function does not take into account the imprint data (see the data in the lower triangle). The parameter correlations are larger than 0.89 and some of them equal or nearly equal 1.0. Once the imprint data are taken into account in the objective function, the parameter correlations decrease. Particularly, the correlations of the elastic parameters with the plastic and viscous parameters decrease although the reductions are not very significant. However, for the other material parameters, the correlations between themselves do not reduce significantly.

Similar phenomena appear in the parameter correlations obtained for the other indenters. If the imprint data are not taken into account in the objective function, all the material parameters are strongly coupled. However, it is noted that all the parameter correlations are always very high although the imprint data are introduced in the objective function when the parameter correlations are evaluated by arbitrary shape indenter 3. This means that the material parameters are not very sensitive to the tip geometry of the arbitrary shape indenter 3. In addition, it can be seen that the plastic parameters cannot be separated from the viscous parameters and the two blocks of material parameters, plastic and viscous, always remain fully coupled among themselves no matter what indenter is used. This inextricable couplings also exist in elastic material parameters E and υ. The corresponding parameter correlations are normally above 0.97.

Compared to the parameter correlation obtained under the loading-unloading cycle, the correlations of most material parameters obtained by the loading-holding-unloading cycle decrease significantly (see Table. 5. 7). For instance, see the data which are obtained by the spherical indenter. In the lower triangle, although the imprint data are not taken into account in the objective function, the blocks of elastic, plastic and viscous parameters begin to be separated. Once the imprint data are counted in the objective function, the blocks of elastic, plastic and viscous parameters are more easily separated. Especially, the two viscous parameters are obviously almost decoupled from the other parameters. However, in the blocks of elastic, plastic and viscous parameters, the material parameters are strongly coupled with each other.

The similar phenomena can be seen in the results obtained by the other indenters. Particularly for the parameter correlations obtained by the conical indenter (see the data in the upper triangle), the parameter correlations of the viscous parameters with the other material parameters are below 0.26 (they are above 0.84 when they are evaluated using the loading-unloading cycle, see the data evaluated by conical indenter in Table. 5. 6). Besides, the blocks of elastic, plastic and viscous parameters are also obviously separated although the material parameters in the blocks are still coupled. Moreover, when the material parameters are evaluated by the arbitrary shape indenter 3, they are always strongly coupled regardless of the effect of the imprint data.

This means that the material parameters are not sensitive to the shape geometries of the arbitrary shape indenter 3.

Table. 5. 7. The cosine matrices of the Hessian matrices obtained by the loading-holding-unloading cycle: upper triangle with imprint data, lower triangle without imprint data.

Spherical indenter									
	E	υ	σ_y^0	Q	ξ	H_{kin}	H_{nl}	η	m
E	1	0.94	0.72	0.67	0.71	0.65	0.68	0.79	-0.70
υ	0.98	1	0.87	0.83	0.87	0.82	0.84	0.71	-0.60
σ_y^0	0.85	0.91	1	1.00	1.00	0.99	1.00	0.55	-0.43
Q	0.81	0.88	1.00	1	1.00	1.00	1.00	0.52	-0.40
ξ	0.85	0.91	1.00	1.00	1	0.99	1.00	0.55	-0.43
H_{kin}	0.79	0.86	0.99	1.00	0.99	1	1.00	0.50	-0.38
H_{nl}	0.82	0.89	1.00	1.00	1.00	1.00	1	0.53	-0.41
η	0.84	0.79	0.58	0.52	0.58	0.50	0.54	1	-0.99
m	-0.79	-0.73	-0.49	-0.43	-0.49	-0.40	-0.45	-0.99	1

Conical indenter									
	E	υ	σ_y^0	Q	ξ	H_{kin}	H_{nl}	η	m
E	1	0.97	0.92	0.87	0.90	0.82	0.86	0.26	0.11
υ	0.99	1	0.97	0.92	0.94	0.87	0.91	0.13	0.24
σ_y^0	0.97	1.00	1	0.98	1.00	0.96	0.98	0.11	0.26
Q	0.97	0.99	1.00	1	1.00	0.99	1.00	0.12	0.24
ξ	0.97	1.00	1.00	1.00	1	0.98	0.99	0.11	0.25
H_{kin}	0.96	0.99	1.00	1.00	1.00	1	1.00	0.13	0.21
H_{nl}	0.96	0.99	1.00	1.00	1.00	1.00	1	0.13	0.23
η	0.41	0.35	0.31	0.30	0.31	0.30	0.31	1	-0.91
m	-0.09	-0.03	0.00	0.01	0.01	0.00	0.00	-0.93	1

Arbitrary shape indenter 1									
	E	υ	σ_y^0	Q	ξ	H_{kin}	H_{nl}	η	m
E	1	0.98	0.85	0.80	0.83	0.78	0.80	0.64	-0.45
υ	0.99	1	0.89	0.85	0.87	0.83	0.85	0.56	-0.35
σ_y^0	0.91	0.92	1	1.00	1.00	0.99	1.00	0.39	-0.17
Q	0.85	0.87	0.99	1	1.00	1.00	1.00	0.35	-0.13
ξ	0.89	0.91	1.00	1.00	1	1.00	1.00	0.39	-0.16
H_{kin}	0.83	0.85	0.99	1.00	0.99	1	1.00	0.33	-0.11
H_{nl}	0.86	0.88	0.99	1.00	1.00	1.00	1	0.35	-0.13
η	0.74	0.71	0.58	0.50	0.57	0.48	0.52	1	-0.97
m	-0.64	-0.61	-0.45	-0.38	-0.44	-0.35	-0.39	-0.99	1

Arbitrary shape indenter 2									
	E	υ	σ_y^0	Q	ξ	H_{kin}	H_{nl}	η	m
E	1	0.98	0.89	0.86	0.88	0.85	0.86	0.61	-0.32
υ	0.99	1	0.94	0.91	0.93	0.90	0.91	0.54	-0.22
σ_y^0	0.93	0.96	1	1.00	1.00	1.00	1.00	0.44	-0.12
Q	0.91	0.94	1.00	1	1.00	1.00	1.00	0.42	-0.10
ξ	0.93	0.96	1.00	1.00	1	1.00	1.00	0.44	-0.12
H_{kin}	0.89	0.93	1.00	1.00	1.00	1	1.00	0.41	-0.08
H_{nl}	0.91	0.94	1.00	1.00	1.00	1.00	1	0.42	-0.10
η	0.66	0.61	0.49	0.45	0.49	0.43	0.46	1	-0.94
m	-0.45	-0.39	-0.25	-0.21	-0.25	-0.19	-0.22	-0.96	1

Arbitrary shape indenter 3									
	E	υ	σ_y^0	Q	ξ	H_{kin}	H_{nl}	η	m
E	1	0.99	0.93	0.91	0.93	0.91	0.92	0.95	-0.94
υ	0.99	1	0.96	0.94	0.96	0.94	0.95	0.96	-0.95
σ_y^0	0.95	0.97	1	1.00	1.00	1.00	1.00	0.98	-0.98
Q	0.93	0.96	1.00	1	1.00	1.00	1.00	0.98	-0.98
ξ	0.95	0.97	1.00	1.00	1	1.00	1.00	0.98	-0.98
H_{kin}	0.92	0.95	1.00	1.00	1.00	1	1.00	0.97	-0.97
H_{nl}	0.94	0.96	1.00	1.00	1.00	1.00	1	0.98	-0.98
η	0.97	0.98	0.97	0.96	0.97	0.95	0.97	1	-1.00
m	-0.96	-0.97	-0.97	-0.96	-0.97	-0.95	-0.96	-1.00	1

In the third case, a reloading cycle is introduced into the load history. The maximum load in the first loading cycle is 60% of the maximum load in the second loading cycle. The corresponding parameter correlations are shown in Table. 5. 8.

Table. 5. 8. The cosine matrices of the Hessian matrices obtained by the loading-holding-unloading-loading-holding-unloading cycle: upper triangle with imprint data, lower triangle without imprint data.

Spherical indenter									
	E	υ	σ_y^0	Q	ξ	H_{kin}	H_{nl}	η	m
E	1	0.96	0.84	0.79	0.84	0.76	0.80	0.41	-0.18
υ	0.99	1	0.92	0.88	0.92	0.86	0.89	0.29	-0.04
σ_y^0	0.93	0.95	1	0.99	1.00	0.99	1.00	0.21	0.04
Q	0.89	0.92	0.99	1	0.99	1.00	1.00	0.20	0.04
ξ	0.94	0.96	1.00	0.99	1	0.99	1.00	0.23	0.03
H_{kin}	0.87	0.90	0.99	1.00	0.98	1	1.00	0.18	0.06
H_{nl}	0.91	0.93	1.00	1.00	1.00	0.99	1	0.21	0.04
η	0.57	0.53	0.48	0.47	0.51	0.45	0.48	1	-0.97
m	-0.43	-0.39	-0.33	-0.33	-0.36	-0.30	-0.34	-0.99	1

Conical indenter									
	E	υ	σ_y^0	Q	ξ	H_{kin}	H_{nl}	η	m
E	1	0.97	0.93	0.88	0.90	0.83	0.87	0.23	0.21
υ	0.99	1	0.97	0.92	0.94	0.87	0.91	0.10	0.34
σ_y^0	0.97	1.00	1	0.98	1.00	0.96	0.98	0.08	0.36
Q	0.95	0.98	1.00	1	1.00	1.00	1.00	0.08	0.33
ξ	0.96	0.99	1.00	1.00	1	0.98	0.99	0.08	0.35
H_{kin}	0.93	0.97	0.99	1.00	1.00	1	1.00	0.08	0.32
H_{nl}	0.94	0.98	0.99	1.00	1.00	1.00	1	0.08	0.33
η	0.39	0.32	0.26	0.22	0.24	0.19	0.21	1	-0.89
m	-0.03	0.05	0.11	0.14	0.12	0.16	0.14	-0.92	1

Arbitrary shape indenter 1									
	E	υ	σ_y^0	Q	ξ	H_{kin}	H_{nl}	η	m
E	1	0.98	0.86	0.82	0.84	0.80	0.82	0.49	-0.10
υ	0.99	1	0.90	0.86	0.88	0.84	0.86	0.43	-0.02
σ_y^0	0.90	0.92	1	0.99	1.00	0.99	0.99	0.41	0.01
Q	0.84	0.85	0.99	1	1.00	1.00	1.00	0.41	0.00
ξ	0.88	0.89	1.00	1.00	1	1.00	1.00	0.42	0.00
H_{kin}	0.82	0.83	0.98	1.00	0.99	1	1.00	0.40	0.01
H_{nl}	0.84	0.86	0.99	1.00	1.00	1.00	1	0.41	0.00
η	0.53	0.49	0.46	0.43	0.46	0.41	0.44	1	-0.90
m	-0.29	-0.25	-0.20	-0.17	-0.20	-0.16	-0.18	-0.96	1

Arbitrary shape indenter 2									
	E	υ	σ_y^0	Q	ξ	H_{kin}	H_{nl}	η	m
E	1	0.98	0.84	0.79	0.82	0.78	0.79	0.53	-0.18
υ	0.99	1	0.90	0.86	0.89	0.85	0.86	0.47	-0.09
σ_y^0	0.88	0.91	1	1.00	1.00	0.99	1.00	0.45	-0.07
Q	0.82	0.85	0.99	1	1.00	1.00	1.00	0.44	-0.07
ξ	0.86	0.89	1.00	1.00	1	1.00	1.00	0.46	-0.08
H_{kin}	0.79	0.83	0.99	1.00	0.99	1	1.00	0.43	-0.06
H_{nl}	0.82	0.85	0.99	1.00	1.00	1.00	1	0.44	-0.07
η	0.57	0.53	0.49	0.46	0.49	0.44	0.46	1	-0.91
m	-0.33	-0.29	-0.24	-0.21	-0.25	-0.20	-0.22	-0.96	1

Arbitrary shape indenter 3									
	E	υ	σ_y^0	Q	ξ	H_{kin}	H_{nl}	η	m
E	1	1.00	0.91	0.85	0.91	0.83	0.88	0.83	-0.81
υ	0.99	1	0.92	0.86	0.92	0.84	0.88	0.82	-0.81
σ_y^0	0.90	0.92	1	0.99	1.00	0.99	1.00	0.94	-0.93
Q	0.85	0.87	0.99	1	0.99	1.00	1.00	0.95	-0.94
ξ	0.90	0.92	1.00	0.99	1	0.98	1.00	0.94	-0.93
H_{kin}	0.83	0.84	0.99	1.00	0.99	1	1.00	0.94	-0.94
H_{nl}	0.87	0.89	1.00	1.00	1.00	1.00	1	0.95	-0.94
η	0.83	0.83	0.94	0.95	0.95	0.95	0.96	1	-1.00
m	-0.82	-0.82	-0.94	-0.94	-0.94	-0.94	-0.95	-1.00	1

From the results obtained by the spherical indenter, we can clearly see that the two viscous parameters, D and m, are significantly decoupled from the elastic and plastic parameters. Particularly, when the imprint data are added in the objective function (see the data in the upper triangle), the correlations of D and m with the elastic and plastic material parameters decrease below 0.414 and 0.179, respectively. However, for the other parameters, the couplings among the elastic and plastic material parameters do not show a remarkable change in comparison with the ones obtained under the loading-holding-unloading cycle. In the blocks of elastic, plastic and viscous parameters, the material parameters are still strongly coupled among themselves.

Similar phenomena also appear in the results obtained by the other indenters. In the blocks of elastic, plastic and viscous parameters, the material parameters are always strongly coupled among themselves. However, it should be noted that the couplings of m and D are lower than 0.9, when they are identified by the conical indenter and the arbitrary shape indenter 2 when the objective function includes the imprint data.

Here, we can also note that all the parameter correlations, which are obtained by the arbitrary shape indenter 3, are very high. The material parameters are not sensitive to the shape geometries of the indenter tip.

5.2.1. Illustration

Herein, the spherical indenter is used to identify the material properties of the elasto-viscoplastic material which is shown in Table. 5. 5. Different forms of the objective function are used. When the objective function takes into account the imprint data, it is written as Eq. (2.51) and when the objective function does not include the imprint data, it is written as Eq. (2.56). Besides this, two loading histories are used: loading-unloading cycle and loading-holding-unloading-loading-holding-unloading cycle. For the second loading history, the maximum load in the first loading cycle is 60% of the maximum load in the second loading cycle. The curves of load versus time for both loading histories are shown in Fig. 5. 1.

The experimental $P-h$ curve is a set of pseudo experimental data obtained by the spherical indenter using the real input material parameters. The plastic behaviour is described by Eq. (4.1), and the non-linear kinematic hardening is approximated by Armstrong-Frederick law (see Eq. (4.2)). The viscosity is described by Eq. (5.1). The values of the real input material parameters can also be seen in the first line of Table. 5. 9. The initial values of the elasto-viscoplastic material are listed in the second line of Table. 5. 9.

Table. 5. 9. The identified material properties for the elasto-viscoplastic material.

	E	υ	σ_y^0	Q	ξ	H_{kin}	H_{nl}	η	m
	(GPa)		(MPa)	(MPa)		(MPa)		$(MPa/s^{1/m})$	
Real input	200	0.3	400	200	10	100	5	1000	2
Initial	300	0.2	600	300	7	400	3	800	5
Case 1	224.9	0.22	423.0	160.1	7.56	152.5	1.87	445.9	1.24
Error (%)	12.5	26.7	5.8	19.9	24.4	52.5	62.6	55.4	38.0
Case 2	208.1	0.23	426.3	150.8	7.27	154.2	1.77	455.6	1.55
Error (%)	4.1	22.0	6.6	24.6	27.3	54.2	64.6	54.4	22.3
Case 3	207.9	0.19	427.6	152.0	7.35	192.9	2.90	589.8	1.81
Error (%)	3.9	36.7	6.9	24.0	26.5	92.9	42.0	41.0	9.5
Case 4	207.0	0.17	420.4	180.6	6.32	150.2	2.16	465.3	1.52
Error (%)	3.5	43.0	5.1	9.7	36.8	50.2	56.9	53.5	23.9

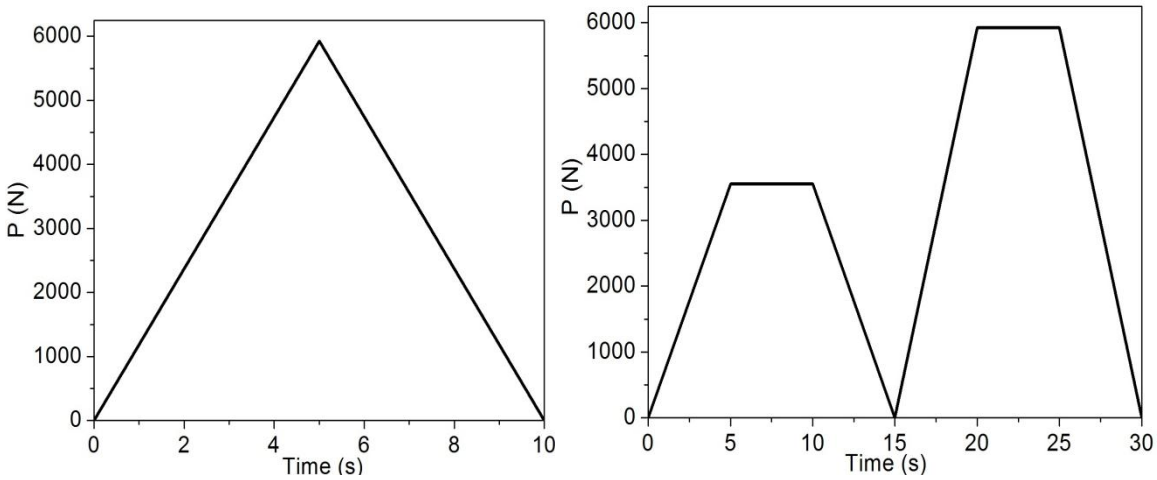

Fig. 5. 1. Two used loading histories: loading-unloading cycle (left), loading-holding-unloading-loading-holding-unloading cycle (right).

The optimized $P-h$ curves and the pseudo experimental data are compared in Fig. 5. 2 and Fig. 5. 5. In Fig. 5. 2, the loading history is single loading-unloading. In Fig. 5. 5, the loading history is more complex. The loading-holding-unloading-loading-holding-unloading cycle is used. In the cases 1 and 3, the objective function does not take into account the imprint data. In the cases 2 and 4, the objective function takes into account the imprint data. The corresponding convergence histories of the objective function can be seen in Fig. 5. 3 and Fig. 5. 6. Moreover, the evolutions of the material parameters are shown respectively in Fig. 5. 4 and Fig. 5. 7. In Fig. 5. 4 and Fig. 5. 7, the normalized material parameter value is defined as the evaluated material parameter value divides the input material parameter value. The final evaluated results obtained by both loading histories are listed in Table. 5. 9.

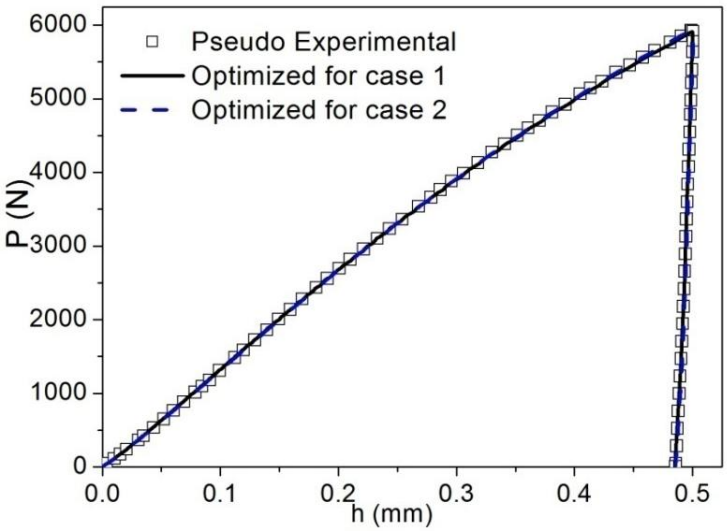

Fig. 5. 2. The optimized $P-h$ curves compared to the pseudo experimental one: loading-unloading cycle is used.

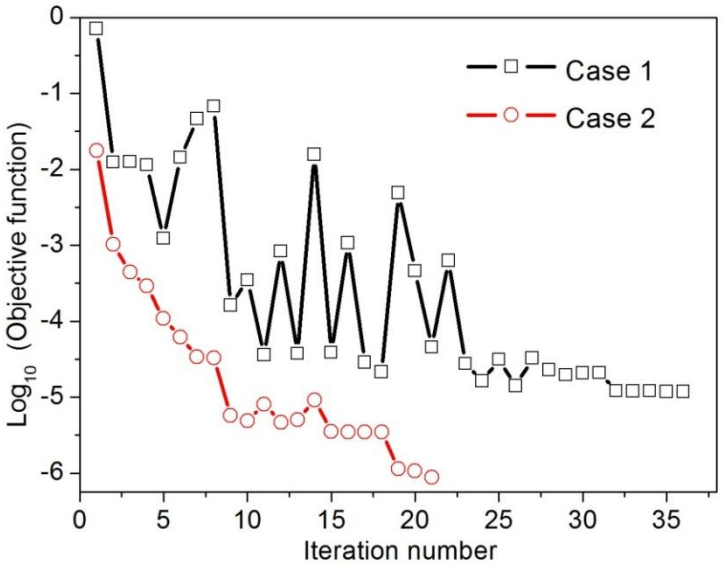

Fig. 5. 3. The convergence histories of the objective function: loading-unloading cycle is used.

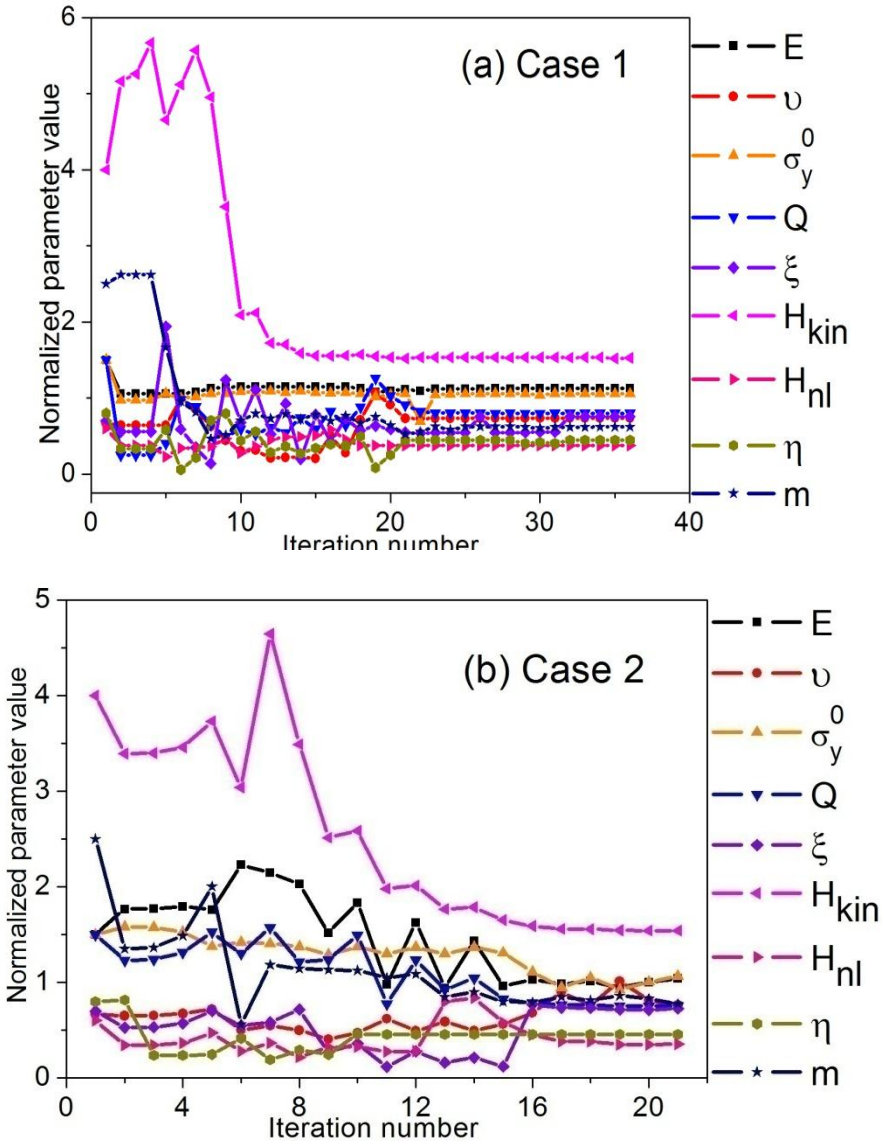

Fig. 5. 4. The evolutions of the material parameters: loading-unloading cycle is used.

It is obvious that the optimal $P-h$ curves usually have a good agreement with the pseudo experimental data. However, we should note that the evaluated material parameters are significantly different from the input material parameters for the case 1. That is because in this case which uses the loading-unloading cycle, all parameters are strongly coupled. The parameter correlations are shown in the lower triangle in Table. 5. 6. However, once the imprint data are taken into account by the objective function, it seems that the accuracy of the Young's modulus is improved. For instance, the error of E is lower than 5% for the case 2.

For the cases 3 and 4 which use the loading-holding-unloading-loading-holding-unloading cycle, the Young's modulus can be correctly evaluated. However, except for the Young's modulus, every identified material parameter has a significant error compared to the input material

parameters. For example, the error of H_{kin} is even larger than 92% compared to the input value in the case 3.

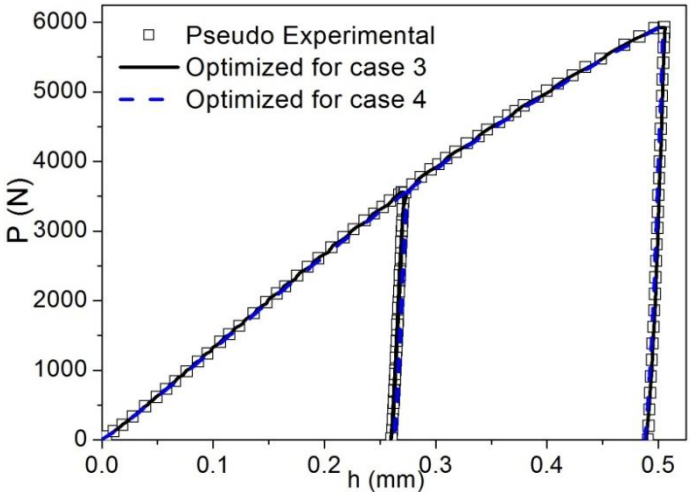

Fig. 5. 5. The optimized $P-h$ curves compared to the pseudo experimental one: loading-holding-unloading-loading-holding-unload cycle is used.

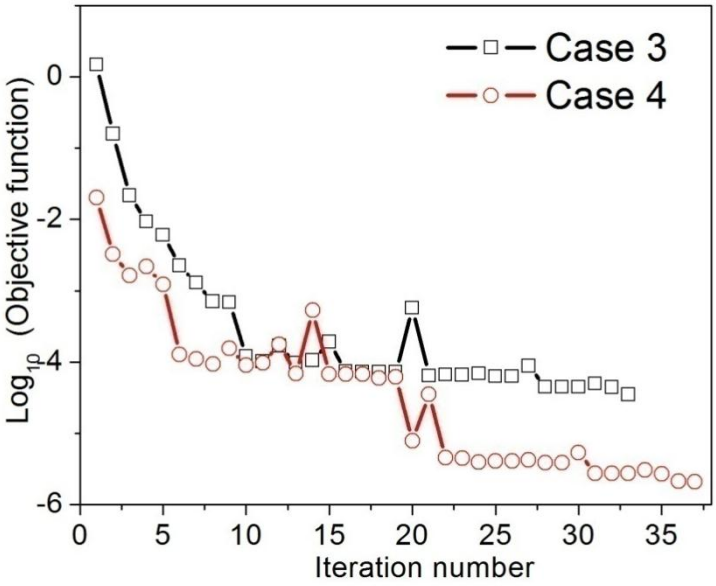

Fig. 5. 6. The convergence histories of the objective function: loading-holding-unloading-loading-holding-unload cycle is used.

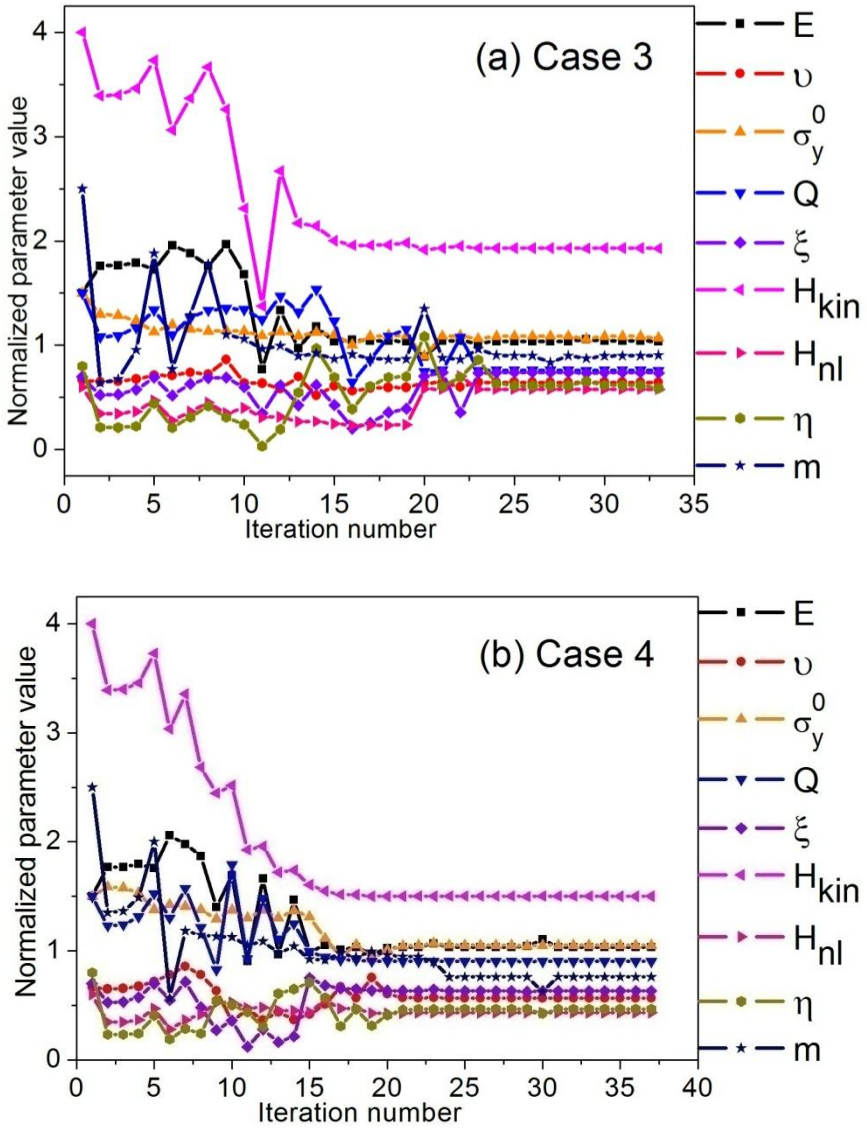

Fig. 5. 7. The evolutions of the material parameters: loading-holding-unloading-loading-holding-unload cycle is used.

According to the parameter correlations which are listed in the lower triangle in Table. 5. 8, it seems that the viscous parameters, η and m are decoupled from the other parameters. However, the evaluated η and m are not correct, this may be due to the fact that η and m are still coupled to each other. Therefore, in order to verify this, three parameters are chosen respectively from elastic, plastic and viscous parameters and the other material parameters are fixed in the following part. For instance, herein E, Q and m are chosen to be variable and the other material parameters are fixed at the input values. Moreover, the different forms of the objective function and the loading history are used to show that the imprint data and the loading history with holding and reloading cycles are helpful in identifying material parameters.

Table. 5. 10. The identified material properties for the elasto-viscoplastic material: E, Q and m are evaluated.

		E (GPa)	Q (MPa)	m	E (GPa)	Q (MPa)	m
		Initial set 1			Initial set 2		
		300	300	5	150	150	1
Identified	Case 1	220.9	180.6	0.24	189.2	186.7	2.51
	Error (%)	10.5	9.7	88.1	5.4	6.7	25.6
	Case 2	207.6	200.2	1.69	203.6	186.4	2.56
	Error (%)	3.8	0.1	15.6	1.8	6.8	28.1
	Case 3	205.0	195.2	2.04	194.4	202.7	1.98
	Error (%)	2.5	2.4	2.1	2.8	1.4	1.0

Two sets of initial values and the corresponding evaluated values of the material parameters are listed in Table. 5. 10. In the cases 1 and 2, single loading-unloading cycles are used. In the case 1, the objective function does not take into account the imprint data. In the case 2, the imprint data are included in the objective function. For the case 3, the loading history is loading-holding-unloading-loading-holding-unloading and the objective function does not take into account the imprint data.

Fig. 5. 8 shows the optimized $P-h$ curves for the cases 1 and 2 which use loading-unloading cycle. It is clear that the optimized $P-h$ curves have a good agreement with the pseudo experimental data. However, Table. 5. 10 shows that E, Q and m are not correctly evaluated in the case 1 for both sets of initial values, all of them have a large error compared to the input values. In the case 2, the accuracy on E is improved by the objective function taking into account the imprint data. The errors of E are lower than 5%. However, the evaluated m are obviously different from the input value for both sets of initial material parameters, the errors of m are larger than 15%. Besides this, it seems that Q is also not correctly evaluated, although its error is very small for the first set of initial material parameters. This is due to the fact that the correlation parameter between Q and m is -0.99 (see it in the lower triangle of Table. 5. 6) and the error of Q is 6.8% for the second set of initial material parameters.

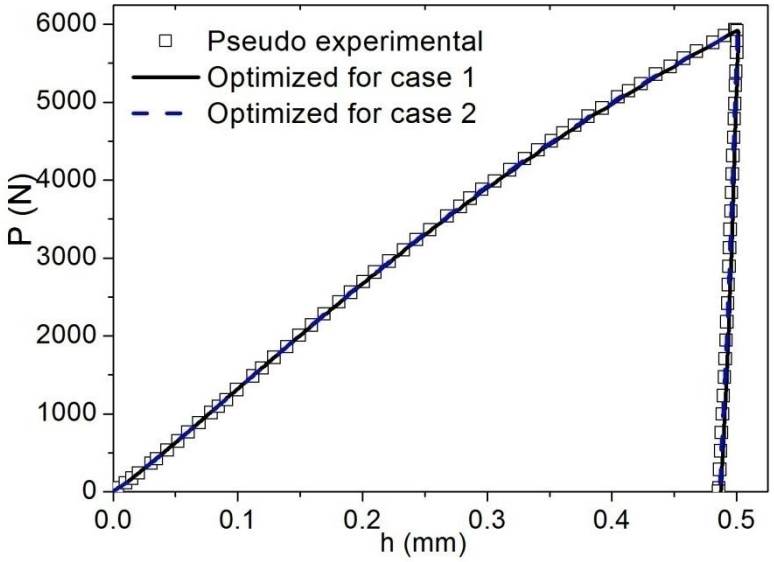

(a) For the initial set 1.

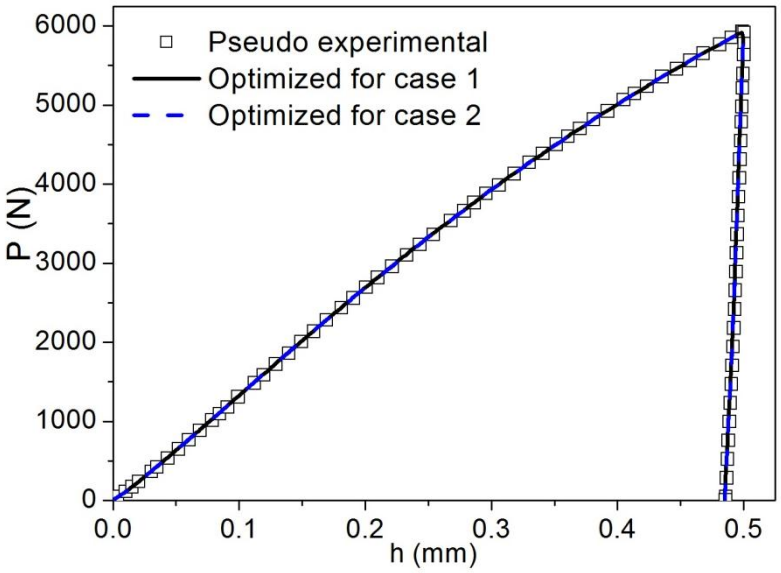

(b) For the initial set 2.

Fig. 5. 8. The optimized $P-h$ curves (only E, Q and m are evaluated) compared to the pseudo experimental one: loading-unloading cycle is used.

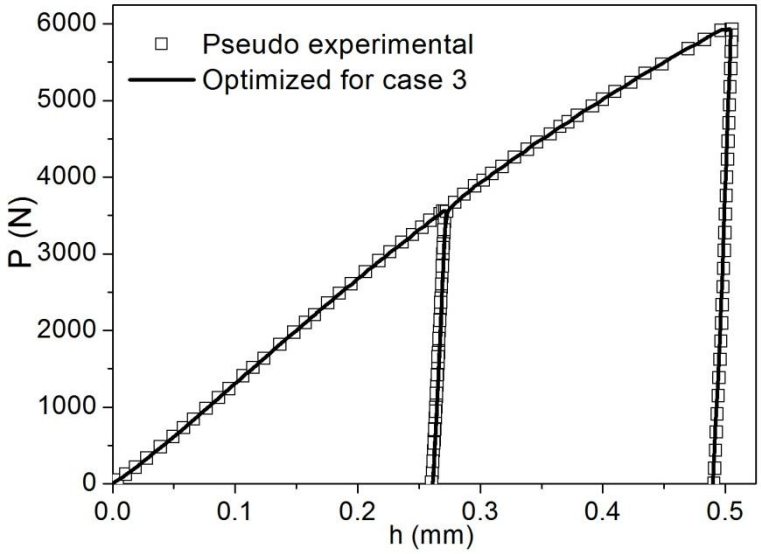

(a) For the initial set 1.

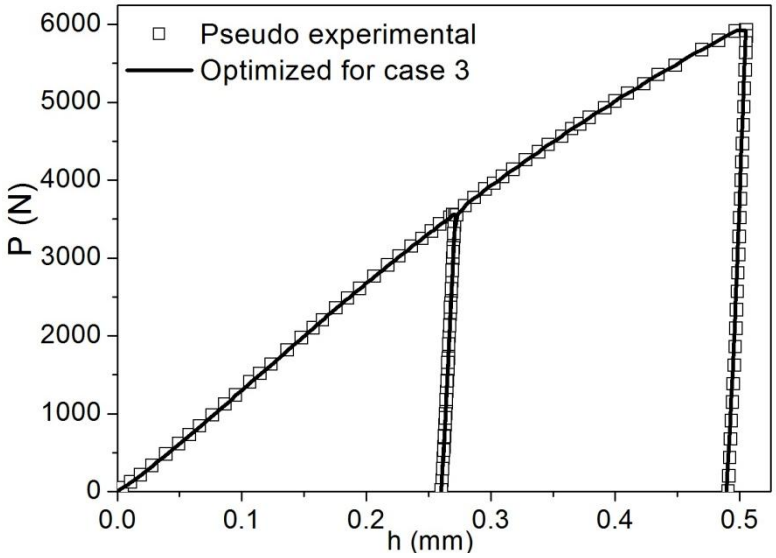

(b) For the initial set 2.

Fig. 5. 9. The optimized $P-h$ curves (only E, Q and m are evaluated) compared to the pseudo experimental one: loading-holding-unloading-loading-holding-unload cycle is used.

Furthermore, we note that for the case 3 which uses loading-holding-unloading-loading-holding-unloading cycle, the accuracies of the evaluated material parameters are significantly improved by the loading history, although the objective function does not take into account the imprint data. The errors of the evaluated material parameters compared to the input values are lower than 5% for both sets of initial material parameters. The optimized $P-h$ curves are shown in Fig. 5. 9. They are almost identical compared to the pseudo experimental one.

Finally, the optimized $P-h$ curves for all the cases are compared in Fig. 5. 10. It is obvious that the optimized $P-h$ curves are nearly identical and Fig. 5. 10 shows they have a good agreement with the pseudo experimental data for both loading histories.

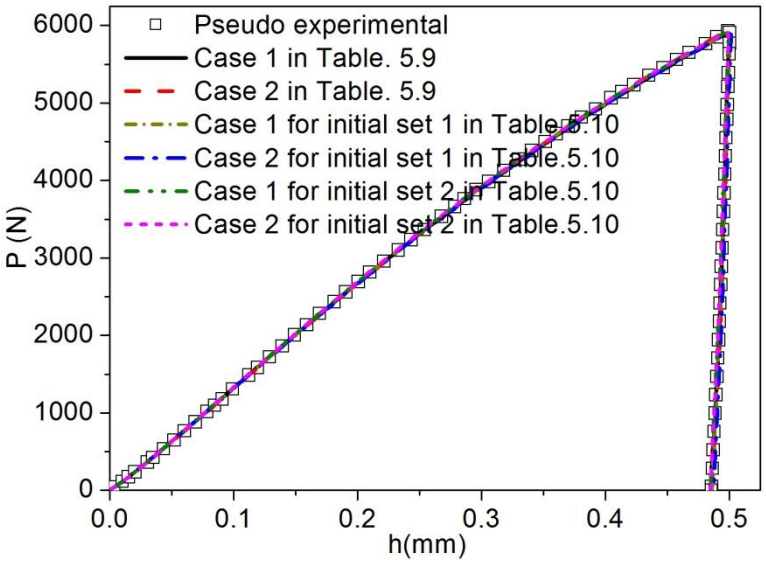

(a) For loading-unloading cycle.

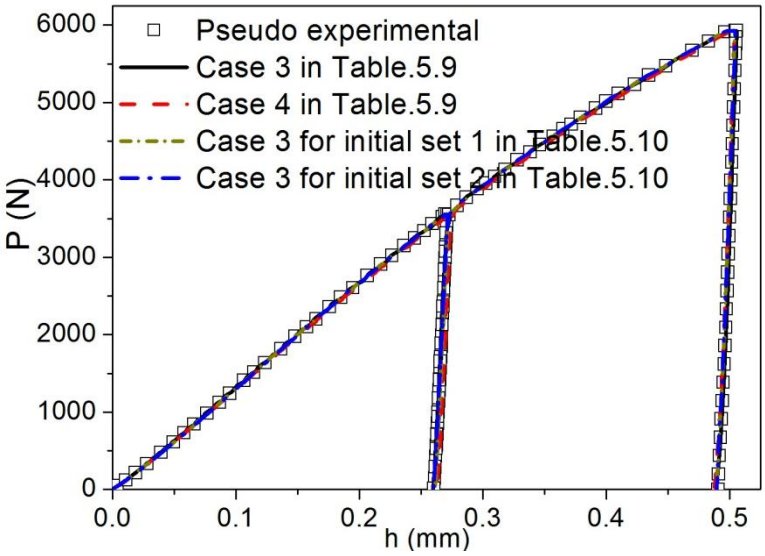

(b) For loading-holding-unloading-loading-holding-unload cycle.

Fig. 5. 10. The comparison of the optimized $P-h$ curves for all the cases.

In the following part, the optimized results for isotropic hardening case are studied. The same initial material parameters which are listed in Table. 5. 9 are used, yet the kinematic hardening parameters, H_{kin} and H_{nl} are fixed at zero. The imprint data are included by the objective function and the loading-unloading cycle is used.

Fig. 5. 11 shows the optimized $P-h$ has a good agreement with the pseudo experimental data. The corresponding convergence history of the objective function and the evaluations of the material parameters are shown respectively in Fig. 5. 12 and Fig. 5. 13. However, Table. 5. 11 shows that the evaluated material parameters have a large error compared to the real input values expect for Q.

In order to investigate the influence of the kinematic hardening on $P-h$ curve, the $P-h$ curve for the isotropic hardening case (H_{kin} and H_{nl} are set to zero, other material parameters are chosen at the same values as the input values) is compared to the pseudo experimental one in Fig. 5. 14. It is obvious that the maximum penetration depth for the isotropic hardening case is larger than the one for the kinematic hardening case for the same maximum load. Thus, it can be said that the influence of the kinematic hardening should not be ignored although the loading history does not include a reloading cycle.

Table. 5. 11. The identified material properties for the elasto-viscoplastic material with isotropic hardening.

	E	υ	σ_y^0	Q	ξ	H_{kin}	H_{nl}	η	m
	(GPa)		(MPa)	(MPa)		(MPa)		$(MPa/s^{1/m})$	
Real input	200	0.3	400	200	10	100	5	1000	2
Initial	300	0.2	600	300	7	0	0	800	5
Identified	227	0.01	420	196	3.0	–	–	417	3.7
Error (%)	13.5	96.7	5.0	2.0	70.0	–	–	58.3	85.2

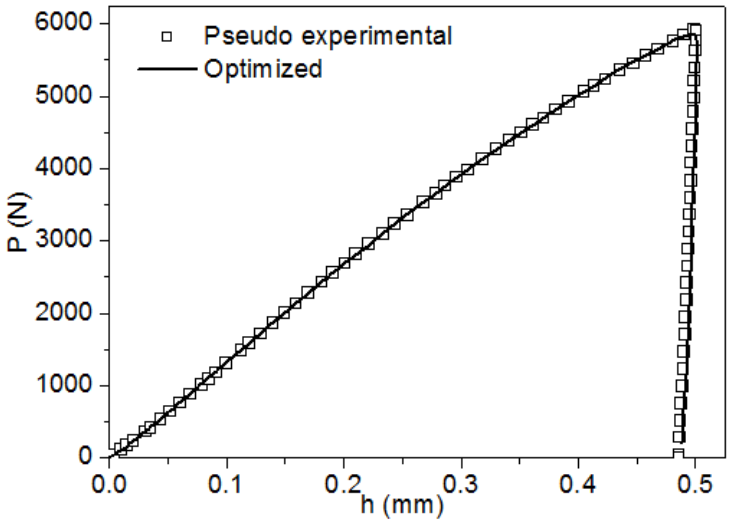

Fig. 5. 11. The optimized $P-h$ curves for the isotropic hardening case.

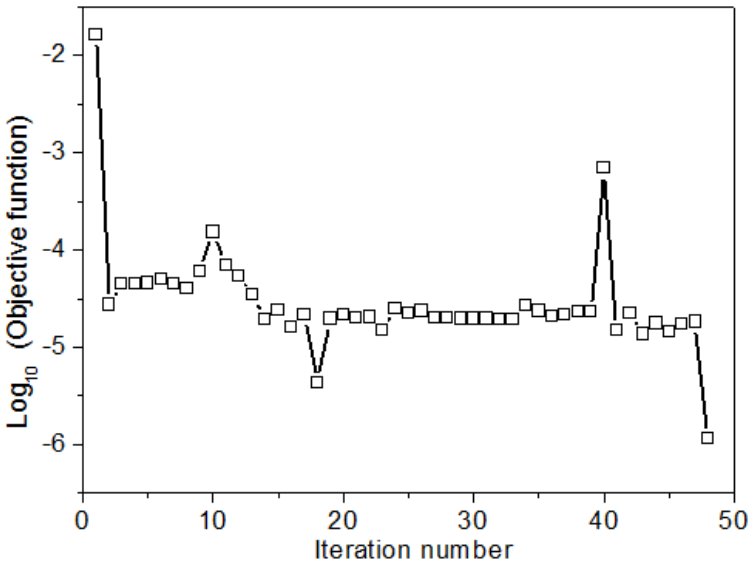

Fig. 5. 12. The convergence history of the objective function.

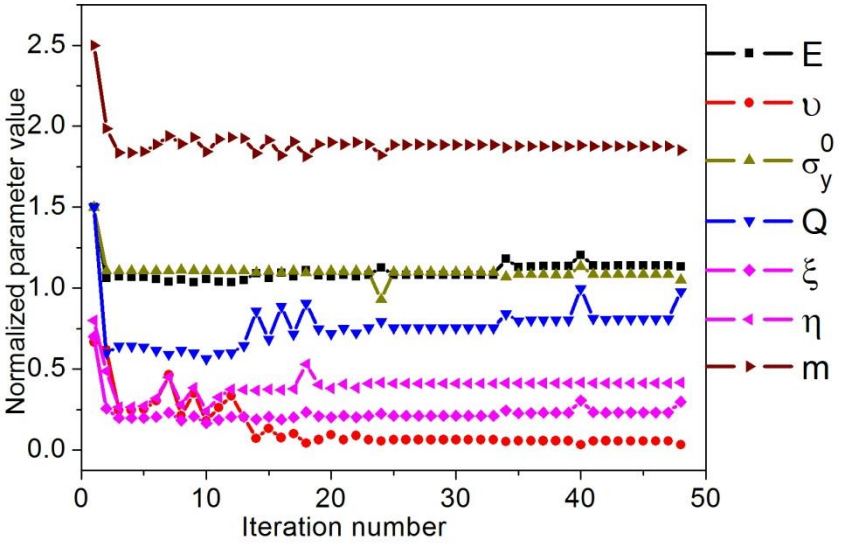

Fig. 5. 13. The evolutions of the material parameters.

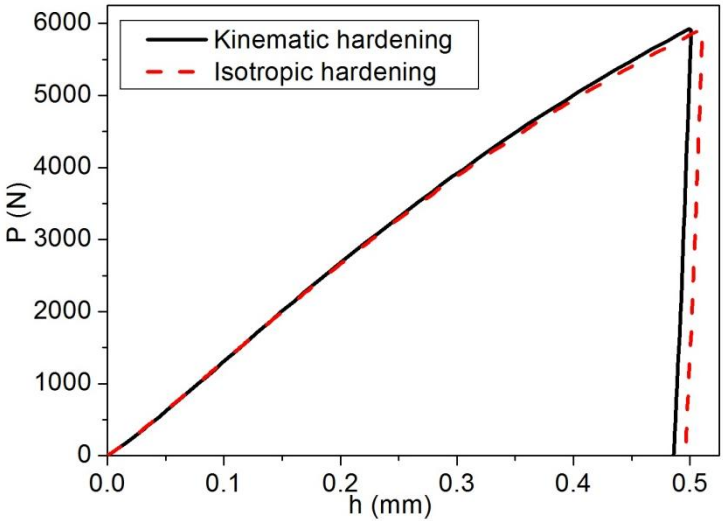

Fig. 5. 14. The $P-h$ curves for the kinematic hardening and isotropic hardening cases.

5.2.2. Conclusions

It is obvious that the residual imprint data are also useful to decrease the parameter correlations for the time-dependent material models. Indeed, the imprint data perform well to decouple the elastic, plastic and viscous parameters from each other, particularly in the case with a holding cycle.

Moreover, the addition of a holding period visibly decreases the correlations of viscous parameters from the other material parameters. From the cases with two holding periods presented in Table. 5. 8, it can be seen that the two viscous parameters of D and m are significantly decoupled from the other material parameters, and that the correlation between D and m also decreases below 0.9, when it is evaluated by the conical indenter and the arbitrary shape indenter 2.

The reloading cycle seems not to reduce the correlations of kinematic hardening parameters with other parameters in a significant way.

From the overall cosine matrices of the Hessian matrices determined by different indenters with different load histories, it can be seen that the blocks of elastic, plastic and viscous material parameters can easily be separated from each other, but they are always fully coupled among themselves.

Besides, it is noted that the conical indenter performs better compared to the other indenters in the identification of the viscous properties of the investigated material.

CHAPTER 6

CONCLUSIONS AND PERSPECTIVES

Overview

The final conclusions of this thesis and some outlooks and perspectives are stated in this chapter.

Contents

6.1. Conclusions

This research project started on September, 2006. Its main aim is to investigate the effect of the indenter tip geometry on the parameter correlation in the identification of material parameters by indentation testing. Through the illustrations presented in this thesis and some researchers' investigations (Constantinescu and Tardieu, 2001; Huber and Tyulyukovskiy, 2004), we have noticed that strongly coupled material parameter correlation is a serious problem in the identification of material parameters. If the material properties are identified using the inverse analysis based on gradient-based optimization algorithms, such correlation of material parameters leads to near-singular matrices in the optimization algorithms, which has a strong effect on convergence rates and on the accuracy with which the location of the minimum of the objective function can be determined. A unique solution is difficult to achieve and the identified material parameters have high errors.

The effects of the tip geometries of some indenters on the correlation of material parameters in parameter identification are investigated in the present thesis. Three arbitrary shape indenters are designed in order to produce different mechanical responses, namely, load versus indentation displacement, and residual imprint. The effects of those indenter tip shapes and the residual imprint data on material parameter correlation are assessed under different loading histories. Several representative material constitutive laws are used, e.g. elasto-plastic, elasto-viscoplastic, in order to evaluate their sensitivity towards indenter tip geometry.

According to the investigations mentioned in this thesis, a deep understanding of the effect of the indenter tip geometry on the parameter correlation in the identification of material parameters is achieved. It is useful to find a strategy to reduce the material parameter correlation. This may help to improve the reliability of material parameter identification procedures which are based on indentation testing combined with inverse methods.

The main original contributions should be emphasised. First, an improved method to calculate the hardness of material for a rounded indenter tip is proposed. Second, the work assesses the effects of imprint data and indenter tip geometry on the correlation of material parameters. Third, it proposes two strategies for improving the identifiability of material parameters. Moreover, the achievements of this work can be summarised as below:

1) The indentation results and the sources of their dispersion are analyzed.

   Normally, in indentation experiments, the dispersion of indentation results is mainly caused by the contact friction, the indentation size effect, the material deformation around the indenter, the imperfect indenter geometry, etc. Besides, when numerical methods are concerned the sources of dispersion come also from the numerical tools because the researchers usually introduce artefact. For instance, in numerical simulations, the errors

caused by the boundary conditions are significant for a small-volume specimen. In addition, pyramid indenters are frequently replaced by conical indenters with equivalent angles. Although the hardness obtained by pyramid indenters are almost similar to the ones obtained by conical indenters, the stress distribution under the indenters and the material deformations around them are completely different compared to the conical indentations.

Moreover, chapter 3 focuses on the influences of the contact friction and of the rounded tip radii of the imperfect conical indenters on the indentation testing results. The results show that neither the contact friction nor the rounded tip radius of the imperfect indenter should be neglected.

2) A method for the evaluation of the correlation of material parameters is presented.

   In the identification of material parameters using the inverse analysis based on the gradient-based optimization method, coupled material parameter correlation generally leads to a non-unique solution. Therefore, it is crucial to find a method to evaluate the correlation of material parameters.

   A cosine matrix of the Hessian matrix is proposed to assess the correlation of the material parameters. It can be determined from the Hessian matrix or the approximated Hessian matrix. They exist in the optimization procedure.

3) A method for reducing the correlation of material parameters is presented.

   Given that the residual imprint data contain the information of the indentation piling-up or sinking-in, they should facilitate the quantification of plastic material behaviour. Therefore, the objective function is designed to take into account the residual imprint mapping data, in order to reduce the correlation of material parameters.

4) Strategies for the improvement of the identifiability of material parameters are proposed and the effects of the residual imprint data on the identification of material parameters are assessed.

   The effect of the imprint data on the correlation of material parameters in the parameter identification is primarily investigated in an elasto-plastic material by a conical indenter. The result shows that the imprint data are helpful to reduce the parameter correlations although the reduction is not significant. Thus, the indenters with special tip shapes are designed in order to produce different piling-up or sinking-in, which is helpful to reduce the parameter correlation and to improve the identifiability of material parameters. Besides, different load histories are applied in the identification of material properties.

   Three indenters with arbitrary shapes are designed. The effects of the tip geometries of the three arbitrary shape indenters on the indentation test data are assessed and compared to the classical indenters. Several materials which exhibit elasto-plastic and elasto-viscoplastic

behaviours are used to evaluate the sensitivity of their parameters towards the indenter tip geometries. In addition, three different load histories are applied on the time-dependent material. The contributions of the holding cycle and the reloading cycle to the determination of the material properties are evaluated.

According to the investigations and the illustrations, it is suggested that the imprint mapping data are important to the identification of the material parameters. Once the imprint data are taken into account in the objective function, the elastic, plastic and viscous parameters can be easily decoupled from each other. Moreover, it is known that the reloading cycle is helpful and the holding cycle is important to determine the properties of the time-dependent material. The viscous material parameters are easily separated from the elastic and the plastic parameters under the effect of the holding cycle.

6.2. Outlooks and Perspectives

Before closing this thesis, it is important to point out that this does not imply the end of the work on this subject. Much more complexities are actually involved in a practical application of indentation testing. On the one hand, thanks to the refinements and the developments of sensor and actuator technology, a more accurate result can be obtained in indentation measurements and the applications of indentation testing are being introduced in more and more engineering fields. On the other hand, indentation is a complex contact system. Some theoretical backgrounds involved in indentation testing are still not completely achieved and mastered. Therefore, some additional technical discussions are presented here.

6.2.1. Assessment of the effect of the indenter tip geometry using 3D model

According to the investigation mentioned in chapter 2, when at the same indentation depth, the areas produced by conical ($\theta = 70.3^{\circ}$), Vickers and Berkovich indenters are identical and the loads are almost the same, they give approximately the same hardness.

However, it is easy to see that, in Fig. 6. 1, Vickers and Berkovich indenters involve more complex tip shape geometries than the conical indenters. The corresponding imprint maps produced by such indenters also have more complex stress distributions. According to the previous investigation (Shi et al., 2010), Berkovich indenter can lead to a larger strain and strain gradient.

The residual imprints produced by Vickers and Berkovich indenters may be more meaningful and valuable to quantify the behaviour of plastic materials. Consequently, in the future, 3D models should be used to assess the effect of the geometries of the indenter tip shapes. However, 3D numerical simulations usually cost more computation time. In the future, this will not be a big problem because, thanks to the rapid development of computers, the task with 3D model can be computed by advanced computers or parallel computing workstation cluster.

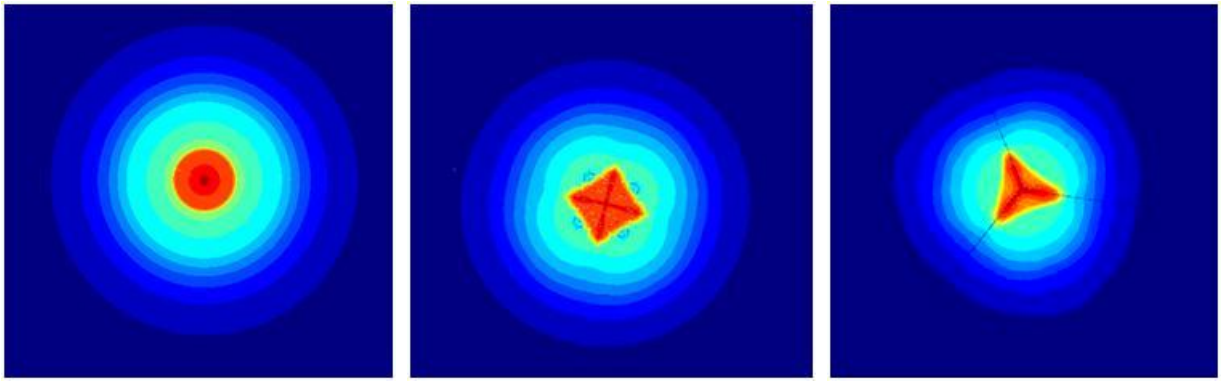

(a) Conical indenter (b) Vickers indenter (c) Berkovich indenter

Fig. 6. 1. The maps of Equivalent plastic strain produced by (a) Conical, (b) Vickers and (c) Berkovich indenters.

6.2.2. Evaluation of more arbitrary shape indenters

Two years ago, some indenters with arbitrary shapes were used in indentation to investigate viscoelastic materials (Kozhevnikov et al., 2008; Kozhevnikov et al., 2010). In the work of (Kozhevnikov et al., 2010), an indenter with seven spherical tips (one is in the centre of a circle and the other six are proportionally located in this circle) is performed. We can note that the pressure distributions under the indenter tips, which are located in the centre and the periphery, are significantly different although the indenter tips have exactly the same geometric shapes.

Those works give us some helpful insights, namely, an indenter should be modelled by several spherical tips with different radii, or with different spaces between them. The relationship between the contact areas and the contact forces are worth investigating. In an indentation test, the load can be written as a function of the indentation depth. For instance, according to the investigation (Oliver and Pharr, 1992), if a spherical indenter is used during the loading, the relationship between P and h is written as $P = Ch^{1.5}$, where, C is a positive constant. Thus, it is known that the slope of the $P-h$ curve increases with an increase of h. If we want to make a change in this slope to investigate the mechanical response of the investigated material, it is

hardly possible for the indenters with symmetry of revolution. However, if the used indenter is modelled by several spherical tips, the relationship between total contact areas and the indentation depth is completely different from the relationship for a single spherical indenter. Therefore, the relationship between P and h will be changed and the slopes of the $P-h$ curve are changed too. Furthermore, the contact areas will become closer to each other with an increase of the indentation depth. The interacting effects of the tips may produce complex stress distributions, it is also worth investigating.

Therefore, the indenter with more complex geometric tip shapes will be evaluated in the future. Such evaluation will be useful because the mechanical response of an indented material under an indenter with complex geometric tip shapes and the imprint data that such indenter produce may contain more valuable information about plasticity. This will help to reduce the correlation of material parameters.

In addition, some researchers (Chollacoop et al., 2003; Cao and Lu, 2004) demonstrated that the conical indenter can be used to determine effectively the plastic properties of typical engineering metallic materials. Besides, many researchers (Chollacoop et al., 2003; Cao and Lu, 2004; Le, 2008; Le, 2009) proposed the use of dual sharp indenters to determine the material properties. They demonstrated that the accuracy of the evaluated material parameters has improved in a significant way. Therefore, an idea is that an indenter with several conical indenters which have a different apex half angle should be used to determine material parameters in the future. Like the aforementioned indenter with spherical tips, the complex geometry shape of such an indenter may be useful to improve the identifiability of material parameters.

REFERENCES

Abu Al-Rub, R.K. and Voyiadjis, G.Z., (2004). Analytical and experimental determination of the material intrinsic length scale of strain gradient plasticity theory from micro- and nano-indentation experiments. International Journal of Plasticity, Vol. 20, pp. 1139-1182.

Abu Al-Rub, R.K., (2007). Prediction of micro and nanoindentation size effect from conical or pyramidal indentation. Mechanics of Materials, Vol. 39, pp. 787-802.

Albrecht, H.J., Hannach, T., Hase, A., Juritza, A., Muller, K. and Muller, W.H., (2005). Nanoindentation: a suitable tool to determine local mechanical properties in microelectronic packages and materials? Archive of Applied Mechanics, Vol. 74, pp. 728-738.

Alcalá, J., Barone, A.C. and Anglada, M., (2000). The influence of plastic hardening on surface deformation modes around Vickers and spherical indents. Acta Materialia, Vol. 48, pp. 3451-3464.

Amini, K. and Rizi, A.G., (2010). A new structured quasi-Newton algorithm using partial information on Hessian. Journal of Computational and Applied Mathematics, Vol. 234, pp. 805-811.

Antunes, J.M., Menezes, L.F. and Fernandes, J.V., (2006). Three-dimensional numerical simulation of Vickers indentation tests. International Journal of Solids and Structures, Vol. 43, pp. 784-806.

Antunes, J.M., Menezes, L.F. and Fernandes, J.V., (2007). Influence of Vickers tip imperfection on depth sensing indentation tests. International Journal of Solids and Structures, Vol. 44, pp. 2732-2747.

Antunez, H.J. and Kleiber, M., (1996). Sensitivity of forming processes to shape parameters. Computer Methods in Applied Mechanics and Engineering, Vol. 137, pp. 189-206.

Balint, D.S., Deshpande, V.S., Needleman, A. and Van der Giessen, E., (2006). Discrete dislocation plasticity analysis of the wedge indentation of films. Journal of the Mechanics and Physics of Solids, Vol. 54, pp. 2281-2303.

Berke, P., Tam, E., plancke-Ogletree, M.P. and Massart, T.J., (2009). Study of the rate-dependent behavior of pure nickel in conical nanoindentation through numerical simulation coupled to experiments. Mechanics of Materials, Vol. 41, pp. 154-164.

Berke, P.Z., (2008). Numerical modeling of the surface and the bulk deformation in a small scale contact. Application to the nanoindentation interpretation and to the micro-manipulation. PhD thesis, Université Libre de Bruxelles, Bruxelles, Belgium.

Bhushan, B. and Sundararajan, S., (1998). Micro/nanoscale friction and wear mechanisms of thin films using atomic force and friction force microscopy. Acta Materialia, Vol. 46, pp. 3793-3804.

Bocciarelli, M., Bolzon, G. and Maier, G., (2005). Parameter identification in anisotropic elastoplasticity by indentation and imprint mapping. Mechanics of Materials, Vol. 37, pp. 855-868.

Bocciarelli, M. and Bolzon, G., (2007). Indentation and imprint mapping for the identification of constitutive parameters of thin layers on substrate: Perfectly bonded interfaces. Materials Science and Engineering: A, Vol. 448, pp. 303-314.

Bocciarelli, M. and Maier, G., (2007). Indentation and imprint mapping method for identification of residual stresses. Computational Materials Science, Vol. 39, pp. 381-392.

References

Bolshakov, A., Oliver, W.C. and Pharr, G.M., (1994). An explanation for the shape of nanoindentation unloading curves based on finite element simulation. Conference: Fall meeting of the Materials Research Society (MRS), Boston, MA (United States).

Bolzon, G., Maier, G. and Panico, M., (2004). Material model calibration by indentation, imprint mapping and inverse analysis. International Journal of Solids and Structures, Vol. 41, pp. 2957-2975.

Borodich, F.M. and Keer, L.M., (2004). Contact problems and depth-sensing nanoindentation for frictionless and frictional boundary conditions. International Journal of Solids and Structures, Vol. 41, pp. 2479-2499.

Bouzakis, K.D., Michailidis, N. and Erkens, G., (2001). Thin hard coatings stress-strain curve determination through a FEM supported evaluation of nanoindentation test results. Surface and Coatings Technology, Vol. 142-144, pp. 102-109.

Bouzakis, K.D., Lontos, A., Michailidis, N., Knotek, O., Lugscheider, E., Bobzin, K. and Etzkorn, A., (2003). Determination of mechanical properties of electron beam-physical vapor deposition-thermal barrier coatings (EB-PVD-TBCs) by means of nanoindentation and impact testing. Surface and Coatings Technology, Vol. 163-164, pp. 75-80.

Brünig, M., (1999). Numerical simulation of the large elastic-plastic deformation behavior of hydrostatic stress-sensitive solids. International Journal of Plasticity, Vol. 15, pp. 1237-1264.

Bucaille, J.L., Felder, E. and Hochstetter, G., (2002). Identification of the viscoplastic behavior of a polycarbonate based on experiments and numerical modeling of the nano-indentation test. Journal of Materials Science, Vol. 37, pp. 3999-4011.

Bucaille, J.L., Stauss, S., Felder, E. and Michler, J., (2003). Determination of plastic properties of metals by instrumented indentation using different sharp indenters. Acta Materialia, Vol. 51, pp. 1663-1678.

Bureau, L., Caroli, C. and Baumberger, T., (2003). Elasticity and onset of frictional dissipation at a non-sliding multi-contact interface. Proceedings of the Royal Society of London Series A-Mathematical Physical and Engineering Sciences, Vol. 459, pp. 2787-2805.

Cao, Y., Li, S.T., Petzold, L. and Serban, R., (2003). Adjoint sensitivity analysis or differential-algebraic equations: The adjoint DAE system and its numerical solution. Siam Journal on Scientific Computing, Vol. 24, pp. 1076-1089.

Cao, Y.P. and Lu, J., (2004). Depth-sensing instrumented indentation with dual sharp indenters: stability analysis and corresponding regularization schemes. Acta Materialia, Vol. 52, pp. 1143-1153.

Carpinteri, A. and Puzzi, S., (2006). A fractal approach to indentation size effect. Engineering Fracture Mechanics, Vol. 73, pp. 2110-2122.

Cense, A.W., Peeters, E.A.G., Gottenbos, B., Baaijens, F.P.T., Nuijs, A.M. and Van Dongen, M.E.H., (2006). Mechanical properties and failure of Streptococcus mutans biofilms, studied using a microindentation device. Journal of Microbiological Methods, Vol. 67, pp. 463-472.

Chandra, A. and Mukherjee, S., (1997). Boundary element methods in manufacturing. Oxford University Press. Inc.

Chen, S.D. and Ke, F.J., (2004). MD simulation of the effect of contact area and tip radius on nanoindentation. Science in China Series G-Physics Astronomy, Vol. 47, pp. 101-112.

Chen, X. and Vlassak, J.J., (2001). Numerical study on the measurement of thin film mechanical properties by means of nanoindentation. Journal of Materials Research, Vol. 16, pp. 2974-2982.

Chen, X., Ogasawara, N., Zhao, M. and Chiba, N., (2007). On the uniqueness of measuring elastoplastic properties from indentation: The indistinguishable mystical materials. Journal of the Mechanics and Physics of Solids, Vol. 55, pp. 1618-1660.

Cheng, L., Xia, X., Scriven, L.E. and Gerberich, W.W., (2005). Spherical-tip indentation of viscoelastic material. Mechanics of Materials, Vol. 37, pp. 213-226.

References

Cheng, Y.T. and Cheng, Z.Z., (1999). Scaling relationships in conical indentation of elastic-perfectly plastic solids. International Journal of Solids and Structures, Vol. 36, pp. 1231-1243.

Cheng, Y.T., Cheng, C.M. and Ni, W., (2006). Methods of obtaining instantaneous modulus of viscoelastic solids using displacement-controlled instrumented indentation with axisymmetric indenters of arbitrary smooth profiles. Materials Science and Engineering: A, Vol. 423, pp. 2-7.

Chollacoop, N., Dao, M. and Suresh, S., (2003). Depth-sensing instrumented indentation with dual sharp indenters. Acta Materialia, Vol. 51, pp. 3713-3729.

Constantinescu, A. and Tardieu, N., (2001). On the identification of elastoviscoplastic constitutive laws from indentation tests. Inverse Problems in Engineering, Vol. 9, pp. 19-44.

Dao, M., Chollacoop, N., Van Vliet, K.J., Venkatesh, T.A. and Suresh, S., (2001). Computational modeling of the forward and reverse problems in instrumented sharp indentation. Acta Materialia, Vol. 49, pp. 3899-3918.

Dettmer, W. and Reese, S., (2004). On the theoretical and numerical modelling of Armstrong-Frederick kinematic hardening in the finite strain regime. Computer Methods in Applied Mechanics and Engineering, Vol. 193, pp. 87-116.

Doerner, M.F. and Nix, W.D., (1986). A method for interpreting the data from depth-sensing indentation instruments. Journal of Materials Research, Vol. 1, pp. 601-609.

Durban, D. and Masri, R., (2008). Conical indentation of strain-hardening solids. European Journal of Mechanics - A/Solids, Vol. 27, pp. 210-221.

Fang, T.H., Chang, W.J. and Weng, C.I., (2006). Nanoindentation and nanomachining characteristics of gold and platinum thin films. Materials Science and Engineering A-Structural Materials Properties Microstructure and Processing, Vol. 430, pp. 332-340.

Fauchais, P., (2004). Understanding plasma spraying. Journal of Physics D: Applied Physics, Vol. 37, pp. 86-108.

Fischer-Cripps, A.C., (2001). Use of combined elastic modulus in the analysis of depth-sensing indentation data. Journal of Materials Research, Vol. 16, pp. 3050-3052.

Fischer-Cripps, A.C., (2002). Nanoindentation. Berlin: Springer-Verlag, New York, NY.

Fischer-Cripps, A.C., (2003). Use of combined elastic modulus in depth-sensing indentation with a conical indenter. Journal of Materials Research, Vol. 18, pp. 1043-1045.

Fischer-Cripps, A.C., Karvánková, P. and Veprek, S., (2006). On the measurement of hardness of super-hard coatings. Surface and Coatings Technology, Vol. 200, pp. 5645-5654.

Foerster, C.E., Stankievicz, J.H., Serbena, F.C., Lepienski, C.M. and Zawislak, F.C., (2007). Flat end and Berkovich instrumented indentation of N and Si irradiated polyethylene - viscoelastic behavior, hardness and elastic modulus. Nuclear Instruments and Methods in Physics Research Section B: Beam Interactions with Materials and Atoms, Vol. 257, pp. 510-514.

Forestier, R., Massoni, E. and Chastel, Y., (2002). Estimation of constitutive parameters using an inverse method coupled to a 3D finite element software. Journal of Materials Processing Technology, Vol. 125, pp. 594-601.

Forestier, R., Chastel, Y. and Massoni, E., (2003). 3D inverse analysis model using semi ¨Canalytic differentiation for mechanical parameter estimation. Inverse Problems in Science and Engineering, Vol. 11, pp. 255-271.

Gao, F. and Takemoto, T., (2006). Mechanical properties evolution of Sn-3.5Ag based lead-free solders by nanoindentation. Materials Letters, Vol. 60, pp. 2315-2318.

Gao, X.L., (2006). An expanding cavity model incorporating strain-hardening and indentation size effects. International Journal of Solids and Structures, Vol. 43, pp. 6615-6629.

Gavrus, A., Massoni, E. and Chenot, J.L., (1996). An inverse analysis using a finite element model for identification of rheological parameters. Journal of Materials Processing Technology, Vol. 60, pp. 447-454.

Gelin, J.C. and Ghouati, O., (1994). An inverse method for determining viscoplastic properties of aluminium alloys. Journal of Materials Processing Technology, Vol. 45, pp. 435-440.

Gerday, A.F., (2009). Mechanical behavior of Ti-5553 alloy. Modeling of representative cells. PhD thesis, Université de Liège, Liège, Belgium.

Giannakopoulos, A.E., (2006). Elastic and viscoelastic indentation of flat surfaces by pyramid indentors. Journal of the Mechanics and Physics of Solids, Vol. 54, pp. 1305-1332.

Gosselin, L., Tye-Gingras, M. and Mathieu-Potvin, F., (2009). Review of utilization of genetic algorithms in heat transfer problems. International Journal of Heat and Mass Transfer, Vol. 52, pp. 2169-2188.

Gouldstone, A., Chollacoop, N., Dao, M., Li, J., Minor, A.M. and Shen, Y.L., (2007). Indentation across size scales and disciplines: Recent developments in experimentation and modeling. Acta Materialia, Vol. 55, pp. 4015-4039.

Haj-Ali, R., Kim, H.K., Koh, S.W., Saxena, A. and Tummala, R., (2008). Nonlinear constitutive models from nanoindentation tests using artificial neural networks. International Journal of Plasticity, Vol. 24, pp. 371-396.

Harsono, E., Swaddiwudhipong, S. and Liu, Z.S., (2009). Material characterization based on simulated spherical-Berkovich indentation tests. Scripta Materialia, Vol. 60, pp. 972-975.

Haseeb, A.S.M.A., (2006). Modeling of the effects of athermal flow strength and activation energy for dislocation glide on the nanoindentation creep of nickel thin film at room temperature. Computational Materials Science, Vol. 37, pp. 278-283.

Hengsberger, S., Kulik, A. and Zysset, P., (2001). A combined atomic force microscopy and nanoindentation technique to investigate the elastic properties of bone structural units. European Cells and Materials, Vol. 1, pp. 12-17.

Hernot, X., Bartier, O., Bekouche, Y., El Abdi, R. and Mauvoisin, G., (2006). Influence of penetration depth and mechanical properties on contact radius determination for spherical indentation. International Journal of Solids and Structures, Vol. 43, pp. 4136-4153.

Huang, G. and Lu, H., (2007). Measurements of two independent viscoelastic functions by nanoindentation. Experimental Mechanics, Vol. 47, pp. 87-98.

Huang, X.Q. and Pelegri, A.A., (2007). Finite element analysis on nanoindentation with friction contact at the film/substrate interface. Composites Science and Technology, Vol. 67, pp. 1311-1319.

Huang, Y., Zhang, F., Hwang, K.C., Nix, W.D., Pharr, G.M. and Feng, G., (2006). A model of size effects in nano-indentation. Journal of the Mechanics and Physics of Solids, Vol. 54, pp. 1668-1686.

Huber, N. and Tsakmakis, C., (1998). Experimental and theoretical investigation of the effect of kinematic hardening on spherical indentation. Mechanics of Materials, Vol. 27, pp. 241-248.

Huber, N. and Tsakmakis, C., (1999a). Determination of constitutive properties from spherical indentation data using neural networks. Part ii: plasticity with nonlinear isotropic and kinematichardening. Journal of the Mechanics and Physics of Solids, Vol. 47, pp. 1589-1607.

Huber, N. and Tsakmakis, C., (1999b). Determination of constitutive properties from spherical indentation data using neural networks. Part i: the case of pure kinematic hardening in plasticity laws. Journal of the Mechanics and Physics of Solids, Vol. 47, pp. 1569-1588.

Huber, N., Konstantinidis, A. and Tsakmakis, C., (2001). Determination of Poisson's ratio by spherical indentation using neural networks - Part I: Theory. Journal of Applied Mechanics-Transactions of the Asme, Vol. 68, pp. 218-223.

Huber, N. and Tsakmakis, C., (2001). Determination of Poisson's ratio by spherical indentation using neural networks - Part II: Identification method. Journal of Applied Mechanics-Transactions of the Asme, Vol. 68, pp. 224-229.

Huber, N. and Tyulyukovskiy, E., (2004). A new loading history for identification of viscoplastic properties by spherical indentation. Journal of Materials Research, Vol. 19, pp. 101-113.

References

Hurtado, J.A. and Kim, K.S., (1999). Scale effects in friction of single-asperity contacts. II. Multiple-dislocation-cooperated slip. Proceedings of the Royal Society of London Series A-Mathematical Physical and Engineering Sciences, Vol. 455, pp. 3385-3400.

Hutchings, I.M., (2009). The contributions of David Tabor to the science of indentation hardness. Journal of Materials Research, Vol. 24, pp. 581-589.

Hysitron, (2005). TriboIndenter User's Manual. Hysitron Inc.

Jeon, E.C., Kim, J.Y., Baik, M.K., Kim, S.H., Park, J.S. and Kwon, D., (2006). Optimum definition of true strain beneath a spherical indenter for deriving indentation flow curves. Materials Science and Engineering: A, Vol. 419, pp. 196-201.

Jeong, S.M. and Lee, H.L., (2005). Finite element analysis of the tip deformation effect on nanoindentation hardness. Thin Solid Films, Vol. 492, pp. 173-179.

Johnson, K.L., (1985). Contact mechanics. Cambridge University press, Cambridge.

Kermouche, G., Loubet, J.L. and Bergheau, J.M., (2004). Extraction of stress-strain curves of elastic-viscoplastic solids using conical/pyramidal indentation testing with application to polymers. Mechanics of Materials, Vol. 40, pp. 271-283.

Kese, K. and Li, Z.C., (2006). Semi-ellipse method for accounting for the pile-up contact area during nanoindentation with the Berkovich indenter. Scripta Materialia, Vol. 55, pp. 699-702.

Kese, K.O., Li, Z.C. and Bergman, B., (2005). Method to account for true contact area in soda-lime glass during nanoindentation with the Berkovich tip. Materials Science and Engineering: A, Vol. 404, pp. 1-8.

Kim, J.H., Yeon, S.C., Jeon, Y.K., Kim, J.G. and Kim, Y.H., (2003). Nano-indentation method for the measurement of the Poisson's ratio of MEMS thin films. Sensors and Actuators A: Physical, Vol. 108, pp. 20-27.

Kim, N.H., Choi, K.K. and Chen, J.S., (2001). Die shape design optimization of sheet metal stamping process using meshfree method. International Journal for Numerical Methods in Engineering, Vol. 51, pp. 1385-1405.

Kim, N.H., Yi, K. and Choi, K.K., (2002). A material derivative approach in design sensitivity analysis of three-dimensional contact problems. International Journal of Solids and Structures, Vol. 39, pp. 2087-2108.

Kim, S.H. and Huh, H., (2002). Design sensitivity analysis of sheet metal forming processes with a direct differentiation method. Journal of Materials Processing Technology, Vol. 130-131, pp. 504-510.

Kizler, P. and Schmauder, S., (2007). Simulation of the nanoindentation of hard metal carbide layer systems - the case of nanostructured ultra-hard carbide layer systems. Computational Materials Science, Vol. 39, pp. 205-213.

Komvopoulos, K. and Yang, J., (2006). Dynamic analysis of single and cyclic indentation of an elastic-plastic multi-layered medium by a rigid fractal surface. Journal of the Mechanics and Physics of Solids, Vol. 54, pp. 927-950.

Kozhevnikov, I.F., Cesbron, J., Duhamel, D., Yin, H.P. and Anfosso-Lédée, F., (2008). A new algorithm for computing the indentation of a rigid body of arbitrary shape on a viscoelastic half-space. International Journal of Mechanical Sciences, Vol. 50, pp. 1194-1202.

Kozhevnikov, I.F., Duhamel, D., Yin, H.P. and Feng, Z.Q., (2010). A new algorithm for solving the multi-indentation problem of rigid bodies of arbitrary shapes on a viscoelastic half-space. International Journal of Mechanical Sciences, Vol. 52, pp. 399-409.

Kruzic, J.J., Kim, D.K., Koester, K.J. and Ritchie, R.O., (2009). Indentation techniques for evaluating the fracture toughness of biomaterials and hard tissues. Journal of the Mechanical Behavior of Biomedical Materials, Vol. 2, pp. 384-395.

Kucharski, S. and Mroz, Z., (2001). Identification of plastic hardening parameters of metals from spherical indentation tests. Materials Science and Engineering A-Structural Materials Properties Microstructure and Processing, Vol. 318, pp. 65-76.

Kucharski, S. and Mroz, Z., (2007). Identification of yield stress and plastic hardening parameters from a spherical indentation test. International Journal of Mechanical Sciences, Vol. 49, pp. 1238-1250.

Landman, U. and Luedtke, W.D., (1996). Atomistic dynamics of interfacial processes: films, junctions and nanostructures. Applied Surface Science, Vol. 92, pp. 237-256.

Le, M.Q., (2008). A computational study on the instrumented sharp indentations with dual indenters. International Journal of Solids and Structures, Vol. 45, pp. 2818-2835.

Le, M.Q., (2009). Material characterization by dual sharp indenters. International Journal of Solids and Structures, Vol. 46, pp. 2988-2998.

Lee, H., Lee, J.H. and Pharr, G.M., (2005). A numerical approach to spherical indentation techniques for material property evaluation. Journal of the Mechanics and Physics of Solids, Vol. 53, pp. 2037-2069.

Leigh, S.H. and Berndt, C.C., (1997). Evaluation of off-angle thermal spray. Surface & Coatings Technology, Vol. 89, pp. 213-224.

Li, J.F., Wang, X.Y., Liao, H., Ding, C.X. and Coddet, C., (2004). Indentation analysis of plasma-sprayed Cr3C2-NiCr coatings. Journal of Materials Science, Vol. 39, pp. 7111-7114.

Liang, L.H., Liu, Y. and Xu, B.H., (2007). Design sensitivity analysis for parameters affecting geometry, elastic-viscoplastic material constant and boundary condition by consistent tangent operator-based boundary element method. International Journal of Solids and Structures, Vol. 44, pp. 2571-2592.

Lim, J.H., (2007). High speed tensile test of automotive steel sheets at the intermediate strain rate. POSCO Technical Report, Vol. 10, pp. 116-122.

Lin, C.K. and Berndt, C.C., (1995). Statistical analysis of microhardness variations in thermal spray coatings. Journal of Materials Science, Vol. 30, pp. 111-117.

Liu, Q.M., Zhang, J. and Yan, L.B., (2009). Response sensitivity and Hessian matrix analysis of planar frames subjected to earthquake excitation. Finite Elements in Analysis and Design, Vol. 45, pp. 695-709.

Liu, Y., Wang, B., Yoshino, M., Roy, S., Lu, H. and Komanduri, R., (2005). Combined numerical simulation and nanoindentation for determining mechanical properties of single crystal copper at mesoscale. Journal of the Mechanics and Physics of Solids, Vol. 53, pp. 2718-2741.

Lugscheider, E., Bobzin, K. and Lackner, K., (2003). Investigations of mechanical and tribological properties of CrAlN+C thin coatings deposited on cutting tools. Surface and Coatings Technology, Vol. 174-175, pp. 681-686.

Luo, J. and Lin, J., (2007). A study on the determination of plastic properties of metals by instrumented indentation using two sharp indenters. International Journal of Solids and Structures, Vol. 44, pp. 5803-5817.

Lysaght, V.E., (1949). Indentation hardness testing. NY : Reinhold, New York.

Ma, X., Yoshida, F. and Shinbata, K., (2003). On the loading curve in microindentation of viscoplastic solder alloy. Materials Science and Engineering A, Vol. 344, pp. 296-299.

Mahnken, R. and Stein, E., (1996a). A unified approach for parameter identification of inelastic material models in the frame of the finite element method. Computer Methods in Applied Mechanics and Engineering, Vol. 136, pp. 225-258.

Mahnken, R. and Stein, E., (1996b). Parameter identification for viscoplastic models based on analytical derivatives of a least-squares functional and stability investigations. International Journal of Plasticity, Vol. 12, pp. 451-479.

Manika, E. and Maniks, J., (2006). Size effects in micro- and nanoscale indentation. Acta Materialia, Vol. 54, pp. 2049-2056.

Mata, M., Anglada, M. and Alcala, J., (2002a). A hardness equation for sharp indentation of elastic-power-law strain-hardening materials. Philosophical Magazine A-Physics of Condensed Matter Structure Defects and Mechanical Properties, Vol. 82, pp. 1831-1839.

References

Mata, M., Anglada, M. and Alcala, J., (2002b). Contact deformation regimes around sharp indentations and the concept of the characteristic strain. Journal of Materials Research, Vol. 17, pp. 964-976.

Mata, M. and Alcala, J., (2004). The role of friction on sharp indentation. Journal of the Mechanics and Physics of Solids, Vol. 52, pp. 145-165.

Mohammadi, Z., Ziaei-Moayyed, A.A. and Mesgar, A.S.M., (2007). Adhesive and cohesive properties by indentation method of plasma-sprayed hydroxyapatite coatings. Applied Surface Science, Vol. 253, pp. 4960-4965.

Nakamura, T. and Gu, Y., (2007). Identification of elastic-plastic anisotropic parameters using instrumented indentation and inverse analysis. Mechanics of Materials, Vol. 39, pp. 340-356.

Nix, W.D. and Gao, H., (1998). Indentation size effects in crystalline materials: A law for strain gradient plasticity. Journal of the Mechanics and Physics of Solids, Vol. 46, pp. 411-425.

Odegard, G.M., Gates, T.S. and Herring, H.M., (2005). Characterization of viscoelastic properties of polymeric materials through nanoindentation. Experimental Mechanics, Vol. 45, pp. 130-136.

Oliver, W.C. and Pharr, G.M., (1992). An improved technique for determining hardness and elastic modulus using load and displacement sensing indentation experiments. Journal of Materials Research, Vol. 7, pp. 1564-1583.

Opitz, A., Ahmed, S.I.U., Schaefer, J.A. and Scherge, M., (2003). Nanofriction of silicon oxide surfaces covered with thin water films. Wear, Vol. 254, pp. 924-929.

Pan, P.Q., (1998). A basis-deficiency-allowing variation of the simplex method for linear programming. Computers & Mathematics with Applications, Vol. 36, pp. 33-53.

Papadimitriou, D.I. and Giannakoglou, K.C., (2008). Computation of the Hessian matrix in aerodynamic inverse design using continuous adjoint formulations. Computers & Fluids, Vol. 37, pp. 1029-1039.

Pelletier, H., (2006). Predictive model to estimate the stress-strain curves of bulk metals using nanoindentation. Tribology International, Vol. 39, pp. 593-606.

Perrott, C.M., (1978). On the indentation fracture of cemented carbide II -- the nature of surface fracture toughness. Wear, Vol. 47, pp. 81-91.

Pharr, G.M., (1998). Measurement of mechanical properties by ultra-low load indentation. Materials Science and Engineering A-Structural Materials Properties Microstructure and Processing, Vol. 253, pp. 151-159.

Pharr, G.M. and Bolshakov, A., (2002). Understanding nanoindentation unloading curves. Journal of Materials Research, Vol. 17, pp. 2660-2671.

Ponthot, J.P., (2002). Unified stress update algorithms for the numerical simulation of large deformation elasto-plastic and elasto-viscoplastic processes. International Journal of Plasticity, Vol. 18, pp. 91-126.

Ponthot, J.P. and Kleinermann, J.P., (2006). A cascade optimization methodology for automatic parameter identification and shape/process optimization in metal forming simulation. Computer Methods in Applied Mechanics and Engineering, Vol. 195, pp. 5472-5508.

Ponthot, J.P., (2010). Finite element code. METAFOR. http://metafor.ltas.ulg.ac.be/dokuwiki/.

Poon, B., Rittel, D. and Ravichandran, G., (2008). An analysis of nanoindentation in elasto-plastic solids. International Journal of Solids and Structures, Vol. 45, pp. 6399-6415.

Qu, S., Huang, Y., Pharr, G.M. and Hwang, K.C., (2006). The indentation size effect in the spherical indentation of iridium: A study via the conventional theory of mechanism-based strain gradient plasticity. International Journal of Plasticity, Vol. 22, pp. 1265-1286.

Rauchs, G., (2006). Optimization-based material parameter identification in indentation testing for finite strain elasto-plasticity. ZAMM - Journal of Applied Mathematics and Mechanics, Vol. 86, pp. 539-562.

Rauchs, G., (2008). The Effect of Load History on Parameter Correlation in Indentation Testing. The 4 th International Conference on Advanced Computational Methods in Engineering, University of Li ège, Belgium.

Rauchs, G., (2009). User Manual of the Finite Element Code HEPPERDANG. Centre de Recherche Public Henri Tudor.

Reid, D.J., (1996). Genetic algorithms in constrained optimization. Mathematical and Computer Modelling, Vol. 23, pp. 87-111.

Rodriguez, J., Rico, A. and Soria, V., (2007). Tribological properties of commercial optical disks estimated from nanoindentation and scratch techniques. Wear, Vol. 263, pp. 1545-1550.

Rodriguez, J., Rico, A., Otero, E. and Rainforth, W.M., (2009). Indentation properties of plasma sprayed Al2O3-13% TiO2 nanocoatings. Acta Materialia, Vol. 57, pp. 3148-3156.

Rogers, D.F., (2001). An introduction to NURBS: with historical perspective. Academic Press, San Diego, USA.

Sakharova, N.A., Fernandes, J.V., Antunes, J.M. and Oliveira, M.C., (2009). Comparison between Berkovich, Vickers and conical indentation tests: A three-dimensional numerical simulation study. International Journal of Solids and Structures, Vol. 46, pp. 1095-1104.

Sauer, R.A. and Li, S.F., (2007). An atomic interaction-based continuum model for adhesive contact mechanics. Finite Elements in Analysis and Design, Vol. 43, pp. 384-396.

Schwarzer, N., (2006). Analysing nanoindentation unloading curves using Pharr's concept of the effective indenter shape. Thin Solid Films, Vol. 494, pp. 168-172.

Schwarzer, N., Chudoba, T. and Pharr, G.M., (2006). On the evaluation of stresses in coated materials during nanoindentation with sharp indenters. Surface & Coatings Technology, Vol. 200, pp. 4220-4226.

Sergeyev, O. and Mroz, Z., (2000). Sensitivity analysis and optimal design of 3D frame structures for stress and frequency constraints. Computers & Structures, Vol. 75, pp. 167-185.

Shi, Z., Feng, X., Huang, Y., Xiao, J. and Hwang, K.C., (2010). The equivalent axisymmetric model for Berkovich indenters in power-law hardening materials. International Journal of Plasticity, Vol. 26, pp. 141-148.

Singh, S.P., Singh, R.P. and Smith, J.F., (2005). Displacement Modulation Based Dynamic Nanoindentation for Viscoelastic Material Characterization. Materials Research Society Symposium Proceedings Vol. 841, pp. 141-146.

Smith, D.E., Tortorelli, D.A. and Tucker, C.L., (1998a). Optimal design for polymer extrusion. Part II: Sensitivity analysis for weakly-coupled nonlinear steady-state systems. Computer Methods in Applied Mechanics and Engineering, Vol. 167, pp. 303-323.

Smith, D.E., Tortorelli, D.A. and Tucker, C.L., (1998b). Analysis and sensitivity analysis for polymer injection and compression molding. Computer Methods in Applied Mechanics and Engineering, Vol. 167, pp. 325-344.

Smith, D.E., Tortorelli, D.A. and Tucker, C.L., (1998c). Optimal design for polymer extrusion. Part I: Sensitivity analysis for nonlinear steady-state systems. Computer Methods in Applied Mechanics and Engineering, Vol. 167, pp. 283-302.

Smith, L.N., German, R.M. and Smith, M.L., (2002). A neural network approach for solution of the inverse problem for selection of powder metallurgy materials. Journal of Materials Processing Technology, Vol. 120, pp. 419-425.

Soare, S., Bull, S.J., O'Neil, A.G., Wright, N., Horsfall, A. and dos Santos, J.M.M., (2004). Nanoindentation assessment of aluminium metallisation; the effect of creep and pile-up. Surface & Coatings Technology, Vol. 177, pp. 497-503.

Solberg, J.M., Jones, R.E. and Papadopoulos, P., (2007). A family of simple two-pass dual formulations for the finite element solution of contact problems. Computer Methods in Applied Mechanics and Engineering, Vol. 196, pp. 782-802.

Song, J., Peters, J., Noor, A. and Michaleris, P., (2003). Sensitivity analysis of the thermomechanical response of welded joints. International Journal of Solids and Structures, Vol. 40, pp. 4167-4180.

Song, J., Shanghvi, J.Y. and Michaleris, P., (2004). Sensitivity analysis and optimization of thermo-elasto-plastic processes with applications to welding side heater design. Computer Methods in Applied Mechanics and Engineering, Vol. 193, pp. 4541-4566.

Stupkiewicz, S., Korelc, J., Dutko, M. and Rodic, T., (2002). Shape sensitivity analysis of large deformation frictional contact problems. Computer Methods in Applied Mechanics and Engineering, Vol. 191, pp. 3555-3581.

Sun, L.W., Fan, Y.B., Li, D.Y., Zhao, F., Xie, T., Yang, X. and Gu, Z.T., (2009). Evaluation of the mechanical properties of rat bone under simulated microgravity using nanoindentation. Acta Biomaterialia, Vol. 5, pp. 3506-3511.

Sun, W., (1998). Newton's method and quasi-Newton--SQP method for general LC1 constrained optimization. Applied Mathematics and Computation, Vol. 92, pp. 69-84.

Suresh, S. and Giannakopoulos, A.E., (1998). A new method for estimating residual stresses by instrumented sharp indentation. Acta Materialia, Vol. 46, pp. 5755-5767.

Suresh, S., Nieh, T.G. and Choi, B.W., (1999). Nano-indentation of copper thin films on silicon substrates. Scripta Materialia, Vol. 41, pp. 951-957.

Swadener, J.G., George, E.P. and Pharr, G.M., (2002a). The correlation of the indentation size effect measured with indenters of various shapes. Journal of the Mechanics and Physics of Solids, Vol. 50, pp. 681-694.

Swadener, J.G., Misra, A., Hoagland, R.G. and Nastasi, A., (2002b). A mechanistic description of combined hardening and size effects. Scripta Materialia, Vol. 47, pp. 343-348.

Tabor, D., (1951). The hardness of metals. Oxford : Clarendon Press.

Taljat, B. and Pharr, G.M., (2004). Development of pile-up during spherical indentation of elastic-plastic solids. International Journal of Solids and Structures, Vol. 41, pp. 3891-3904.

Thurn, J. and Cook, R.F., (2002). Simplified area function for sharp indenter tips in depth-sensing indentation. Journal of Materials Research, Vol. 17, pp. 1143-1146.

Tirupataiah, Y. and Sundararajan, G., (1987). A comprehensive analysis of the static indentation process. Materials Science and Engineering, Vol. 91, pp. 169-180.

Tortorelli, D.A. and Michaleris, P., (1994). Design sensitivity analysis: Overview and review. Inverse Problems in Engineering, Vol. 1, pp. 71-105.

Tsay, J.J. and Arora, J.S., (1990). Nonlinear structural design sensivitity analysis for path dependent problems. Part 1: General theory. Computer Methods in Applied Mechanics and Engineering, Vol. 81, pp. 183-208.

Tuck, J.R., Korsunsky, A.M., Bull, S.J. and Davidson, R.I., (2001). On the application of the work-of-indentation approach to depth-sensing indentation experiments in coated systems. Surface & Coatings Technology, Vol. 137, pp. 217-224.

Tyulyukovskiy, E. and Huber, N., (2007). Neural networks for tip correction of spherical indentation curves from bulk metals and thin metal films. Journal of the Mechanics and Physics of Solids, Vol. 55, pp. 391-418.

Vandamme, M. and Ulm, F.J., (2006). Viscoelastic solutions for conical indentation. International Journal of Solids and Structures, Vol. 43, pp. 3142-3165.

Venkatesh, T.A., Van Vliet, K.J., Giannakopoulos, A.E. and Suresh, S., (2000). Determination of elasto-plastic properties by instrumented sharp indentation: Guidelines for property extraction. Scripta Materialia, Vol. 42, pp. 833-839.

Wang, G., Wan, Z., Wang, X. and Lv, Y., (2008). Genetic algorithm based on simplex method for solving linear-quadratic bilevel programming problem. Computers & Mathematics with Applications, Vol. 56, pp. 2550-2555.

Wang, L. and Rokhlin, S.I., (2005). Universal scaling functions for continuous stiffness nanoindentation with sharp indenters. International Journal of Solids and Structures, Vol. 42, pp. 3807-3832.

Wang, Y., Raabe, D., Kluber, C. and Roters, F., (2004). Orientation dependence of nanoindentation pile-up patterns and of nanoindentation microtextures in copper single crystals. Acta Materialia, Vol. 52, pp. 2229-2238.

References

Warren, A.W. and Guo, Y.B., (2006). Machined surface properties determined by nanoindentation: Experimental and FEA studies on the effects of surface integrity and tip geometry. Surface and Coatings Technology, Vol. 201, pp. 423-433.

Wei, Z., Li, G. and Qi, L., (2006). New quasi-Newton methods for unconstrained optimization problems. Applied Mathematics and Computation, Vol. 175, pp. 1156-1188.

Winnubst, A.J.A., Keizer, K. and Burggraaf, A.J., (1983). Mechanical properties and fracture behaviour of ZrO2-Y2O3 ceramics. Journal of Materials Science, Vol. 18, pp. 1958-1966.

Xue, Z., Huang, Y., Hwang, K.C. and Li, M., (2002). The influence of indenter tip radius on the micro-indentation hardness. Journal of Engineering Materials and Technology-Transactions of the Asme, Vol. 124, pp. 371-379.

Yan, W., Sun, Q., Feng, X.Q. and Qian, L., (2007). Analysis of spherical indentation of superelastic shape memory alloys. International Journal of Solids and Structures, Vol. 44, pp. 1-17.

Yin, Z.J., Tao, S.Y., Zhou, X.M. and Ding, C.X., (2007). Evaluating microhardness of plasma sprayed Al2O3 coatings using Vickers indentation technique. Journal of Physics D-Applied Physics, Vol. 40, pp. 7090-7096.

Youn, S.W. and Kang, C.G., (2005). FEA study on nanodeformation behaviors of amorphous silicon and borosilicate considering tip geometry for pit array fabrication. Materials Science and Engineering A-Structural Materials Properties Microstructure and Processing, Vol. 390, pp. 233-239.

Yu, N., Polycarpou, A.A. and Conry, T.F., (2004). Tip-radius effect in finite element modeling of sub-50 nm shallow nanoindentation. Thin Solid Films, Vol. 450, pp. 295-303.

Zhang, F., Saha, R., Huang, Y., Nix, W.D., Hwang, K.C., Qu, S. and Li, M., (2007a). Indentation of a hard film on a soft substrate: Strain gradient hardening effects. International Journal of Plasticity, Vol. 23, pp. 25-43.

Zhang, J.Q. and Sakai, M., (2004). Geometrical effect of pyramidal indenters on the elastoplastic contact behaviors of ceramics and metals. Materials Science and Engineering A-Structural Materials Properties Microstructure and Processing, Vol. 381, pp. 62-70.

Zhang, M., Djurdjanovic, D. and Ni, J., (2007b). Diagnosibility and sensitivity analysis for multi-station machining processes. International Journal of Machine Tools & Manufacture, Vol. 47, pp. 646-657.

Zhang, T.H. and Yang, Y.M., (2002). Developments and applications of nano-hardness techniques. Advances in Mechanics, Vol. 32, pp. 349-364.

Zhang, Y., Goldgof, D.B., Sarkar, S. and Tsap, L.V., (2007c). A sensitivity analysis method and its application in physics-based nonrigid motion modeling. Image and Vision Computing, Vol. 25, pp. 262-273.

Zhang, Z.L., Kristiansen, H. and Liu, J., (2007d). A method for determining elastic properties of micron-sized polymer particles by using flat punch test. Computational Materials Science, Vol. 39, pp. 305-314.

Zhao, M., Chen, X., Ogasawara, N., Razvan, A.C., Chiba, N., Lee, D. and Gan, Y.X., (2006a). New sharp indentation method of measuring the elastic-plastic properties of compliant and soft materials using the substrate effect. Journal of Materials Research, Vol. 21, pp. 3134-3151.

Zhao, M., Ogasawara, N., Chiba, N. and Chen, X., (2006b). A new approach to measure the elastic-plastic properties of bulk materials using spherical indentation. Acta Materialia, Vol. 54, pp. 23-32.

Zhao, Z.M., Zhang, L., Song, Y.G., Wang, W.G. and Liu, H.B., (2009). Composition, microstructures and properties of Al_2O_3/ZrO_2 (Y_2O_3) self-growing ceramic composites prepared by combustion synthesis under high gravity. Journal of Physics: Conference Series, Vol. 152, pp. 012085.

Zhong, Y. and Zhu, T., (2008). Simulating nanoindentation and predicting dislocation nucleation using interatomic potential finite element method. Computer Methods in Applied Mechanics and Engineering, Vol. 197, pp. 3174-3181.

Zysset, P.K., Guo, X.E., Hoffler, C.E., Moore, K.E. and Goldstein, S.A., (1999). Elastic modulus and hardness of cortical and trabecular bone lamellae measured by nanoindentation in the human femur. Journal of Biomechanics, Vol. 32, pp. 1005-1012.